1-1-1996

The evolution of globular clusters : analysis of external effects and determination of progenitor populations.

Chigurupati Murali
University of Massachusetts Amherst

The Evolution of Globular Clusters: Analysis of External Effects and Determination of Progenitor Populations

A Dissertation Presented

by

Chigurupati Murali

Submitted to the Graduate School of the
University of Massachusetts Amherst in partial fulfillment
of the requirements for the degree of

Doctor of Philosophy

September 1996

Department of Physics and Astronomy

The Evolution of Globular Clusters: Analysis of External Effects and Determination of Progenitor Populations

A Dissertation Presented

by

Chigurupati Murali

Approved as to style and content by:

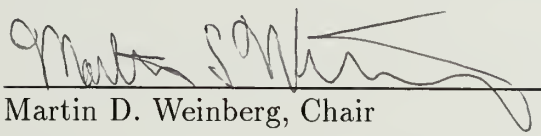

Martin D. Weinberg, Chair

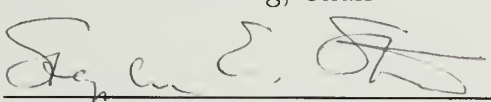

Stephen E. Strom, Member

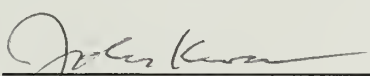

John Kwan, Member

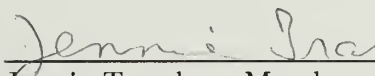

Jennie Traschen, Member

John F. Dubach, Department Head
Department of Physics and Astronomy

ACKNOWLEDGEMENTS

I would foremost like to thank my parents for the limitless support they have provided throughout this and every other stage of my life thus far. I can only hope that these few accomplishments can provide some satisfaction.

I also express utmost gratitude to my advisor, Martin Weinberg, for taking me as a student and for encouraging me when I struggled. He has taught me the satisfaction of being a scientist and the discipline required to experience that ssatisfaction.

Lori Allen, Ted Bergin, Georgina Beristain, Lynne Hillenbrand, David Kastor, David Kendall, Meg Lysaght, Mike Meyer, Jennie Traschen and many others have sustained me with friendship, trips to the Ale House, their inspiration and intensity of discussion and many hilarious moments.

Finally, I must thank Penny for all her patience and support. She may be the only person more glad to see this done than I am.

Abstract

The Evolution of Globular Clusters: Analysis of External Effects and Determination of Progenitor Populations

September 1996

Chigurupati Murali, A.B., Harvard University

Ph.D., University of Massachusetts Amherst

Directed by: Professor Martin D. Weinberg

We include external effects in the Fokker-Planck scheme for studying globular cluster evolution. We use this method to study cluster evolution under the combined influence of relaxation, tidal heating and binary heating of the core in the Milky Way and M87 and related systems in fundamental plane ellipticals. The investigations examine the physical behavior as a function of internal cluster properties and external orbit in a galaxy and use likelihood-based statistical inference to examine possible progenitors of present-day populations.

In M87, cluster evolution is driven by spheroidal heating on low-eccentricity orbits and relaxation on high-eccentricity orbits. The rapid evolutionary rate in the dense inner regions of the galaxy produces the large core in the cluster distribution through depletion. Depletion also leads to an estimated 35% reduction in the specific frequency of globular clusters, S_N. Because smaller fundamental plane ellipticals (FPEs) are denser at a given fiducial radius than larger FPEs, homologous cluster populations evolve more rapidly in the smaller FPEs. This partially explains differences in S_N observed in FPEs.

In the Milky Way, cluster evolution is dominated by disk heating on low-eccentricity orbits and relaxation on high-eccentricity orbits, regardless of inclination. Disk influence leads to strong evolution with approximately 55% reduction in the initial population. Evaporation on high-eccentricity orbits dominates leading to

greater tangential bias in both disk and halo populations as a function of time. The inferred initial halo population appears to match the kinematics of the observed halo field star population. Conversely, the inferred initial disk population does not appear to match the kinematics of any disk populations. These results suggest that the flattened component of the cluster population formed in the dissipative collapse that preceded the formation of the Galactic disk.

Table of Contents

List of Tables

List of Figures

Chapter 1

Introduction

Early estimates of main-sequence stellar lifetimes when applied to globular cluster color-magnitude diagrams yielded cluster age estimates of many Gyr (Sandage 1953). Though present-day age estimates are larger, the conclusion that clusters are among the oldest objects in the Universe is indisuptable. This realization naturally engendered the notion that clusters also represent 'fossil' relics of the proto-galaxy (e.g. Larson 1990) and has led to inferences regarding the formation and early evolution of the Milky Way based on the observed properties of globular clusters and their apparent relationship to halo field stars (e.g. Eggen, Lynden-Bell & Sandage 1962; Searle and Zinn 1978).

More recently, detailed observations have revealed globular cluster systems surrounding numerous external galaxies with a range of morphological types (Harris 1991). While direct age estimates for the individual clusters in these systems are not generally available, their luminosities and colors imply ages similar to those of Milky Way clusters. It has become evident, therefore, that cluster formation is a generic feature of the formation and evolution of galaxies themselves.

Theoretical studies of globular cluster dynamics have progressed at the same time as these other investigations. The principal catalyst has been the recognition that two-body relaxation drives evolution on a timescale that is much less than the age of a typical cluster. The earliest investigations by Ambartsumian (1938), Spitzer (1940) and Chandrasekhar (1942) have led to the thorough picture of internally driven evolution which is available today (c.f. Chapter 2)[1].

[1]Note that while the more precise age estimates described above were not available at the time of these early investigations, a typical age was considered to be on the order of 3 Gyr; e.g. Chandrasekhar (1943).

An important goal of the theory of cluster evolution is to infer the initial conditions of cluster systems and thereby elucidate their significance as proto-galactic fossils. In particular, researchers have sought to ascertain the size of the initial population, the initial distribution of cluster masses and their kinematic properties at the time of formation. The results of such investigations so far indicate that clusters have evolved considerably since formation. As a result, the significance of observed clusters as fossils is not obvious.

However, most theoretical research has focused on internally-driven evolution although it is evident that clusters also undergo a variety of tidal effects due to their orbits in the host galaxy. Conversely, studies focusing on external effects have generally not included this refined understanding of internal effects. It has therefore been difficult to directly infer the degree to which observed cluster properties have changed through evolution.

The work presented here is an attempt to establish more clearly the primordial properties of globular cluster systems and shed light on the notion of clusters as 'fossil relics'. These efforts encompass a methodological domain which is needed to attack the problem formally and numerically, and an astronomical domain in which the fundamental questions arise.

The initial goal was to develop theoretical and numerical methods to describe external tidal effects on clusters. By developing these methods in connection with the Fokker-Planck description of internal evolution, we established a valuable tool for studying cluster evolution in relation to observations of real clusters- particularly for investigating the statistical properties of evolving cluster populations. Chapter 2 presents a comprehensive discussion of this implementation, the physical significance of external effects and preliminary implications for Milky Way globulars.

Given these tools for studying cluster evolution in galactic environments, we then began to investigate the initial conditions of cluster systems in the Milky Way and external galaxies. One of the best known cluster systems outside of the Milky Way surrounds M87, the giant elliptical which dominates the center of the Virgo cluster of galaxies. Chapter 3 describes our study of this system and applications to the evolution of globular cluster populations in elliptical galaxies in general.

Finally, in Chapter 4, we return to the original goal of defining the initial conditions of the Milky Way globular cluster system. This work is still in progress but the preliminary results show important changes have occurred in the cluster system.

Each chapter represents a paper which has been or is in the process of being submitted to *Monthly Notices of the Royal Astronomical Society.* The text is unchanged and the original abstract has been given as the lead text prior to the introduction in each chapter. The appendices have been included at the end of the thesis as per the University submission requirements but have been separated according to the chapter in which they originally appeared.

Chapter 2

The Effect of the Galactic Spheroid on Globular Cluster Evolution

We study the combined effects of relaxation, tidal heating and binary heating on globular cluster evolution, exploring the physical consequences of external effects and examining evolutionary trends in the Milky Way population. Our analysis demonstrates that heating on circular and low-eccentricity orbits can dominate cluster evolution. The results also predict rapid evolution on eccentric orbits either due to strong relaxation caused by the high densities needed for tidal limitation or due to efficient bulge shocking of low density clusters.

The combination of effects leads to strong evolution of the population as a whole. For example, within the solar circle, tidally-limited $10^5 M_\odot$ clusters lose at least 40% of their mass in 10 Gyr. At high eccentricity most of these clusters evaporate completely. Bulge shocking disrupts clusters within 40 kpc which have less than 80% of their mass within their pericentric inner Lagrange point. Our results are consistent with suggestions that the shape of the cluster luminosity function results from evaporation and disruption of low mass clusters; they further predict that the net velocity dispersion of the cluster system in the inner Galaxy has decreased with time. Preliminary constraints on formation models are also discussed. We conclude that the observed cluster system has largely been shaped by dynamical selection.

2.1 Introduction

Many studies of globular cluster evolution have focused on internal mechanisms which drive evolution. This work has produced a clear picture in which initial stellar evolution causes significant mass loss from a nascent cluster

(e.g. Chernoff & Weinberg 1990); two-body relaxation leads to mass segregation (e.g. Inagaki & Saslaw 1985) and core collapse in surviving clusters (e.g. Cohn 1980); binary heating halts collapse (e.g. Lee et al. 1991); and the cluster continuously loses mass due to the escape of stars, eventually undergoing complete evaporation (e.g. Lee & Goodman 1995).

It is also recognized that the Galaxy influences cluster evolution. The time-dependent tidal field heats clusters and tidal limitation aids in the removal of escaping stars. Previous investigations have considered disk shocking, bulge shocking and tidal limitation, concluding that each will play a role, particularly in the inner Galaxy (e.g. Spitzer & Chevalier 1973; Chernoff & Shapiro 1987; Aguilar, Hut & Ostriker 1988; Weinberg 1994). In addition, recent observational studies showing correlations of cluster properties with Galactocentric position indicate the measurable influence of the Galaxy (e.g Chernoff & Djorgovski 1989; Djorgovski et al 1993; Djorgovski & Meylan 1994).

The principal tool used in studies of cluster evolution over the last decade-and-a-half has been direct solution of the Fokker-Planck equation (Cohn 1979). However, most of these calculations have excluded external effects. Recently, using time-dependent perturbation theory to investigate disk shocking, Weinberg (1994) demonstrated that resonant forcing can perturb internal stellar trajectories beyond the limit expected from adiabatic invariance. This indicates that the Galaxy plays a greater role in cluster evolution than previously thought and motivates new studies of cluster evolution which combine internal and external effects.

The importance of external heating requires us to re-examine the current picture of internally-driven evolution. In particular, external effects will influence the collapse rates, evaporation times and general physical properties derived in previous calculations. The present work compares this behavior with and without

heating over a wide range of cluster properties to present a revised view. This study also examines the survival and disruption characteristics of clusters on a range of Galactic orbits to shed light on the initial conditions of the cluster system. The results demonstrate that evolution does indeed depend strongly on position and orbit, further implying that observed cluster properties have been largely determined through dynamics.

Our study rests on a linear theory of external heating– based on Weinberg's (1994) treatment of disk shocking– which we include in numerical solutions of the Fokker-Planck equation. Nearly all previous work has emphasized impulsive shock heating due to a single passage through the disk or bulge. The work presented here describes resonant heating due to the time-varying tidal field encountered on periodic orbits of the cluster in the Galaxy- an effect we refer to as *orbit* heating. In this context, shock heating is seen to result from the broad resonances caused by an impulsively applied external force.

Although our treatment of external heating can include the influence of any component of the Galactic potential, here we consider only the spheroid in order to allow precise definition of the physical behavior and preliminary description of the evolutionary trends. The present study includes heating on cluster orbits in the isothermal sphere and is used to study cluster evolution from initial King model states to the point of complete evaporation on a range of orbits in the Galaxy. Our conclusions, therefore, place only lower limits on the overall rate of cluster evolution but are significant nonetheless.

The plan of the paper is as follows. We derive the linear theory of external heating in §2.2 and discuss its physical interpretation in §2.3. In §2.4, the numerical implementation is described. In §2.5 we present the results of our study of cluster evolution under the combined influence of internal and external effects. Finally, in §2.6, we discuss the implications of the results for the Milky Way

globulars. Readers concerned primarily with the effects of heating and its evolutionary consequences may skip §2.2 without loss of continuity.

2.2 Derivation of external heating rate

The physics behind the perturbation theory discussed below can be summarized as follows. Each orbit in the cluster acts like a pendulum with two-degrees of freedom (cf. Binney & Tremaine 1987, Chap. 3). The time-dependent tidal field can drive the pendula at a discrete or continuous spectrum of frequencies depending on whether the perturbation is quasi-periodic or aperiodic, respectively. Because the temporal variation discussed here is caused by the cluster's orbit in the spherical component of the Galaxy, the spectrum is discrete. For disk shocking described by Weinberg (1994), the spectrum is continuous. In both cases, the energy of each orbit changes as it passes through the resonance. The accumulated effect of all possible resonances on all orbits, drives the secular evolution of the equilbrium distribution function (DF). The expressions given below are valid for both periodic and aperiodic cases.

We compute the evolution by expanding the Boltzmann equation to first order and solving for the perturbed distribution function (neglecting self-gravity). The first-order change phase mixes but second order energy input leads to an induced phase space flux which helps drive cluster evolution. N-body comparisons shown in Appendix A.5 indicate that the self-gravity of the tidally-induced wake has negligible effect for cases of interest here.

We use a locally inertial reference frame which is centered on the cluster and has axes fixed in space (see Appendix A.1 for derivation). The unperturbed Hamiltonian is therefore completely separable, implying the existence of action-angle variables. This frame allows the internal dynamics to be defined in accordance with the standard Fokker-Planck technique (e.g. Cohn 1979) which

uses an energy-space DF $f(E)$ and depends on the adiabatic invariance of the radial action. Within this framework, we derive a version of the formalism presented by Weinberg (1994) which describes heating of globular clusters on arbitrary orbits in external potentials.

2.2.1 Perturbed distribution function

The linearized Boltzmann equation is a linear partial differential equation in seven variables. Using action-angle variables, we can separate the equation and employ standard DFs constructed according to Jeans' theorem (Binney & Tremaine 1987). The explicit form of the linearized Boltzmann equation is

$$\frac{\partial f_1}{\partial t} + \frac{\partial f_1}{\partial \mathbf{w}}\frac{\partial H_0}{\partial \mathbf{I}} - \frac{\partial f_0}{\partial \mathbf{I}}\frac{\partial H_1}{\partial \mathbf{w}} = 0, \tag{2.1}$$

where $\mathbf{w}$ is the vector of angles, and $\mathbf{I}$ are the conjugate actions. The quantities f_0 and H_0 depend on the actions alone. The small variation in Galactic potential over a typical cluster size allows quadratic expansion of the tidal field (see Appendix A.1 for details). We may thus define $H_1 = u(\mathbf{r})g(t)$ and expand in a Fourier series in action-angle variables (e.g. Tremaine & Weinberg 1984). Each term $f_{1\mathbf{l}}$ in the Fourier series is the solution of the following differential equation:

$$\frac{\partial f_{1\mathbf{l}}}{\partial t} + (i\mathbf{l}\cdot\mathbf{\Omega})\mathrm{f}_{1\mathbf{l}} = \mathrm{i}\mathbf{l}\cdot\frac{\partial \mathrm{f}_0}{\partial \mathbf{I}}\mathrm{U}_{\mathbf{l}}(\mathbf{I})\mathrm{g}(\mathrm{t}) \equiv \mathrm{i}\mathbf{l}\cdot\frac{\partial \mathrm{f}_0}{\partial \mathbf{I}}\mathrm{H}_{1\mathbf{l}}, \tag{2.2}$$

where $\mathbf{\Omega} = \partial \mathrm{H}/\partial \mathbf{I}$ and

$$U_{\mathbf{l}}(\mathbf{I}) = \frac{1}{(2\pi)^3}\int_{-\pi}^{\pi} \mathrm{u}(\mathbf{r})\mathrm{e}^{-\mathrm{i}\mathbf{l}\cdot\mathbf{w}}\mathrm{d}^3\mathbf{w}. \tag{2.3}$$

The inhomogeneous equation may be solved using a Green's function (e.g. Birkhoff & Rota 1962, p.39) to give the time-dependence for each coefficient of the perturbed DF

$$f_{1\mathbf{l}} = i\mathbf{l}\cdot\frac{\partial f_0}{\partial \mathbf{I}} U_{\mathbf{l}}(\mathbf{I}) e^{-i\mathbf{l}\cdot\Omega t}\int_{t_0}^{t} dt' e^{i\mathbf{l}\cdot\Omega t'} g(t'), \tag{2.4}$$

where we have assumed that the perturbation begins at time t_0.

2.2.2 Heating rate

The rate of change in energy arising from the perturbation follows from Hamilton's equations (Weinberg 1994). The total phase-averaged change in energy can be written as

$$\langle E\rangle = \int_{t_0}^{t} dt \sum_{\mathbf{l}=-\infty}^{\infty} (i\mathbf{l}\cdot\Omega) H_{1-\mathbf{l}} f_{1\mathbf{l}}. \tag{2.5}$$

Substituting for $f_{1\mathbf{l}}$ from equation (2.4) yields

$$\langle E\rangle = -4\pi^3 \sum_{\mathbf{l}=-\infty}^{\infty} (\mathbf{l}\cdot\Omega)(\mathbf{l}\cdot\frac{\partial f_0}{\partial \mathbf{I}})|U_{\mathbf{l}}|^2 \left| \int_{t_0}^{t} dt' e^{i\mathbf{l}\cdot\Omega t'} g(t') \right|^2, \tag{2.6}$$

which represents the heat input due to the perturbation during an interval $\Delta t = t - t_0$. This expression is valid for finite-duration, aperiodic perturbations such as disk passage as well as periodic perturbations which arise on regular orbits in the Galaxy. In particular, Weinberg's (1994) results for disk shocking are obtained from equation (2.6) by substituting the tidal amplitude appropriate to the disk profile for $g(t')$ and integrating over the interval $(-\infty, \infty)$ assuming a linear trajectory.

For periodic perturbations it is more suitable to derive the asymptotic heating rate (e.g. Landau & Lifschitz 1965, p.151). We first expand the tidal amplitude in a Fourier series

$$g(t) = \sum_{n=-\infty}^{\infty} a_n e^{in\omega t}, \tag{2.7}$$

and substitute into equation (2.6). Taking the limit $t \to \infty$ and assuming the onset of the perturbation at $t_0 = 0$, we obtain

$$\langle \dot{E} \rangle = -8\pi^4 \sum_{l=-\infty}^{\infty} (\mathbf{l} \cdot \mathbf{\Omega})(\mathbf{l} \cdot \frac{\partial f_0}{\partial \mathbf{I}})|U_l|^2 \sum_{n=-\infty}^{\infty} |a_n|^2 \delta(n\omega - \mathbf{l} \cdot \mathbf{\Omega}). \quad (2.8)$$

Integrating $\langle \dot{E} \rangle$ over inclination and angular momentum, we obtain the change in energy which defines the induced change in the distribution, given by a one-dimensional continuity equation in energy space (appropriate to the 1D Fokker-Planck formulation employed below; see Appendix A.3 for derivation):

$$\frac{\partial f}{\partial t} = \frac{1}{16\pi^2 P(E)} \frac{\partial}{\partial E} \{\langle \langle \dot{E} \rangle \rangle\}, \quad (2.9)$$

where $P(E)$ is the phase space volume. This is called the equation of quasilinear diffusion in the plasma literature (e.g. Stix 1992). The term *quasilinear* refers to the proportionality of the heating rate to the squared amplitudes of the linear modes. The linear modes arise from the resonant forcing of stellar orbits by a periodic perturbation. The competition between two-body relaxation and this externally induced phase space flux can strongly influence globular cluster evolution, as we will show below.

2.2.3 Heating rate in isothermal sphere

Below we will need the heating rate for a cluster orbiting in the isothermal sphere. For most galaxies, the small variation in potential over a typical cluster size allows quadratic expansion of the tidal field. Therefore, the perturbing Hamiltonian is:

$$H_1 = \frac{1}{2}\Omega_0^2(t)[-\cos 2\Theta(t)x^2 - 2\sin 2\Theta(t)xy - \cos 2\Theta(t)y^2 + z^2], \quad (2.10)$$

where $\Omega_0(t) = V_0/R(t)$ is the angular rotation speed at the orbital radius at time t and $\Theta(t) = \int_0^t dt'\Omega$ is the instantaneous azimuthal angle of orbit. Using equations (10) and (11) in Weinberg (1994), we can write the perturbation as a series in action-angle variables:

$$H_1 = \frac{1}{2}\Omega_0^2(t) \sum_{l=-\infty}^{\infty} \{\frac{1}{3}\sqrt{4\pi} V_{000}(\beta)\delta_{l_20}\delta_{l_30}$$
$$+\frac{2}{3}\sqrt{\frac{4\pi}{5}} V_{2l_20}(\beta)\delta_{l_30} - e^{-2i\Theta}\sqrt{\frac{2\pi}{15}} V_{2l_22}(\beta)\delta_{l_32}$$
$$-e^{2i\Theta}\sqrt{\frac{2\pi}{15}} V_{2l_2,-2}(\beta)\delta_{l_3,-2}\} X_{l_2}^{l_1} e^{i\mathbf{l}\cdot\mathbf{w}}, \tag{2.11}$$

where

$$X_{l_2}^{l_1} = \frac{1}{2\pi}\int_{-\pi}^{\pi} dw_1 e^{-il_1 w_1} r^2 e^{il_2(\psi - w_2)}, \tag{2.12}$$

β is the inclination of the orbital plane and $V_{ll_2l_3}(\beta)$ is a rotation matrix (e.g. Tremaine & Weinberg 1984). The angle $\psi - w_2$ is the difference between the mean azimuthal angle w_2 and the azimuthal angle in the orbital plane. We substitute this expansion into equation (2.8) and average over inclination and angular momentum to derive the heating rate

$$\langle\langle \dot{E} \rangle\rangle = -8\pi^4 \sum_{l=-\infty}^{\infty} \int d\kappa\kappa J_{max}^2/\Omega_1 (\mathbf{l}\cdot\mathbf{\Omega})(\mathbf{l}\cdot\frac{\partial \mathrm{f}_0}{\partial \mathbf{I}})|\mathrm{X}_{l_2}^{l_1}|^2$$
$$\Big\{\Big[(\frac{1}{18}+\frac{1}{90})\delta_{l_20} + \frac{1}{60}\delta_{l_2|2|}\Big] \sum_{n=-\infty}^{\infty} |a_n|^2 \delta(\mathbf{l}\cdot\mathbf{\Omega} - \mathrm{n}\omega)$$
$$+\Big[\frac{1}{30}\delta_{l_20} + \frac{1}{20}\delta_{l_2|2|}\Big] \sum_{n=-\infty}^{\infty} |b_n|^2 \delta(\mathbf{l}\cdot\mathbf{\Omega} - \mathrm{n}\omega)\Big\}, \tag{2.13}$$

where

$$a_n = \frac{1}{P}\int_{-P/2}^{P/2} dt \Omega_0^2(t) e^{-in\omega t}, \tag{2.14}$$

$$b_n = \frac{1}{P}\int_{-P/2}^{P/2} dt \Omega_0^2(t) e^{-2i\Theta(t) - in\omega t} \tag{2.15}$$

and P is the period of the cluster orbit.

For an isotropic DF, $\mathbf{l} \cdot \partial \mathrm{f_0}/\partial \mathbf{I} = (\mathbf{l} \cdot \mathbf{\Omega})\mathrm{df_0/dE}$. We also explore the effect of anisotropy using Merritt-Osipkov models (e.g. Binney & Tremaine 1987). The distribution function takes the form $f_0(\mathbf{I}) = \mathrm{f(Q)}$, where $Q = E \pm J^2/2r_a^2$, $\mathbf{l} \cdot \partial \mathrm{f_0}/\partial \mathbf{I} = df_0/dQ(\mathbf{l} \cdot \mathbf{\Omega} \mp \mathrm{l_1 \Omega_1 J/\Omega_2 r_a^2} \pm \mathrm{l_2 J/r_a^2})$. The anisotropy increases with decreasing anisotropy radius, r_a.

2.3 Discussion of physical mechanism

A cluster orbiting in the Galaxy feels a time-dependent tidal field. A typical orbit is periodic and introduces a periodic external force on orbits of cluster stars. As described in §2.2, resonant heating occurs when the periods of stellar orbit and external force coincide, leading to repeated acceleration and increase in the energy of individual orbits. Integrated over many periods, the energy gained by the orbit increases linearly with time (c.f. eq. 2.8). Energy absorption eventually leads to the evolution of individual orbits. (see Appendix A.4 for discussion and numerical implementation of finite duration resonances). This in turn drives the secular evolution of the cluster potential.

Orbits can either gain or lose energy to the tidal field depending on the particular resonance. For example, in disk galaxies with flat rotation curves it is well-known that the inner Lindblad resonance loses energy to a perturbation while an outer Lindblad resonance gains energy. However, for isotropic distribution functions with $df/dE > 0$, the perturbation always heats the system on average though some localized regions of phase space may lose energy.

Non-resonant interaction has no net effect on an orbit. Successive maxima in the external force tend to accelerate and decelerate the star equally, leading to asymptotic cancellation as long as the initial transients remain linear (i.e. do not alter the intrinsic frequency of the star with an initial jolt). Over short times,

non-resonant heating does occur because the time duration is insufficient for complete cancellation to occur.

Non-linear transient or *impulsive* heating leads to rapid change in orbital energies as a rapidly applied force 'kicks' a star regardless of its orbital frequency. However, the standard impulse approximation, when used to describe a periodic perturbation, ignores the long-term decay of transient energy in the linear limit as well as the linear growth in energy at the resonances. For most cases of interest, heating rates are in the linear limit, implying that external influence depends primarily on secular transfer of energy through orbital resonances.

To illustrate the behavior of transients and transient decay, Figure 2.1 compares the exact time-dependent energy input given by equation (2.6) with the energy input defined by the asymptotic heating rate equation (2.8). Transients decay rapidly at low energy and more slowly at high energy. Empirically, we find that two to three Galactic orbital periods are required before the asymptotic limit is effectively reached. This treatment therefore adequately describes all but the outermost halo clusters for which initial transients may still be important. The comparisons of perturbation theory with N-body simulation shown in Appendix A.5 demonstrate the validity of the approach.

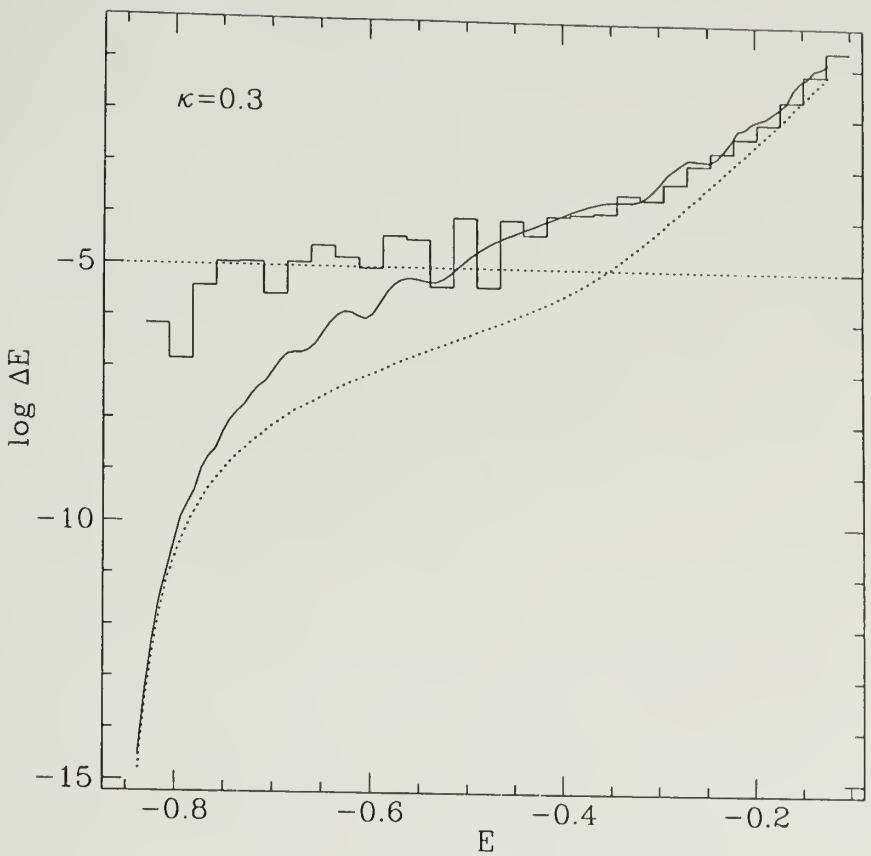

Figure 2.1. Mean change in energy of stellar distribution: theory vs. simulation. The mean change in energy as a function of internal orbital energy in a $W_0 = 5$ King model due to heating on an eccentric $\kappa = 0.3$ ($e \approx 0.7$) orbit after one orbital period. Comparison of simulation (histogram), exact time-dependent perturbation theory (equation 6, solid) and heat input calculated from asymptotic heating rate (equation 8, dotted) shows that initial transients decay strongly at low energy while impulsive energy change persists at high energy. Horizontal dotted line indicates the level of accuracy in the simulation.

The magnitude of the heating rate is determined by the cluster profile, density and orbit. The profile and density define the distribution of internal orbital frequencies and the cluster orbit defines the external forcing frequencies and amplitude. For a cluster of fixed profile and mass, the density is determined by the tidal radius. Individual clusters may not be tidally limited due to initial conditions or heating-driven expansion. Therefore we use the function $M(x_p)$ to parameterize the fraction of the total cluster mass enclosed within the instantaneous pericentric inner Lagrange point, x_p. This function depends on the profile and the ratio of cluster mean density to the mean density required by tidal limitation. A tidally-limited cluster has limiting radius, $R_c = x_p$, and therefore $M(x_p) = 1$, while a tidally-unlimited has $R_c > x_p$ and therefore $M(x_p) < 1$. Heating rates for a given orbit increase as $M(x_p)$ decreases.

The perturbing potential in the logarithmic sphere, equation (2.10), heats clusters on orbits of any eccentricity. The tide transfers energy and angular momentum to the cluster through the resonances, which unbinds stars. On circular orbits, the tidal field creates a triaxial perturbation of constant amplitude proportional to Ω_0^2 rotating with fixed pattern speed Ω_0. On eccentric orbits, conservation of center-of-mass angular momentum introduces time-dependent amplitude and rotation rate. This produces more resonances. Tidal torquing can also induce a net spin.

The rate of external heating is also influenced by our choice of equilibrium phase space distributions. For example, according to Jeans' theorem, one can define equilibria in the rotating frame of a circular cluster orbit using the Jacobi constant, E_J (e.g. Heggie & Ramamani 1994). By transforming to the frame in which the perturbation is time-independent, we remove the resonances from the problem. We can therefore choose a bound distribution of orbits in E_J using the limiting zero-velocity surface, so no stars are lost and the cluster experiences no

Table 2.1. Processes and parameter dependences

	Parameters							
Process	α	m_l	m_u	W_0	$M(x_p)$	M_c	E	κ
Relaxation	√	√	√	√	√	√		
External Heating				√	√	√	√	√
Core Heating	√	√	√	√	√	√		

net tidal heating, although inertial energies and angular momenta are not conserved. Using $f(E)$ instead of $f(E_J)$ leads to heating in the analogous case because we cannot choose orbits which are strictly bound. In any case, a real cluster cannot reach true equilibrium because it is bound and therefore undergoes relaxation. In fact, as is shown below, it is typically a competition between external heating and relaxation due to strong resonances with diffused core stars that strongly influences cluster evolution.

2.4 Fokker-Planck Calculations

To determine the influence of external heating on cluster evolution, we conduct a series of Fokker-Planck calculations which begin with King model initial conditions and run through core collapse to complete evaporation. Relaxation is computed using the multi-mass code of Chernoff & Weinberg (1990) which solves Henon's (1961) orbit-averaged Fokker-Planck equation. Core heating is included in the form described by Lee et al (1991) with a time step that supresses stochastic core osillations. Implementation of external heating is detailed in Appendix A.4. The comparisons shown in Appendix A.5 are used to test the implementation.

Each physical process depends on the input model parameters listed in Table 2.1. The total mass is denoted by M_c and the concentration by W_0. Orbits in the

isothermal sphere are defined by their energy E and angular momentum J. In place of absolute angular momentum J, we use the relative angular momentum $\kappa = J/J_{max}(E)$, where $J_{max}(E)$ is the angular momentum of a circular orbit with energy E. The value $\kappa = 0$ denotes a radial orbit and the value $\kappa = 1$ denotes a circular orbit. The apocentric, pericentric and mean orbital radii are denoted R_a, R_p, R_{av}, respectively. We represent the Galactic potential as a singular isothermal sphere with rotation velocity $v_0 = 220$ km/s.

We consider a range of initial values for $M(x_p)$. If the young, rich LMC clusters are representative of young globular clusters, $M(x_p)$ may be significantly smaller than unity initially (Elson, Fall & Freeman 1987). Furthermore, as discussed in §2.5.4.2, formation scenarios can imply varying degrees of tidal truncation for an individual cluster depending on the local conditions under which it forms and the orbit on which it travels.

The distribution of stellar masses in the cluster is given by a power-law mass spectrum, $dN/dM \propto m^{-\alpha}$, with upper and lower mass limits m_l and m_u, respectively. Fiducial values $\alpha = 2.35$, $m_l = 0.1$ and $m_u = 2.0$ are adopted in §2.5.1 to represent the cluster mass spectrum following the period of strong stellar evolution when relaxation, tidal heating and binary heating dominate cluster evolution. The importance of stellar evolution diminishes after ~ 1 Gyr for $\alpha = 2.35$ and $m_l = 0.1$ which corresponds to the main sequence lifetime for a $2M_\odot$ A-star. The effect of changing the mass spectrum is explored in §2.5.2.

2.5 Results

2.5.1 Orbital heating and bulge shocking

Because heating rates depend on cluster profile, tidal truncation and orbit, comparisons in different physical regimes are needed to demonstrate the primary

influences of heating on cluster evolution. We choose four specific examples listed in Table 2.2.

Example 1 compares the relative strengths of heating rates on different orbits using physically identical clusters, each of which is tidally-limited at its orbital pericenter. In this case, because the average tidal strength is largest on circular orbits, heating is also strongest on circular orbits and decreases with eccentricity (Figure 2.2).

To investigate the effect of heating on long-term evolution, we compare evaporation times, t_{ev}, for tidally limited clusters of different mass, concentration and κ. Table 2.3 shows t_{ev} normalized by the circular, $10^5 M_\odot$ $W_0 = 5$ case (arbitrary scaling to physical units is provided in §2.5.4.1). In these comparisons, clusters of a particular mass and concentration are identical and clusters of differing mass and concentration possess the mean density required for tidal limitation.

For identical clusters, t_{ev} decreases monotonically with κ, reaching a minimum for circular orbits. Evaporation times can decrease by a factor of two in circular cases when tidal heating is included. The relative evaporation times reflect the relative strength of heating rates shown in Figure 2.2. Heating accelerates evolution because external forcing efficiently torques and expels high-energy core stars on radial orbits, as noted by Oh & Lin (1992) in N-body calculations. This reduces the local relaxation time in the core, enhances relaxation rates and causes rapid evaporation. Spitzer & Chevalier (1973) noted this effect in certain regimes of disk shocking, interpreting it as an increase in the core-halo temperature gradient (see also Chernoff & Shapiro 1987, Weinberg 1994). For the highest eccentricities, t_{ev} is only slightly shorter than with no heating, demonstrating the insignificance of high-eccentricity heating in tidally-limited clusters.

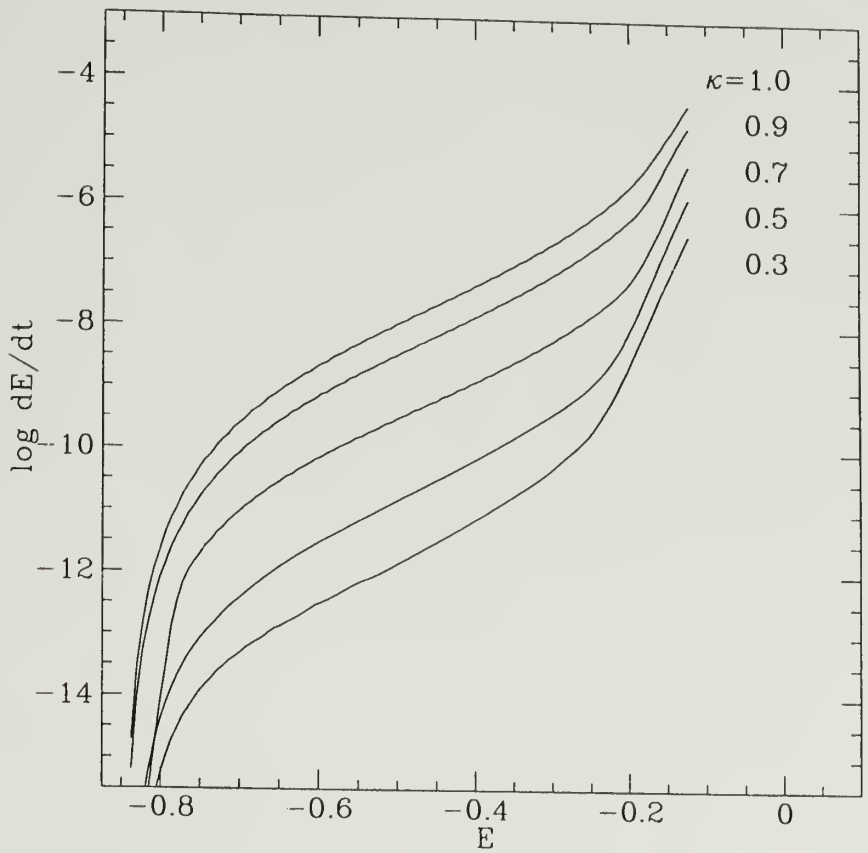

Figure 2.2. Heating rates for Example 1. Heating rates are compared in identical tidally-limited $W_0 = 5$ clusters on different orbits. Values of κ are indicated to the right of each curve. Heating on circular orbits dominates because the average tidal strength is highest, decreasing with eccentricity because average tidal amplitude drops monotonically. Heating rates in circular and $\kappa = 0.3$ case differ by about 2 orders of magnitude. In the circular case, orbits near the tidal boundary gain $\sim 10\%$ in energy in an orbital time.

Table 2.2. Example scenarios for a $10^5 M_\odot$ cluster

Example	κ	R_a^a	R_p^a	P^b	r_t^c	x_p^c	$M(x_p)$	t_{dyn}^d
1	1.0	8.5	8.5	2.5	70	70	1.0	5.0
	0.9	11.2	9.2	2.1	70	70	1.0	5.0
	0.7	19.6	10.3	3.1	70	70	1.0	5.0
	0.5	37.8	11.8	5.3	70	70	1.0	5.0
	0.3	89.4	13.7	11.3	70	70	1.0	5.0
2	1.0	8.5	8.5	2.5	70	70	1.0	5.0
	0.9	9.4	7.6	1.8	63.5	63.5	1.0	4.3
	0.7	10.9	5.7	1.7	48.5	48.5	1.0	2.9
	0.5	11.9	3.7	1.7	33.2	33.2	1.0	1.6
	0.3	12.4	1.9	1.6	19.3	19.3	1.0	0.7
3	1.0	8.5	8.5	2.5	70	70	1.0	5.0
	0.9	9.4	7.6	1.8	70	61.4	1.0	5.0
	0.7	10.9	5.7	1.7	70	47.6	0.99	5.0
	0.5	11.9	3.7	1.7	70	31.5	0.92	5.0
	0.3	12.4	1.9	1.6	70	16.4	0.63	5.0
4	0.3	15.0	2.3	1.9	22.9	22.9	1.0	0.9
	0.3	15.0	2.3	1.9	41.3	23.5	0.95	2.3
	0.3	15.0	2.3	1.9	48.8	21.1	0.9	2.9
	0.3	15.0	2.3	1.9	61.1	20.3	0.8	4.1
	0.3	15.0	2.3	1.9	73.2	19.4	0.7	5.4

[a] (kpc), [b] (100 Myr), [c] (pc), [d] (Myr)

In many cases, evaporation time does not vary strongly with concentration for the same orbit and mass, indicating that overall mass loss rates are insensitive to initial concentration. In the exceptional $\kappa = 0.9$ and 1.0, $W_0 = 3$, $10^6 M_\odot$ cases, heating causes rapid disruption because these clusters have low binding energy and long relaxation times and are easily torn apart by the tide.

While Example 1 compares heating rates as a function of eccentricity in identical clusters, the orbits occupy different regions of the Galaxy (c.f. Table 2.2). In Example 2, we consider clusters in similar regions by comparing tidally-limited clusters on orbits of equal mean radius. Because they are tidally truncated, these clusters still undergo the same rate of heating relative to internal energies shown in

Table 2.3. Evaporation times t_{ev}

$W_0 = 3$	κ				
M_c ($M_\odot$)	1.0	0.9	0.6	0.3	nh[a]
1.0×10^5	0.65	0.95	1.27	1.29	1.30
1.0×10^6	0.94	3.69	9.61	10.9	11.2
$W_0 = 5$	κ				
M_c ($M_\odot$)	1.0	0.9	0.6	0.3	nh
1.0×10^5	1.00	1.15	1.34	1.37	1.38
5.0×10^5	3.20	4.25	5.64	6.10	6.20
1.0×10^6	5.20	7.01	10.31	11.43	11.82
$W_0 = 7$	κ				
M_c ($M_\odot$)	1.0	0.9	0.6	0.3	nh
1.0×10^5	1.12	1.27	1.40	1.41	1.42
5.0×10^5	3.97	4.70	5.95	6.25	6.37
1.0×10^6	6.35	8.29	11.06	11.96	12.13

[a] nh denotes no heating

Figure 2.2. However, cluster densities vary due to differences in orbital angular frequencies. For fixed cluster mass, this implies that tidal radii will vary.

The tidal radius r_t decreases with the increased perigalactic angular frequency at higher eccentricity. This increases the mean density and decreases the dynamical time t_{dyn}, producing shorter relaxation times, larger evaporation rates and, as a result, shorter lifetimes as compared to Example 1. A cluster with $\kappa = 0.3$ in Example 2 will evaporate in 1/7 the time of a cluster with $\kappa = 0.3$ in Example 1 and 1/5 the time of a cluster with $\kappa = 1.0$ (the circular case).

Since cluster orbits are generally unknown, the degree of tidal truncation at pericenter cannot be directly inferred. So, in Example 3, we assume that an observed cluster lies at its average orbital radius for a range of eccentricity and is tidally limited for zero eccentricity. The mass within the pericentric inner

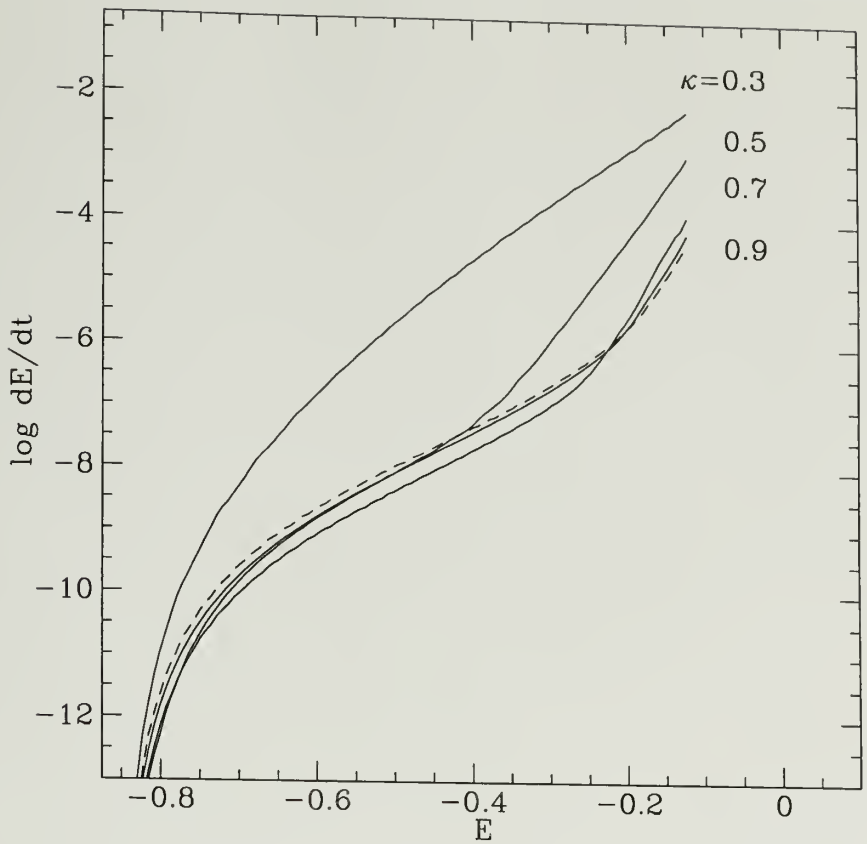

Figure 2.3. Heating rates for Example 3. Tidally-limited circular case (dashed line) is plotted for reference. For $\kappa = 0.7$, heating increases strongly in mildly tidally-unlimited cluster compared to Example 1. For $\kappa = 0.3$, distribution with $E > -0.3$ undergoes strong shocking on orbital time scale.

Lagrange point $M(x_p)$ can be substantially less than unity on eccentric orbits (Table 2.2). This leads to stronger heating than found on the same orbits in Example 1 (see Figure 2.3). For $\kappa = 0.7$ the heating rate is much larger than in Example 1 even though only small amounts of mass overlie x_p. For $\kappa = 0.3$ strong impulsive heating or bulge shocking (e.g. Aguilar et al 1988) occurs due to the increase in tidal amplitude.

Example 4 shows the dependence of heating rates on degree of tidal truncation for a fixed $\kappa = 0.3$ orbit. Figure 2.4 illustrates the dependence of heating on both

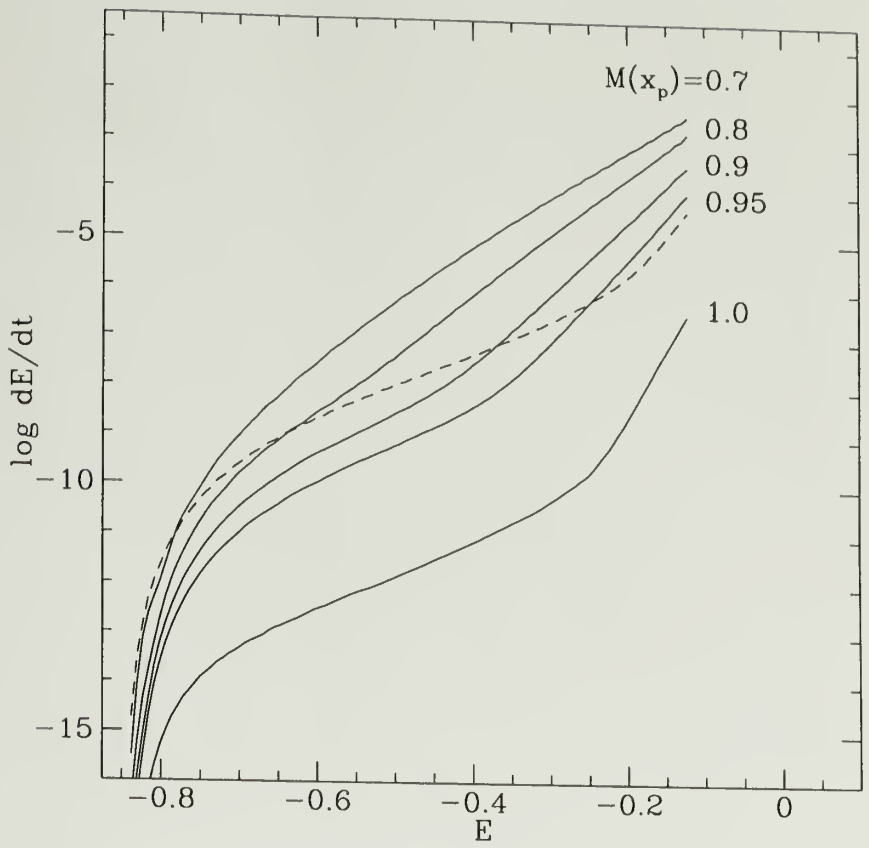

Figure 2.4. Heating rates for Example 4. Shocking develops slowly as $M(x_p)$ decreases. For $M(x_p) \sim 0.95$ heating of the tail is slightly stronger than in the tidally-limited circular case (dashed line). Heating at low energies is substantially less. Strong impulsive heating or bulge shocking of the tail of the distribution will occur for $M(x_p) < 0.9$.

κ and $M(x_p)$: significant heating will occur on orbital timescales for $\kappa = 0.3$ and $M(x_p) < 0.9$. Strong heating for $\kappa > 0.3$ will also occur because these orbits have larger heating rates for the same value of $M(x_p)$. Table 2.2 shows the variation in cluster size and dynamical time with tidal truncation, indicating the corresponding variation in mean density.

The evolutionary consequences of the heating rates in Example 4 are shown in Table 2.4. Clusters of different mass and concentration have equal $M(x_p)$ on the

Table 2.4. Bulge shocking evaporation times (Example 4)

$W_0 = 3$			$M(x_p)$		
$M_c\ (M_\odot)$	1.0	0.95	0.9	0.8	0.7
1.0×10^5	1.3	1.3	1.1	0.4	0.2
1.0×10^6	10.9	2.4	0.8	0.4	0.4

$W_0 = 5$			$M(x_p)$		
$M_c\ (M_\odot)$	1.0	0.95	0.9	0.8	0.7
1.0×10^5	1.4	2.4	2.1	1.0	0.5
1.0×10^6	11.4	12.1	5.2	1.5	0.5

$W_0 = 7$			$M(x_p)$		
$M_c\ (M_\odot)$	1.0	0.95	0.9	0.8	0.7
1.0×10^5	1.4	2.7	2.4	2.3	2.0
1.0×10^6	12.0	16.0	23.4	13.8	7.5

same orbit. Weakly bound clusters disrupt more easily because the resonances occur more deeply within the system. Survival of $W_0 = 3$ clusters decreases strongly with $M(x_p)$. Conversely, for small reduction in $M(x_p)$, survival of $W_0 = 5$ and $W_0 = 7$ clusters is enhanced as increased heating is offset by diminished relaxation. For $W_0 = 5$, maximum enhancement occurs at $M(x_p) \sim 0.95$. For $W_0 = 7$, higher binding energies lead to even longer lifetimes for more severe truncations. Further reductions in $M(x_p)$ eventually lead to rapid disruption due to strong tidal shocking.

These results define a rough criterion for bulge shocking: for $W_0 \leq 5$ and $\kappa > 0.3$, bulge shocking will occur for $M(x_p) < 0.9$. Disruption for fixed $M(x_p)$ and κ also implies disruption for larger κ because heating rates increase with κ. For $\kappa < 0.3$, bulge shocking requires even smaller $M(x_p)$ to cause disruption.

This series of comparisons establishes three important aspects of tidal effects on different orbits in a spherical potential: 1) low-eccentricity and circular orbit

heating for tidally-limited clusters strongly accelerate evolution; 2) high-eccentricity heating has little effect in tidally-limited cases but the high mean density found for typical orbital radii in the Galaxy leads to short relaxation and evaporation times; 3) high-eccentricity heating, or bulge shocking, becomes important when clusters are tidally-unlimited, although the exact effect depends on $M(x_p)$, κ, W_0 and M_c.

Finally, an important consequence of strong tidal heating is suppression of the gravothermal instability. Although this may cause expansion and disruption, relaxation slows the expansion and can still produce mass segregation (Figure 2.5). Therefore, *mass segregation does not necessarily imply core collapse*, a possibility that does not arise when neglecting external heating (e.g. Chernoff & Weinberg 1990; Drukier, Richer & Fahlman 1992). Observed clusters with King profiles and strong mass segregation (such as M71) may reflect the influence of strong tidal effects.

2.5.2 Influence of Mass Spectrum

The mass spectrum controls the rate of relaxation and interplay with external heating. Clusters with steep mass spectra or a narrow range of low mass stars have lower relaxation rates than do clusters with shallow mass spectra or a wide range in stellar mass (e.g. Chernoff & Weinberg 1990). Here we examine the competition between external heating and relaxation over a range in α and m_u in unheated and circularly heated tidally-limited clusters.

Circular heating reduces evaporation times over a range in α (Table 2.5). Roughly a factor of three reduction can occur for $\alpha = 3.35$. Differences between heated and unheated clusters increase with α because the slower relaxation rates at high α are more readily enhanced. In addition, for fixed mass and concentration, heating reduces differences in evaporation time which depend on α.

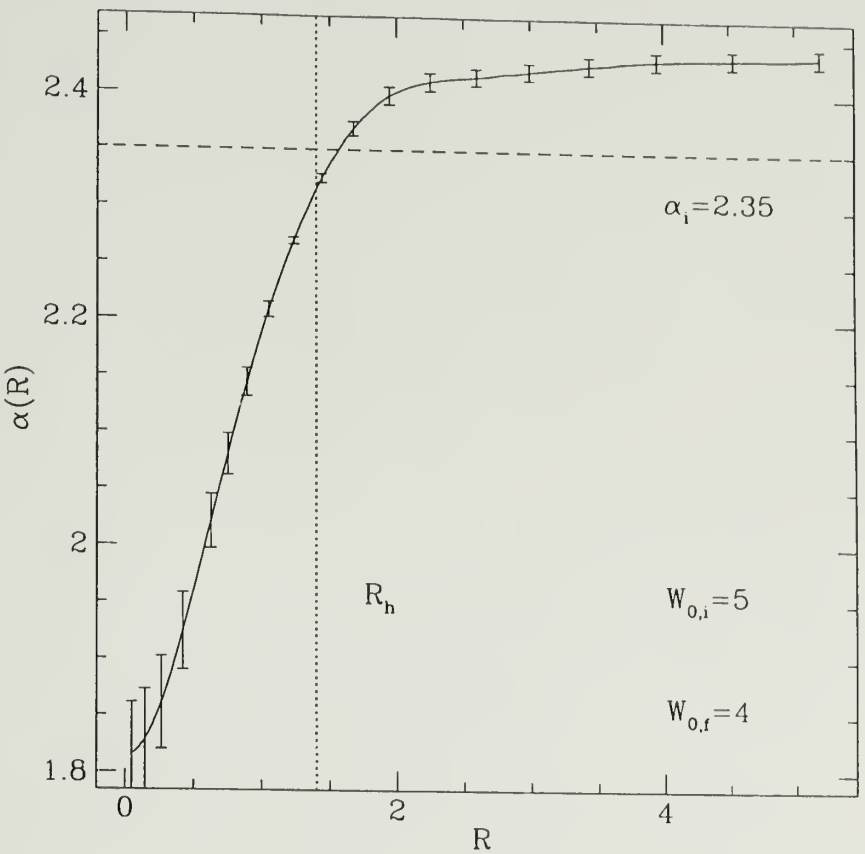

Figure 2.5. Radial dependence of mass spectral index in disrupting cluster. The cluster is dominated by bulge shocking with $W_0 = 5$, $M_c = 10^6 M_\odot$, $M(x_p) = 0.8$. α_i is the initial spectral index. R_h is the half-mass radius. Tidally disrupting clusters may show evidence of mass segregation. In this case bulge shocking suppresses core contraction, leading to expansion and disruption. The profile is approximately $W_0 = 4$ and the remaining mass is $M_c = 2.3 \times 10^5 M_\odot$.

Table 2.5. Times of core collapse and evaporation

$W_0 = 5$	α			
$M_c\ (M_\odot)$	1.35	2.35	3.35	
		t_{ev}		
5.0×10^5	2.7	3.2	5.3	heated
	4.4	6.3	14.1	unheated
1.0×10^6	4.3	5.2	8.2	heated
	8.6	12.3	25.9	unheated
		t_{cc}		
5.0×10^5	1.6	1.6	2.1	heated
	2.2	1.9	2.3	unheated
1.0×10^6	2.7	2.7	3.6	heated
	4.0	3.1	4.4	unheated

$W_0 = 7$	α			
$M_c\ (M_\odot)$	1.35	2.35	3.35	
		t_{ev}		
5.0×10^5	2.8	4.0	7.4	heated
	4.3	6.1	14.0	unheated
1.0×10^6	4.9	6.4	11.8	heated
	8.1	12.1	26.8	unheated
		t_{cc}		
5.0×10^5	0.56	0.37	0.41	heated
	0.59	0.37	0.38	unheated
1.0×10^6	1.06	0.71	0.76	heated
	1.06	0.71	0.76	unheated

$m_l = 0.1 M_\odot$, $m_u = 2.0 M_\odot$

Table 2.6. Mass at core collapse

$W_0 = 5$	α			
$M_c\ (M_\odot)$	1.35	2.35	3.35	
5.0×10^5	0.39	0.54	0.59	heated
	0.65	0.88	0.93	unheated
1.0×10^6	0.30	0.43	0.50	heated
	0.65	0.88	0.93	unheated
$W_0 = 7$	α			
$M_c\ (M_\odot)$	1.35	2.35	3.35	
5.0×10^5	0.82	0.90	0.92	heated
	0.93	0.98	0.99	unheated
1.0×10^6	0.78	0.87	0.90	heated
	0.93	0.98	0.99	unheated

$m_l = 0.1 M_\odot$, $m_u = 2.0 M_\odot$

Heating also reduces core collapse times t_{cc} up to 33% (Table 2.5) and masses remaining at core collapse up to a factor of two (Table 2.6). High concentration clusters maintain the same core collapse times in all cases but show decreased mass at core collapse.

The non-monotonic behavior of core collapse time with spectral index was also found by Inagaki (1985 Table II) in Plummer law initial profile and Chernoff & Weinberg (1990 Table 4) in King models. This indicates a complex relation between concentration, mass segregation and core collapse. Heating supresses this behavior for $W_0 = 5$.

Evaporation times decrease with increasing m_u (Figure 2.6). The decrease in t_{ev} with increasing mass range results from enhanced relaxation caused by a more extreme mass segregation instability. A 25% range in the duration of strong stellar evolution for $\alpha = 2.35$ gives a range in mass limits of $1.9 \leq m_u \leq 2.2$ and results in very small differences in evaporation time.

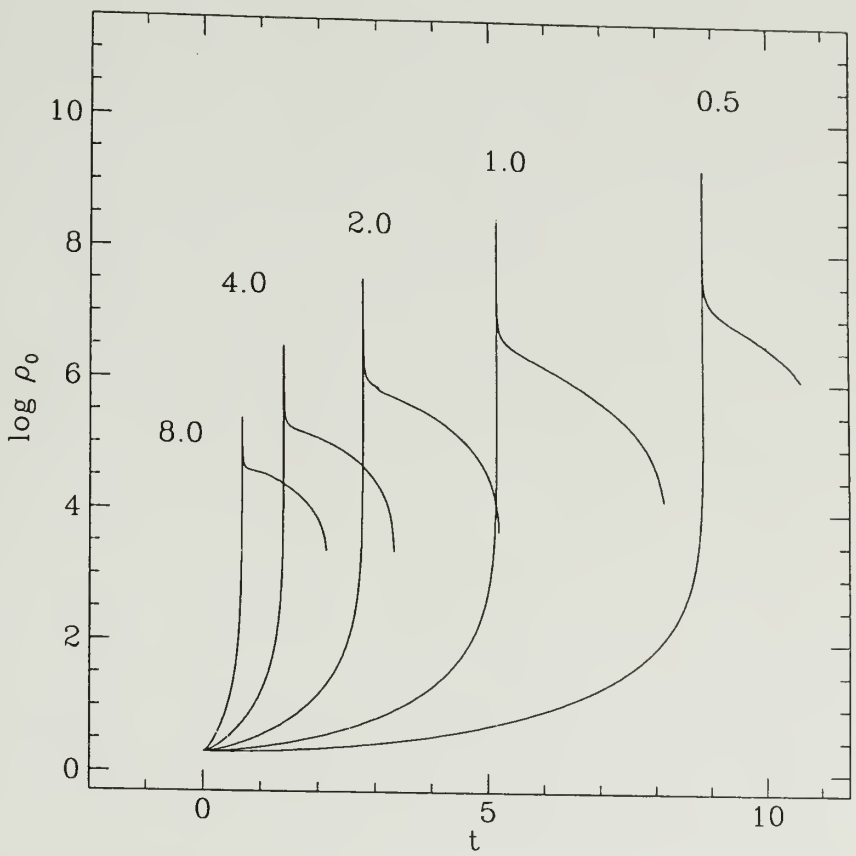

Figure 2.6. Dependence of central density evolution on range of internal stellar masses. Central density evolution for $W_0 = 5$, $10^6 M_\odot$ clusters on circular orbits with $\alpha = 2.35$, $m_l = 0.1$ and m_u as indicated. Evaporation occurs at the termination of each central density curve. Evaporation times vary by no more than 10% for the expected range $1.9 \leq m_u \leq 2.2$ in initial upper mass limit for $\alpha = 2.35$. Evaporation times decrease with increases mass m_u due to the enhanced mass segregation instability.

2.5.3 Influence of Anisotropy

Another internal property that determines the influence of external heating is the anisotropy of the stellar orbit distribution. Figure 2.7 shows the variation of heating rate with anisotropy radius within a cluster. Heating increases with anisotropy due to efficient impulsive heating of radial orbits at apocenter. However, heating rates for $r_a = 2.5$ unbind orbits with $E > -0.25$ in one orbital period t_{cr} and quickly alter the DF. The relaxation time is roughly 100 crossing times, so diffusion cannot maintain the assumed level of radial anisotropy in the cluster halo. We estimate that anisotropy radii of $r_a \geq 5.0$ are sustainable through relaxation. The interplay between heating and anisotropy seen here provides strong incentive to study the evolution of fully anisotropic DFs.

2.5.4 Evolution in the Milky Way

2.5.4.1 Scaled evaporation times

The dimensionless evaporation times for tidally-limited clusters discussed in §2.5.1 may be scaled to physical units using the following relation

$$t_{phys} = 1.1 \times 10^3 \bar{t} \times t_{ev}, \tag{2.16}$$

where $\bar{t}$ is the orbital period at the tidal radius

$$\bar{t} = \left(\frac{GM_c}{r_t^3}\right)^{-1/2} \tag{2.17}$$

and

$$r_t = \left(\frac{GM_c}{2\Omega_p'^2}\right)^{1/3}. \tag{2.18}$$

The quantity $\Omega_p'(\kappa, R_a)$ is the effective perigalactic angular frequency of an orbit of given κ and apocentric radius R_a due to tidal strain and centrifugal force (defined in Appendix A.2).

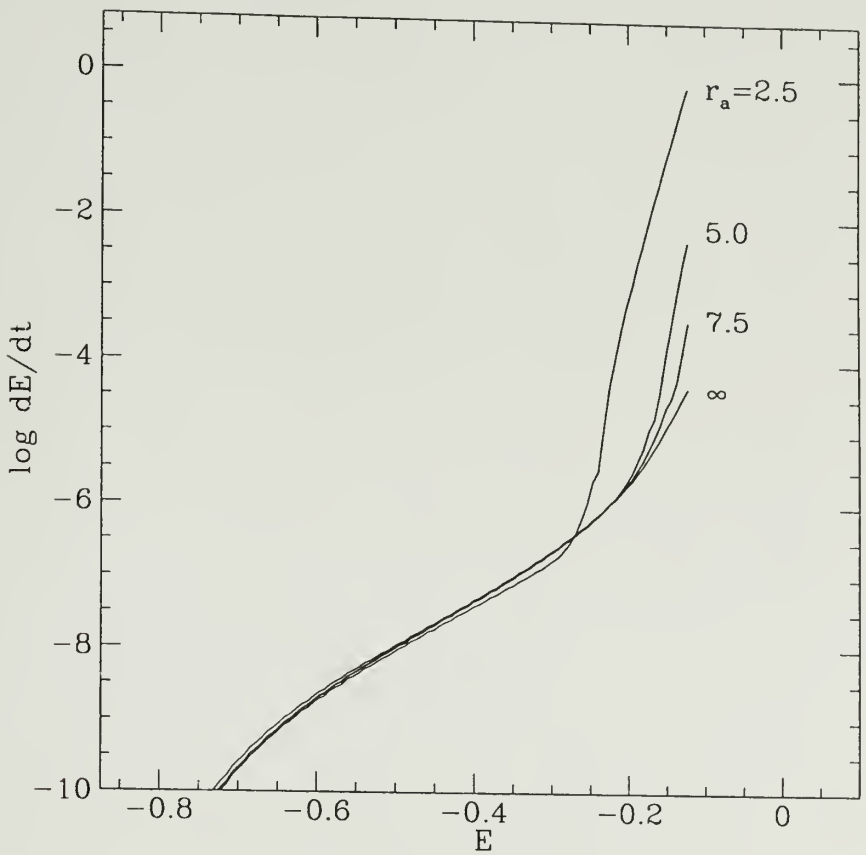

Figure 2.7. Heating rates for clusters with radial anisotropy. Heating rates are shown for clusters on circular orbits with indicated anisotropy radius. For $r_a = 2.5$, the anisotropy parameter $\beta = 1 - \bar{v}_\theta^2/\bar{v}_r^2 = 0.17$ at the half-mass radius. Energy input increases due to efficient impulsive heating of radial stellar orbits at apocluster.

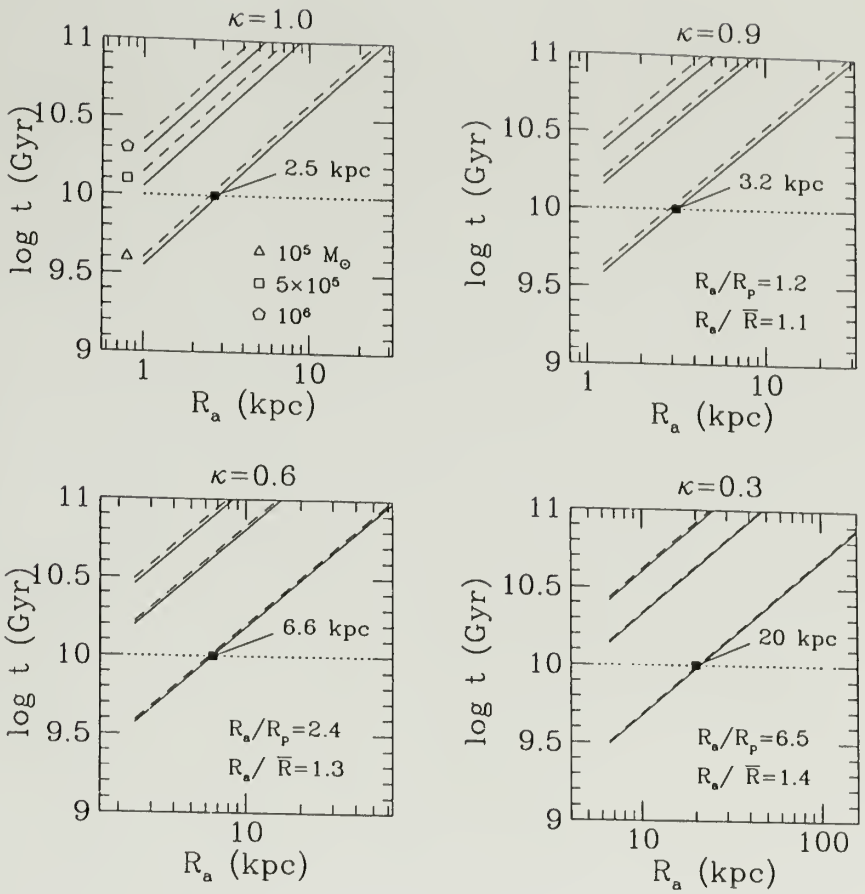

Figure 2.8. Evaporation times for tidally limited clusters. Evaporation times vs. apogalacticon for $W_0 = 5$ (solid) and $W_0 = 7$ (dashed). Low mass clusters evaporate within 10 Gyr in inner Galaxy to apogalactic radii as shown. Strong heating drives low eccentricity clusters to evaporation while high densities of tidal limitation drive high eccentricity clusters to evaporation. Evaporation of $\kappa = 0.3$, $10^5 M_\odot$ occurs out to average radii of 15 kpc.

As an example, the dimensionless evaporation times given in Table 2.3 are scaled to a range of apogalactica in Figure 2.8. Clusters evaporate over a wide range of Galactocentric radii depending on κ. In 10 Gyr, clusters on circular orbits evaporate within 3 kpc, while those on $\kappa = 0.3$ orbits evaporate out to average radii of 15 kpc.

2.5.4.2 Survival and disruption

Here we present a simple evolutionary scenario in which clusters form at apocenter with a range of mean density parameterized by $\rho_{crit,FR}(R)$, the Fall-Rees (1985) critical cloud density at Galactocentric radius R. This parameterization is chosen to allow normalization with respect to a particular model. Other models (e.g. Harris & Pudritz 1994; Murray & Lin 1992) can be similarly evaluated given expressions for initial protocloud densities as a function of Galactocentic radius. A range of density is used to define a range of $M(x_p)$ for clusters at each radius, thereby illustrating characteristics which are independent of any particular model. We only consider relaxation, external heating and binary heating although gas removal and stellar evolution will play an important role following formation. These effects should weaken the potential and increase disruptive tendencies described here.

In the first case, clusters form on eccentric $\kappa = 0.3$ orbits (e.g. Eggen, Lynden-Bell and Sandage 1962). Figure 2.9 shows the resulting pattern of survival, disruption and evaporation for 10^5 and $10^6 M_\odot$ clusters after 10 Gyr. Clusters initially with $10^5 M_\odot$ do not surive within $R_{av} = 15$, reflecting the evaporation times shown above. Lower density clusters suffer disruption to even larger distances. High mass clusters with $M(x_p) \lesssim 0.8$ can suffer disruption but none can evaporate.

Cluster formation on less eccentric $\kappa = 0.7$ orbits shows the same qualitative pattern of survival, evaporation and disruption as above (Figure 2.10). The consequences are less severe because the density contrast between formation at apocenter and tidal limitation at pericenter is not as great. In this case, low mass cluster survival is limited to regions beyond 5 kpc for clusters which are nearly tidally-limited.

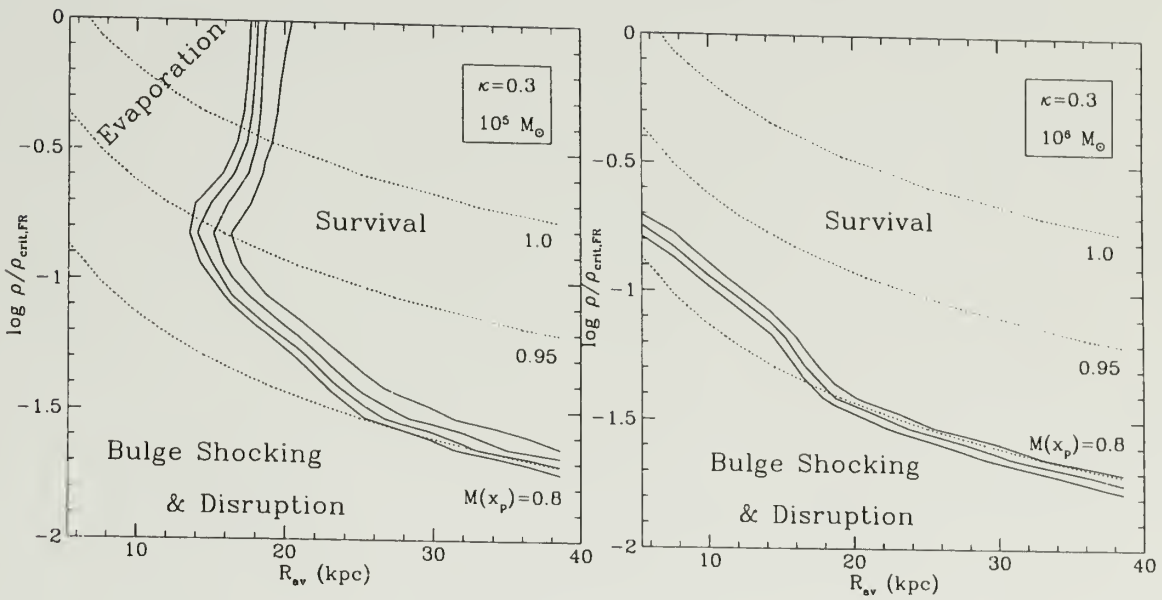

Figure 2.9. Bulge shocking of proto-clusters for $\kappa = 0.3$. Contours of log mass (solid) show survival and disruption of proto-clusters with an initial $W_0 = 5$ profile after 10 Gyr due to tidal effects on $\kappa = 0.3$ orbits. Contours are in the range $3.75 \leq \log M \leq 4.5$. R_{av} indicates average orbital radius and $\rho_{crit,FR}$ is the Fall-Rees (1985) critical cloud density at radius R. Dotted contours show lines of equal $M(x_p)$. Left: $10^5 M_\odot$ clusters with $\rho \approx \rho_{crit,FR}(R)$ evaporate due to high initial densities, lower density clusters disrupt from bulge shocking and clusters with $M(x_p) \sim 0.95$ survive longest due to balance between heating and relaxation. Right: a density of $0.1\rho_{crit,FR}$ leads to bulge shocking and disruption in $10^6 M_\odot$ out to $R_{av} \sim 10kpc$.

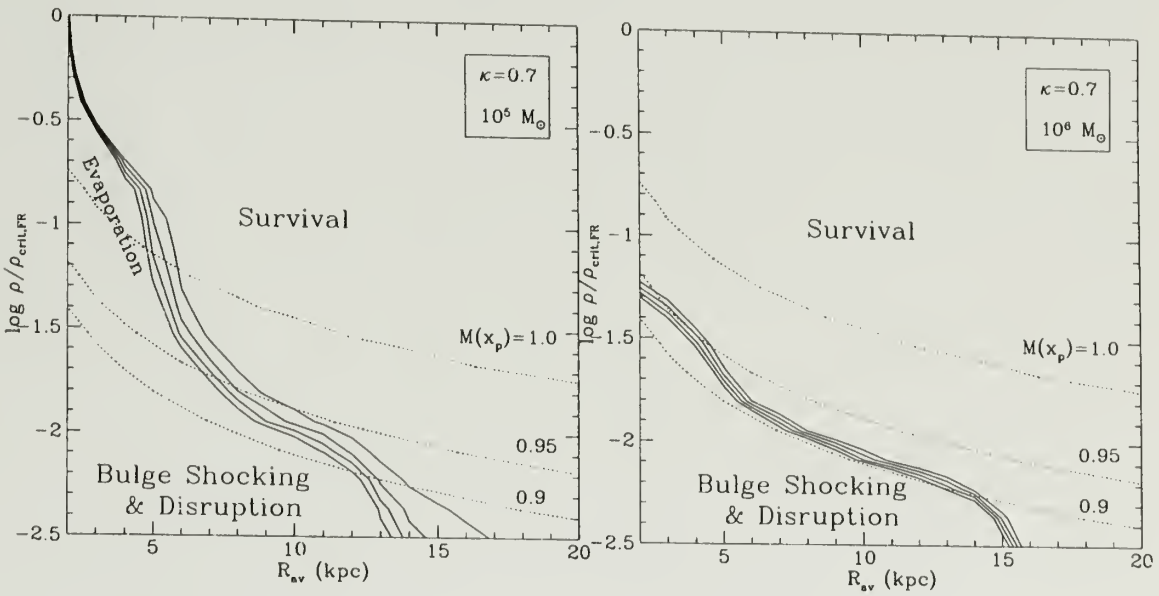

Figure 2.10. Bulge shocking of proto-clusters for $\kappa = 0.7$. As in Fig. 2.9 but on $\kappa = 0.7$ orbits. Left: high density $10^5 M_\odot$ clusters evaporate, low density clusters disrupt due to extreme tidal heating and clusters survive at larger radii. The convergence of contours into the upper left corner is a numerical artifact caused by mean densities beyond the range of our calculations. However, these clusters also evaporate because of the high densities. Right: low density clusters disrupt at densities roughly 30% of the mean density for tidal limitation out to 15 kpc due to strong tidal heating

2.6 Implications for Milky Way Clusters

The calculations presented above bear on our understanding of the observed mass and space distributions of Galactic globular clusters. We summarize some relevant properties for reference. In the Djorgovski (1993) compilation, 65% of 130 clusters with distance estimates lie within the solar circle. The overall peak of the luminosity function of Galactic globulars is $M_v = -7.36$ (Harris 1991) corresponding to a mass of $1.5 \times 10^5 M_\odot$ (where $M/L_v = 2$). The luminosity function varies little in this inner region.

Our results imply that the observed characteristics of this inner population have evolved with time. Because $10^5 M_\odot$ clusters evaporate or lose large amounts of mass in a Hubble time in the inner Galaxy, clusters at the peak of the luminosity function have evolved from higher mass. For example, at 6 kpc clusters on circular orbits with $M_v = -7.36$ will evolve to $M_v = -6.8$ in 10 gyr, losing roughly 40% of their initial mass. Inside the solar circle, clusters near the present peak had at least 30% more mass, depending on the orbit.

Many clusters will also have vanished. We predict that evaporation and disruption of $10^5 M_\odot$ clusters occur within 3 kpc for $\kappa = 1.0$ and within apocentric radii $R_a = 20$ kpc for $\kappa = 0.3$. For intermediate κ, the destruction region is bracketed by these limiting cases. These results buttress arguments based on two-body relaxation times that the shape of the luminosity function stems from evaporation and disruption of a larger initial population of low mass clusters (e.g. Larson 1996, Okazaki & Tosa 1995).

The dependence of survival on orbit implies that the kinematic distribution of clusters has evolved as well. Clusters on high eccentricity orbits in the inner Galaxy are least likely to survive due to both evaporation and bulge shocking. This suggests a decrease in the net velocity dispersion for the rotating system of metal-rich and inner halo metal-poor clusters (Zinn 1993). This tendency may also

partially account for observed differences between the kinematics of halo field stars and metal-poor globular clusters (e.g. Aguilar et al. 1988).

Finally, survival also depends strongly on initial cluster densities. Destruction is more pronounced for clusters with low initial density and low initial concentration due to bulge shocking. Bulge shocking can disrupt massive $10^6 M_\odot$ clusters on eccentric orbits out to 40 kpc provided $M(x_p) \lesssim 0.8$. However, a proper assessment of the initial distribution of cluster densities requires cosmogonical considerations.

We conclude that the segment of the cluster population which is native to the Milky Way or which was accreted at an early time represents a dynamically selected sample, with current masses, orbits and densities all favored for survival over a Hubble time of evolution. Tidal interaction with the Galactic disk will amplify these effects. Details will be described in a subsequent paper.

2.7 Summary

The key conclusions are as follows:

1. Time-dependent heating on low-eccentricity orbits accelerates evolution and sharply reduces evaporation times.

2. Tidally limited clusters on high-eccentricity orbits have high internal density, leading to short evaporation times even though heating rates are negligible.

3. Bulge shocking on high-eccentricity orbits can rapidly disrupt clusters over a wide range in mass and apogalactic radius when their densities are roughly a factor of 10 below the mean density required for tidal limitation.

4. Evaporation and disruption have shaped the mass, orbit and density distribution of clusters. In particular, clusters at the peak of the luminosity function had at least $\sim 30\%$ more mass depending on orbit. Evaporation on

high-eccentricity orbits has decreased the velocity dispersion in the cluster kinematic distribution.

Secondary results are as follows:

1. Evaporation times do not strongly depend on concentration in most cases. However, heating can lead to rapid disruption in massive clusters with low concentration because of the low binding energy and long relaxation time.

2. Clusters disrupting due to heating may still show signs of mass segregation due to continued relaxation.

3. Heating accelerates evolution over a range of mass spectral index and reduces the dependence of evaporation time on different initial mass spectra.

4. The development of anisotropy through relaxation in the core will increase evolutionary rates found in the isotropic distributions investigated here.

Chapter 3

Globular Cluster Evolution in M87 and Fundamental Plane Ellipticals

The globular cluster population in M87 has decreased measurably through dynamical evolution caused by relaxation, binary heating and time-dependent tidal perturbation. For fundamental plane ellipticals in general, cluster populations evolve more rapidly in smaller galaxies because of the higher mass density. A simple evolutionary model reproduces the observed trend in specific frequency with luminosity for an initially constant relationship.

Fits of theoretically evolved populations to M87 cluster data from McLaughlin et al. (1994) show the following: 1) dynamical effects drive evolution in the initial mass and space distributions and can account for the large core in the spatial profile as well as producing radial-dependence in the mass spectrum; 2) evolution reduces S_N by 50% within 16 kpc and 35% within 50 kpc, implying that S_N was initially 26 in this region. We estimate that 15% of the 'missing' clusters lie below the detection threshold with mass less than $10^5 M_\odot$.

3.1 Introduction

Observations of some giant elliptical galaxies reveal globular cluster systems which appear more extended than the host (Harris 1991). A particularly well-documented example belongs to M87 with a core radius of 7 arc sec and a cluster system with a core radius of 1 arc min (McLaughlin 1995). However, because a cluster population evolves dynamically due to both internal and external processes, the currently observed population almost certainly differs from the primordial one, complicating the interpretation.

Researchers have attempted to explain the extended core of the M87 cluster distribution as the evolved remnant of an initial profile which more closely resembled the light. However, neither dynamical friction nor shocking by a compact nucleus can fully account for this feature. Lauer & Kormendy (1986) found that a dynamical friction induced inflow can broaden an initially peaked spatial distribution but not at the observed scales. Ostriker, Binney & Saha (1989, hereafter OBS) subsequently determined that nuclear tidal disruption is viable only if clusters formed exclusively on box orbits.

Another potential mechanism is cluster evaporation through dynamical evolution. Recent work in this area demonstrates that evaporative mass loss driven by relaxation and heating due to a time-varying tidal field can lead to strong evolution of the Milky Way cluster population in a Hubble time (Weinberg 1994, Murali & Weinberg 1996, hereafter MW). In this paper, we examine these influences on cluster evolution in the dense inner regions of M87 and find that they produce the observed flattened profile from a peaked initial distribution over a wide range of initial conditions. Direct estimates of initial conditions using dynamically evolved parametric models of the spatial distribution and cluster mass function indicate that roughly 35% of the initial population dissolves or evolves below the detection threshold leaving the large core as a result. Furthermore, the decay in the size of the cluster population corresponds to a decrease in the specific frequency of globular clusters, S_N, which denotes the number of clusters per unit galaxian luminosity with L measured in units of $M_v = -15$.

The high values of S_N found in giant ellipticals have become a key point in galaxy formation arguments and suggest, for example, that the cluster system formed along with M87 (e.g. Harris 1991; van den Bergh 1995). Here we show that cluster systems decay more rapidly in less luminous fundamental plane ellipticals; this leaves larger values of S_N in luminous galaxies at the present epoch even if all

ellipticals begin with equal S_N. Our results thus provide at least a partial explanation for the observed trend of S_N with L.

The plan of the paper is as follows. We summarize our choices for the cluster population and the mass model for M87 in §3.2. The assumptions and method for dynamically evolving the population is presented in §3.3. The main results, the statistical comparison of the observed clusters to the theoretical models, is presented in §3.4. This includes an exploration of the evolutionary trends, best fit spatial profiles and mass functions, and an inference of the primordial population. In §3.5, we discuss the discuss the importance of the fundamental plane properties on the observed relation between specific frequency and luminosity A summary is given in §3.6.

3.2 Cluster population

We assume that the cluster population formed in an initial burst approximately 11 Gyr ago. Stellar evolution dominated cluster evolution for the first Gyr for a Salpeter IMF ($\beta = 2.35$) with $m_l = 0.1\,\mathrm{M}_\odot$, corresponding to the main sequence lifetime of $2\,\mathrm{M}_\odot$ A-star. Our zero-age population represents the epoch when, approximately 10 Gyr ago, relaxation, external heating and core collapse heating began to drive cluster evolution.

The fiducial calculations represent zero-age clusters as $W_0 = 5$ King models. Comparison calculations using $W_0 = 7$ clusters show nearly identical evolution over the long time scales of interest, in agreement with the results of MW where overall evaporation times were found to depend weakly on concentration in the range $5 \leq W_0 \leq 7$. We expect similar trends in evolution for $W_0 = 3$ clusters (c.f. MW), except in high mass, low-eccentricity cases where tidal heating leads to rapid disruption. These clusters enhance the destruction rate described below, but constitute a very small fraction of expected initial populations.

Table 3.1. Cluster Initial Conditions

Structural parameters		Fiducial value
M	total mass	$10^5 \leq M_c \leq 5 \times 10^6 M_\odot$
W_0	King concentration parameter	$W_0 = 5, 7$
R_T	cluster limiting radius	tidal limitation
Mass spectral parameters		
β	mass spectral index: $N(m) \propto m^{-\beta}$	$\beta = 2.35$ (Salpeter)
m_l	lower mass limit	$m_l = 0.1$
m_u	upper mass limit	$m_u = 2.0$
Orbital parameters		
E	orbital energy	isotropic orbit
κ	relative ang. mom.: $J/J_{max}(E)$	distribution

Each cluster is tidally limited on its orbit in the host. While initial cluster densities may differ from the mean density required by perigalactic tidal limitation, subsequent evolution during the first Gyr leads rapidly to tidal truncation or disruption. The limiting or *tidal* radius R_T is uniquely determined by the cluster mass and orbit. Table 3.1 summarizes the choice of parameters for individual clusters.

To represent the cluster mass distribution, $\nu(M, r)$, we use pure power laws (e.g. Harris & Pudritz 1994), power laws whose exponents have a linear dependence on radius, and a Gaussian magnitude distribution (e.g. McLaughlin, Harris & Hanes 1994, MHH). Power law mass distributions have been proposed on physical grounds by Harris & Pudritz (1994) while the Gaussian is commonly used as a convenient fitting function for the observed cluster luminosity function. To represent the spatial distribution of the cluster population in the primary, we use power law densities with and without a core derived from isotropic distribution functions, $f(E)$. Orbital isotropy is assumed due to lack of observational constraint.

Adopted models are given by joint distributions $\nu(M, r) \times f(E)$ and are summarized in Table 3.2. The Model 1 and Model 2 families use power law mass

Table 3.2. Population models

Designation	$\rho(r)$	$\nu(M)$	Parameters
Model 1a	$\rho_0 r^{-\eta}$	$M^{-\alpha}$	η, α
Model 1b	$\rho_0 r^{-\eta}$	$M^{-(\alpha+Kr)}$	η, α, K
Model 1c	$\rho_0(r_c^2+r^2)^{-\eta/2}$	$M^{-\alpha}$	η, r_c, α
Model 1d	$\rho_0(r_c^2+r^2)^{-\eta/2}$	$M^{-(\alpha+Kr)}$	η, r_c, α, K
Model 2a	$\rho_0 r^{-\eta}$	$e^{-(V-V_0)^2/2\sigma_V^2} \cdot dV/dM$	η, V_0, σ_V
Model 2b	$\rho_0(r_c^2+r^2)^{-\eta/2}$	$e^{-(V-V_0)^2/2\sigma_V^2} \cdot dV/dM$	η, r_c, V_0, σ_V

and Gaussian magnitude distributions respectively. Within each family, successive models have additional parameters to explore varying core sizes and radial dependence of the mass spectral index. Detailed derivation of models from the underlying distribution function is given in Appendix B.1.

Finally, we represent the potential of M87 as a singular isothermal sphere, with rotation velocity $v_0 = 606\,\mathrm{km\,s^{-1}}$ (e.g. OBS), velocity dispersion $\sigma = 350\,\mathrm{km\,s^{-1}}$, and assume a distance of 16 Mpc (van der Marel 1992). This defines a length scale of 77.6 pc per second of arc. Further discussion of potential and distance scale is given in Appendix B.2.

3.3 Cluster evolution

Competition between internal relaxation and heating due to external forcing may dramatically affect a cluster's evolutionary time scale and survival history. In addition to impulsive heating of a cluster halo—in a gravitational bulge shock, for example—resonances between the cluster's own orbital motion and internal stellar trajectories may heat cluster stars beyond the limit set by adiabatic invariance (Weinberg 1994). For tidally-limited clusters resonant heating on low-eccentricity orbits and tidal limitation on high-eccentricity orbits drive rapid cluster evolution and evaporation (see MW for details). The strength of these effects motivates this study.

The evolution of individual clusters includes two-body relaxation in the one-dimensional Fokker-Planck approximation (e.g. Cohn 1979), external heating due to the time-varying tidal field (MW), and a phenomenological binary heating term (e.g. Lee et al. 1991).

We take advantage of the scale-free galaxian profile by fixing orbital energy E of all clusters, choosing an initial grid of tidally-limited clusters in $\kappa = J/J_{max}(E)$ and mass, and computing the evolution to complete evaporation. The quantity $J_{max}(E)$ denotes the maximum angular momentum of an orbit with energy E. This grid may then be scaled to all desired orbital energies. The time evolution of the space density for the entire population is then constructed by determining the phase space distribution at the desired time using the evolutionary calculations and projecting appropriately.

Although we specifically consider M87, the results apply to any elliptical with similar profile. For example, we can scale evolution to any fundamental plane elliptical. Because the period decreases with mass, the same initial population will be more evolved for smaller mass primaries (see §3.5 for more discussion).

3.4 Results

3.4.1 Evolution of the core

An initially peaked cluster distribution develops a flattened core through dynamical evolution of individual clusters, as shown in Figure 3.1. In the dense regions of the inner galaxy, rapid mass loss due to relaxation and tidal heating can cause complete evaporation of a cluster or drive it below the observational limit. Rapid relaxation results from the high densities imposed by tidal limitation while tidal heating strongly enhances evaporation rates on low-eccentricity orbits. The resulting profiles are similar to the profile derived in McLaughlin (1995).

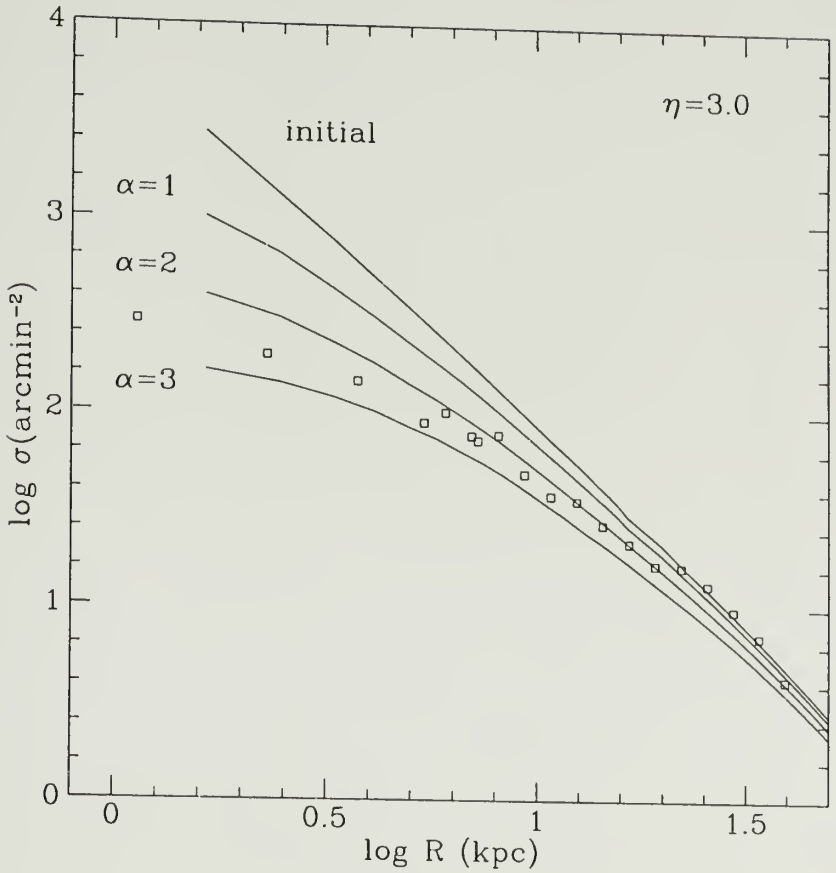

Figure 3.1. Surface density of evolved cluster system. Surface density inferred from observations (open squares) compared to Model 1a for indicated values of mass spectral index α and initial r^{-3} ($\eta = 3$) profiles (solid curves). Rapid evolutionary rates of low mass clusters produce flatter cores for larger α.

The overall shape of the evolving profile depends on both the initial mass and space distribution of the clusters. Consider the following limits. For a fixed spatial profile, a distribution rich in low mass clusters evolves rapidly due to short evaporation times while for a fixed mass distribution, a sharply peaked spatial profile develops a smaller core than a shallow profile. Taken together, the two trends produce a correlation between the inferred initial mass distribution and density profile: a large population of low mass clusters can rapidly flatten a steep initial profile while, conversely, a large population of high mass clusters allows a flatter initial profile to evolve slowly to the same final shape. Observations of the cluster mass distribution will distinguish between the different initial conditions.

3.4.2 Estimates of initial conditions

The evolved cluster populations described in §3.3 are compared to observed cluster data[1] using a maximum likelihood estimator which combines model and background surface densities with incompleteness measurements. The background surface density is taken to be 6.33 per arcmin^2 with a uniform luminosity function (MHH). Point sources lie in the region $1.21' \leq R \leq 7'$ (the field edge), centered on M87, with apparent limiting magnitude $V = 24$. We use a mass-to-light ratio $(M/L)_V = 2$ to convert luminosity to mass. Note that larger M/L will shift the population to higher mass, implying less evolution, while smaller M/L will have the opposite effect. For $R < 1.21'$, the authors provide 3 binned points (McLaughlin 1995). A joint χ^2-likelihood estimator is used to include all data points. Details of the estimation procedure are provided in Appendix B.3.

We fit both dynamically evolved distributions and unevolved distributions based on the models presented in Table 3.2. In the case of dynamically evolved models, the quoted values represent initial conditions (labeled by 'initial'). In the

[1]The data have been kindly supplied by McLaughlin & Harris (1995)

Table 3.3. Model 1 fits

Epoch	η	σ_η	r_c	σ_{r_c}	α_0	σ_{α_0}	K	σ_K	-log L
					Model 1a				
initial	2.76	0.04	-	-	1.95	0.03	-	-	69502.9
					Model 1b				
initial	2.66	0.06	-	-	1.68	0.09	0.01	0.004	69501.3
					Model 1c				
present	3.09	0.13	7.30	0.79	1.73	0.04	-	-	69500.6
initial	3.03	0.12	5.67	0.94	1.93	0.04	-	-	69499.8
					Model 1d				
present	3.06	0.13	7.34	0.81	1.30	0.08	0.028	0.002	69480.9
initial	3.13	0.10	5.70	0.40	1.61	0.10	0.014	0.004	69492.8

Table 3.4. Model 2 fits

Epoch	η	σ_η	r_c	σ_{r_c}	V_0	σ_{V_0}	σ_V	σ_{σ_V}	-log L
					Model 2a				
initial	2.77	0.05	-	-	-7.11	0.17	1.16	0.08	69487.2
					Model 2b				
present	3.10	0.13	7.32	0.80	-7.33	0.10	1.08	0.07	69468.7
initial	3.14	0.12	5.14	0.77	-7.07	0.17	1.19	0.08	69485.3

case of unevolved models, the quoted values represent the best fit parameters at the present epoch (labeled by 'present'). Only models with cores are considered in the present epoch fits because coreless models poorly represent the data.

Tables 3.3 and 3.4 present the best estimates and their variances (cf. Table 3.2). Comparison of present epoch and initial parameter estimates illustrates several expected evolutionary trends. The core of the distribution grows due to the depletion of clusters in the inner regions of the galaxy. The power law index α decreases, while the Gaussian magnitude peak V_0 and slope K of the radially-dependent power law both increase as a result of the selective evaporation of lower mass clusters. The increase in K also indicates that depletion occurs primarily in the inner regions. The following cases show specific features of these trends.

We plot the marginal probability density in V_0 and σ_V for Model 2b in Figure 3.2. The best estimate for V_0 decreases with time as low mass (and therefore high

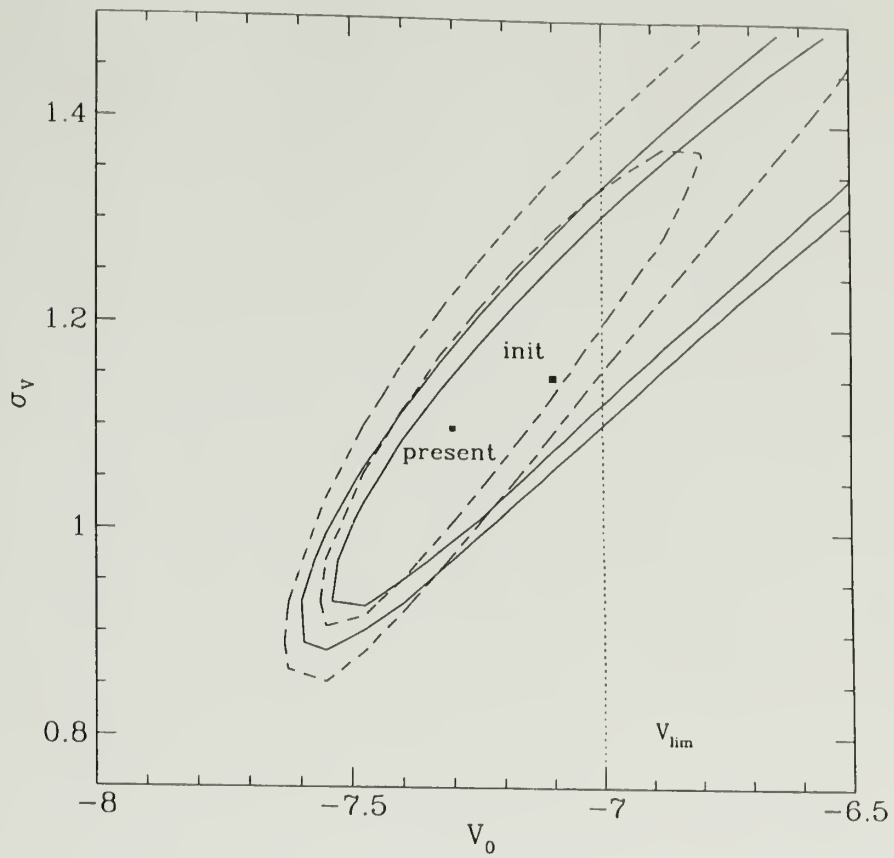

Figure 3.2. Confidence levels for V_0 and σ_V. 95% and 99% confidences for marginal density in V_0 and σ_V for present (dashed) and initial (solid) Model 2a fits. Points indicate best-fit values. Vertical line shows magnitude limit.

V) clusters disappear. However, the assumption of identical initial and present epoch values cannot be ruled out since the values of V_0 are only weakly inconsistent (cf. Table 3.4). The lack of constraint could result from the shallow magnitude limit of the data. Both fits are consistent with distributions which peak below the limiting magnitude of $V = -7$.

Model 1d suggests that there is radial dependence in the mass distribution (Fig. 3.3). Both present epoch and initial fits are inconsistent with a constant mass spectral index ($K = 0$) and indicate that dynamical evolution has enhanced

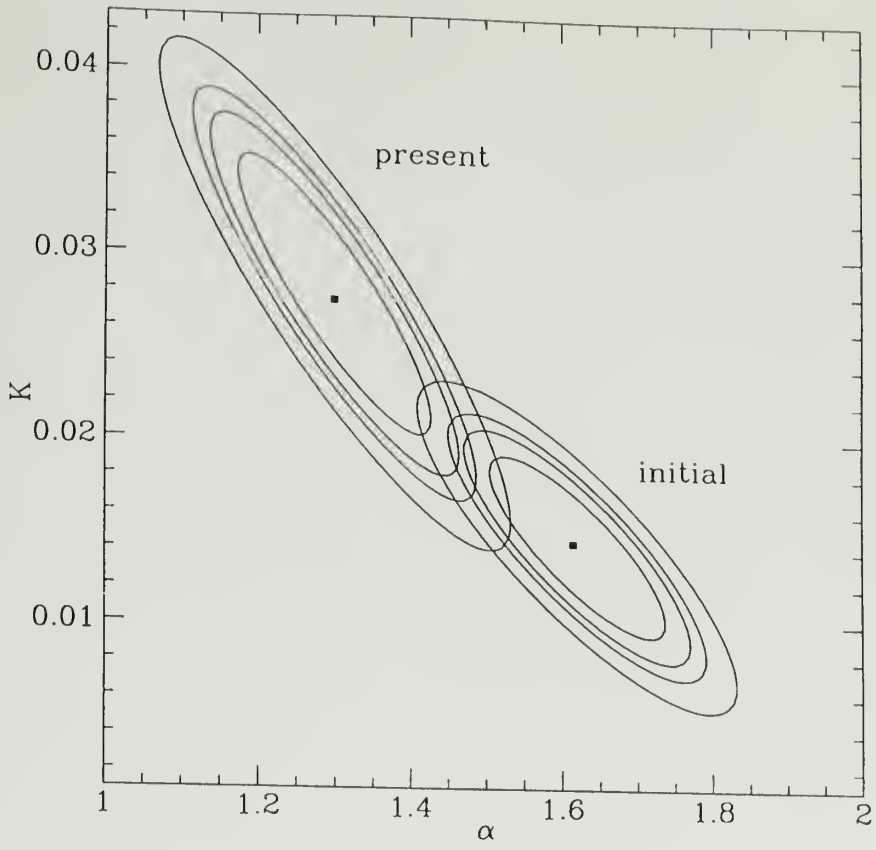

Figure 3.3. Confidence levels for α and K. 75%, 90%, 95%, and 99% confidences for marginal density in α and K for present epoch and initial Model 1d fits. Points mark best-fit values. The initial spectral index shows mild radial dependence increasing from a central value of 1.61 to 1.97 at 30 kpc in the best-fit case.

the radial dependence. In the core region, the present index $\alpha \approx 1.4$. We note that these results conflict with those of MHH and McLaughlin & Pudritz (1996), who find no radial dependence in the mass distribution.

3.4.3 Comparison of models

The previous section examined the results of trends in the evolution of the cluster population within several model families. Here, we identify the best overall

representation among the initial models after 10 Gyr of evolution using a generalized likelihood ratio test (e.g. Martin 1971).

The final column in Table 3.3 shows that the most general model gives a better estimate in each case, as expected. In particular, Model 1c can be rejected in favor Model 1d, a result which is consistent with the confidence surfaces for the radially-dependent mass spectrum plotted in Figure 3.3.

Model 2b generalizes Model 2a by introducing arbitrary *initial* core size. A finite core does provide a better estimate but zero core (Model 2a) cannot be rejected. Figure 3.4 compares the surface density profiles of these two models. The Model 2b fit falls below the observed profile at small radii due to the shallow initial core. However, the binned surface density points have relatively low weight in the full data set. The good fit of Model 2a to the inner data points suggests that a more peaked initial distribution may provide the optimal fit. The use of individual cluster counts in this region should help provide the necessary constraint. The deviation of the present epoch fit from the data further suggests that evolution plays an important role in shaping the profile.

Finally, we compare the most general power law mass function model, Model 1d, with the most general Gaussian magnitude model, Model 2b, by constructing a linear combination of both spaces and searching for the global maximum. The maximum occurs at the best-fit parameters for Model 2b: the Gaussian magnitude distribution describes the data significantly better than any power law mass distribution. As discussed above, the Gaussian may be poorly constrained by the limiting magnitude of the data. However, examination of the estimated functions shows that the power law is more peaked at low mass than the Gaussian both initially and finally, while the Gaussian has more weight at high mass. These differences in shape also lead to the statistical preference of the

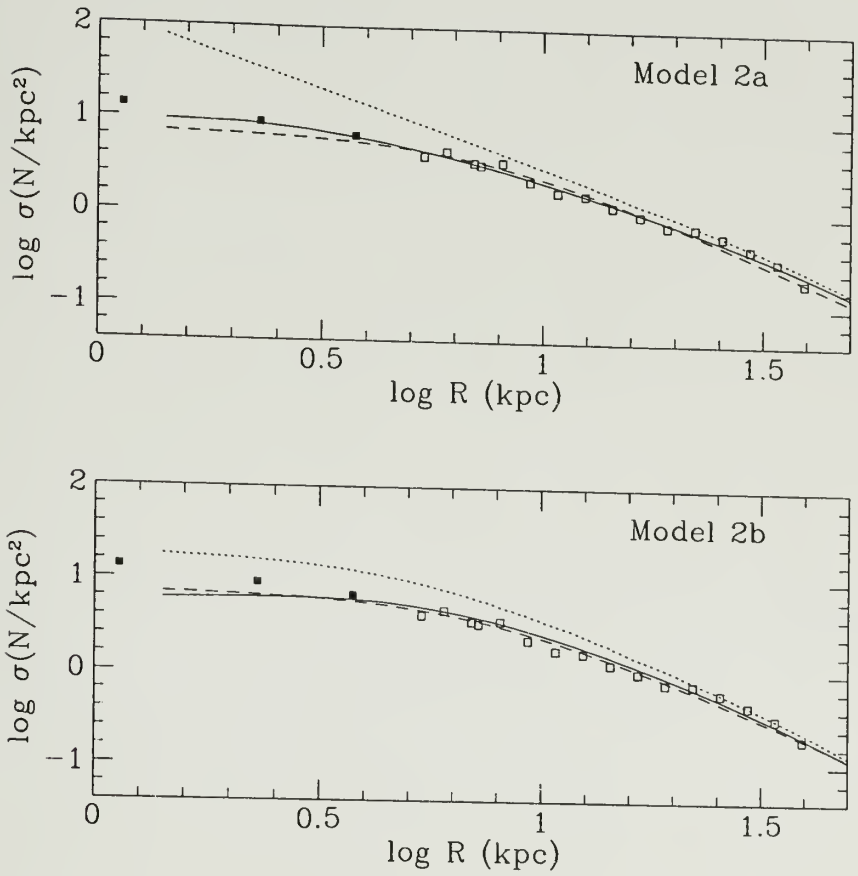

Figure 3.4. Comparison of Model 2a and 2b surface densities. Comparison of predicted surface density profiles (solid) with binned data. Initial profiles (dotted) and present epoch Model 2b fits (dashed) are also plotted. Both the model with initial core and the present epoch fit deviate from the data in the inner region.

Table 3.5. Evolved model comparisons

test	$-2\ln\lambda^{\flat}$	$\nu^{\sharp}$	accept	reject	confidence
1c–1d	14.0	4		√	99%
2a–2b	3.8	4	√		60%
1d–2b	15.0	7		√	96%

$^{\flat}-2\ln\lambda$ is likelihood ratio
$^{\sharp}\nu$ is number of degrees of freedom

Gaussian luminosity function over the spatially constant power law and its radially-dependent generalization.

Table 3.5 summarizes the conclusions of the tests comparing the initial conditions and lists the likelihood ratios and confidence values. In the first two cases, the likelihood ratios follow directly from Tables 3.3 and 3.4. In summary, we find that the initial Gaussian magnitude distribution best describes the data, but that we cannot distinguish between singular density profiles and densities with core. Both conclusions may result from insufficient data.

3.4.4 Evolution of the initial population

From the derived initial conditions, we plot the projected cumulative distribution of clusters initially within 50 kpc or $6.5R_e$ (Figure 3.5). The initial population in this region is about 7250 for Model 2a, a factor of 1.6 larger than the presently observed population of 4500. For Model 2b, the initial population size is smaller, but still in excess of 6000. Evolved clusters will also be found at masses below the observational limit. Within 16 kpc, about 500 evolved clusters are expected in the range $24 > V > 24.5$ ($10^5 > M > 7 \times 10^4 M_\odot$). All other clusters in this region initially in this mass range will have evaporated.

This implies that the specific frequency, S_N, evolves with time. Using the ratio of final to initial surface densities from the models, we derive the run in initial specific frequency at radius R, $S_N(R)$ (Figure 3.6). As expected, depletion in the

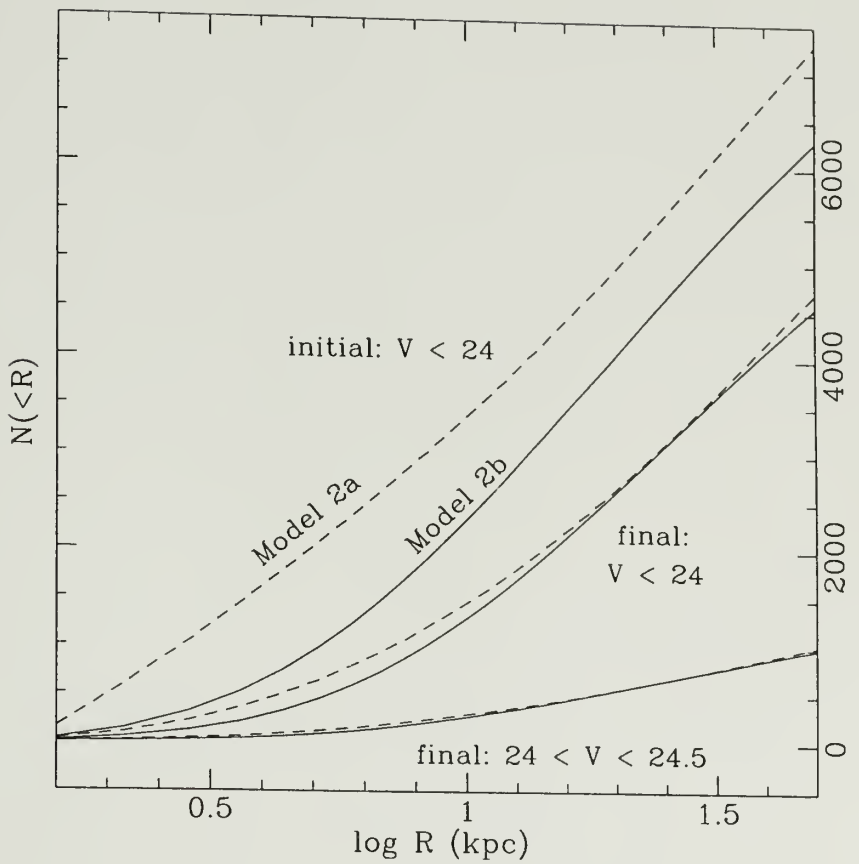

Figure 3.5. Estimated initial and observed distributions of clusters in M87. Estimated cumulative distribution of clusters for projected radius $R < 50\,\mathrm{kpc}$ ($6.5R_e$). Initial distributions for Model 2a (dashed) and Model 2b (solid) are shown for $V < 24$ (upper pair). Final distributions are shown for $V < 24$ (middle pair) and for $24 > V > 24.5$ (bottom pair). Clusters with $24 > V > 24.5$ began with $V < 24$. Approximately 50% of the initial clusters vanish within (16 kpc) $2R_e$ and 35% within $6.5R_e$ for Model 2a.

inner regions dominates; however, $\sim 10\%$ change in $S_N(R)$ occurs even out to 50 kpc due to the rapid evolution of low-mass clusters.

Model 2a in Figure 3.5 shows a 35% change in total S_N within 50 kpc due to depletion. The observed total value $S_N \approx 17$ in this region (MHH) implies an initial value of 26.5. Thus even the enormous observed value of S_N has diminished significantly due to evolution (this neglects the intrinsic evolution in galaxy luminosity due to stellar evolution). The time evolution of the total S_N is shown directly in Figure 3.7. The decay of the cluster population is approximately exponential in time with e-folding times of 20 Gyr and 40 Gyr for measurements within 16 and 50 kpc, respectively.

Our comparison applies to clusters in specified mass and radial ranges in a galaxy. Quoted specific frequency values are extrapolated over unobserved ranges from data taken within such limits. In the case of M87, MHH find $S_N = 17.7$ directly from the observations, while extrapolation yields a total $S_N = 14.4$ for the whole galaxy. Their extrapolation of the luminosity function over all magnitudes yields a total correction of 2.2 to cluster counts in the observed magnitude range. For $R < 42$ kpc, using this correction they estimate a total ~ 9400 clusters (3729 observed in galaxy+cD envelope, 500 in core, $\times 2.2$) which is 70% of the total number of clusters estimated over all radii. The estimated initial distribution has a larger correction because it is weighted more heavily to low mass (c.f. §3.4.2). Since most of these clusters completely evaporate, this implies even greater evolution in specific frequency than derived here.

3.5 Discussion

Our conclusions ignore the possibility that recent merger and accretion events have have strongly contaminated the initial cluster population. Merging of gas-rich galaxies is expected to produce clusters with strong central concentration (Zepf &

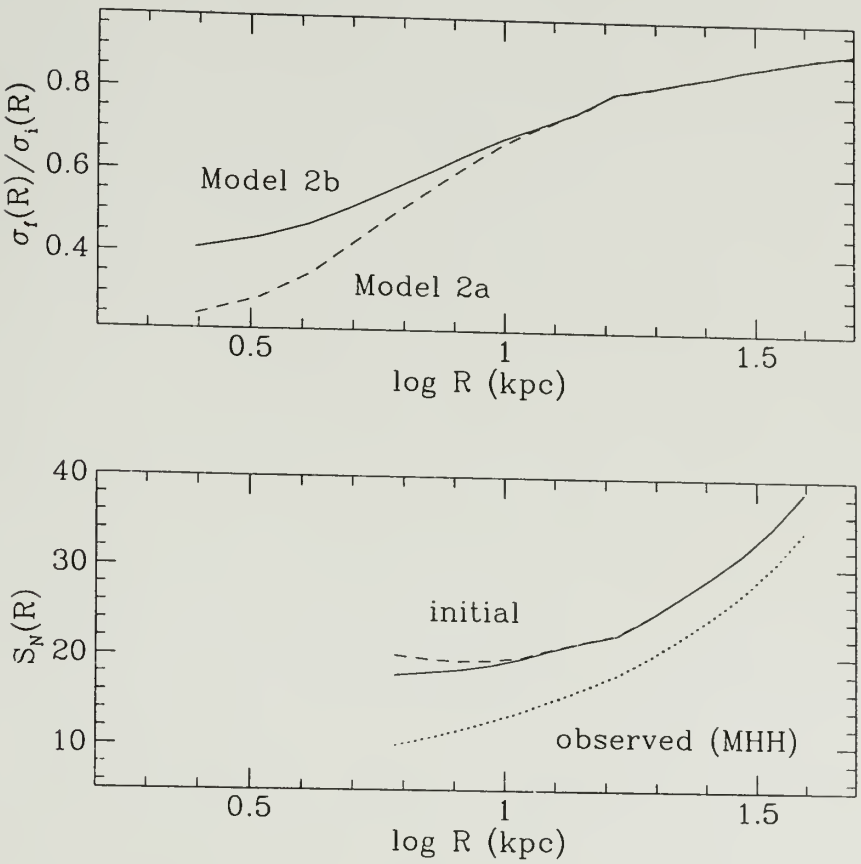

Figure 3.6. Ratio of final to initial cluster system surface density. The ratio of final to initial surface density (top) in Models 2a (dashed) and 2b (solid) and the run in initial specific frequency at R ($S_N(R)$) for each model (bottom) derived from the observed values given by MHH (dotted). Evolution reduces S_N by 35% in Model 2a.

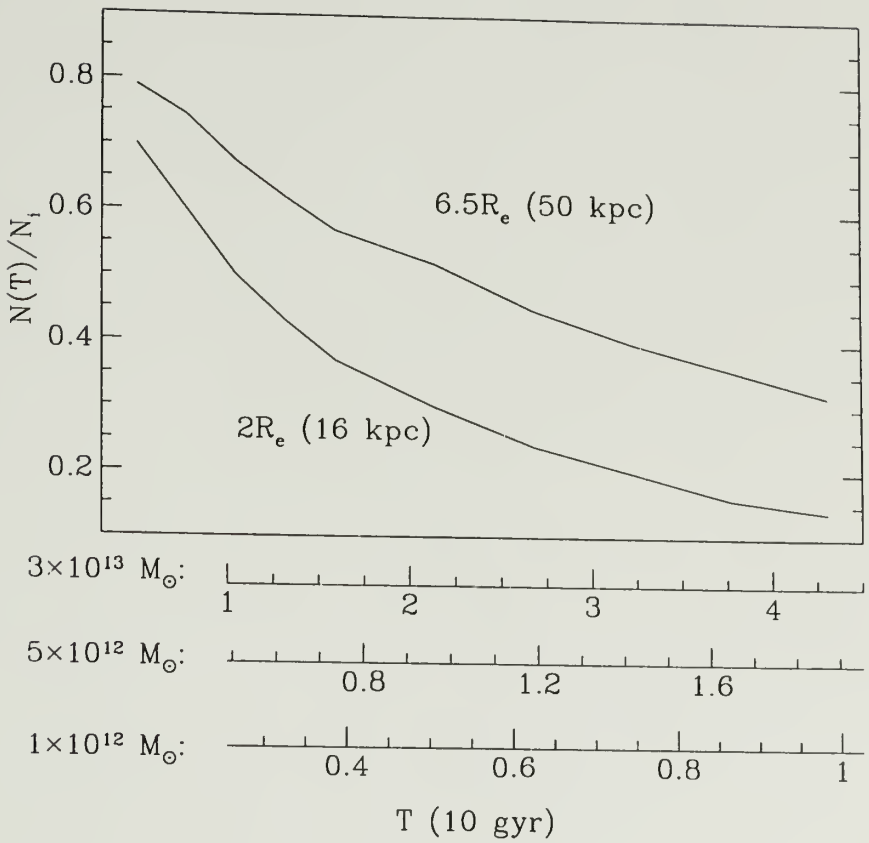

Figure 3.7. Fraction of clusters surviving as a function of projected radius. The fraction of clusters remaining within the indicated projected radius as a function of time. Abscissae indicate time units which correspond to fundamental plane scaling for galaxies with indicated masses. Top axis gives M87 scaling (other axes will be discussed in the next section). Initial S_N is ≈ 21 measured within 16 kpc and 26.5 measured within 50 kpc and decays with the cluster population.

Ashman 1993; Mihos & Hernquist 1994), but the large core of the distribution itself argues against any recent merger which has produced significant numbers of young clusters. Thus either cluster-producing mergers in M87 have occurred long in the past or not at all.

The recent addition of clusters through satellite accretion is also unlikely to account for a significant fraction of the observed population. For example, accretion of Milky Way-type spirals can only account for about 25% of the observed population, assuming that the $4L_*$ luminosity of M87 ($R < 40\,\mathrm{kpc}$) comes entirely from satellites (Lauer 1988). Assuming that material is stripped when the mean density of the primary exceeds that in the satellite, accretion will deposit clusters in regions of mean density similar to that in the original environment of the accreted galaxy. The clusters, then, will remain roughly tidally truncated. Their new orbits depend on the orbit of the dissolving satellite, but otherwise evolution should be similar and the accreted population may appear coeval regardless of the time of accretion.

The high specific frequency of globular clusters in M87 appears to indicate the exceptional conditions governing the formation and evolution of cD galaxies relative to other ellipticals. The observation that specific frequency increases with galaxy luminosity suggests that galaxy formation was not an intrinsically hierarchical and homologous process (e.g. Santiago & Djorgovski 1993).

However, the current results indicate that density differences between galaxies will lead to differences in the evolution of intrinsic cluster populations. Since M87 lies approximately on the fundamental plane for elliptical galaxies, we can investigate differences in environment-driven cluster evolution by scaling our results to other ellipticals. We assume that the initial profile of the cluster population derived above, when scaled homologously, describes the initial population in any elliptical. The dynamical time scale for a tidally truncated

cluster with constant mass and spatial profile is then determined by the mean density of the galaxy: $\tau \sim M^{-1/2}R^{3/2}$. This yields $\tau \sim M^{\beta}$, where $\beta = 0.4$ for the fundamental plane scaling given in Faber et al. (1987), $\beta = 0.26$ for the Djorgovski & Davis (1987) results, and $\beta = 0.6$ for a more recent set of parameters from Faber (1995; see also Pahre et al. 1995). This relation implies that clusters evolve and are depleted more rapidly in smaller, low luminosity ellipticals than in massive, high luminosity ellipticals.

To demonstrate the importance of this effect, we combine the approximate exponential decay rate of the cluster population found in §3.4.4 with this scaling relation. This gives an expression for the number of clusters remaining in an initially coeval population belonging to a galaxy of luminosity L at time T:

$$\begin{aligned} N_{cl}(L,T) &= N_0(L)e^{-T/\tau_0(M_{M87}/M)^{\beta}} \\ &= N_0 e^{-T/\tau_0(L_{M87}/L)^{1.24\beta}}, \end{aligned} \tag{3.1}$$

where $\tau_0 \approx 40\,\mathrm{Gyr}$ for M87, $N_0(L)$ is the initial distribution of cluster population sizes as a function of galaxy luminosity and $M/L \sim L^{1.24}$ throughout.

Using a power-law distribution $N_0(L) = N_*(L/L_{M87})^{\gamma}$, we compare the model curve $N_{cl}(L,T)$ to an observed sample of cluster populations in galaxies (Harris 1996). The resulting models show qualitative agreement with the data (Figure 3.8), falling off at low luminosity more rapidly with increasing β due to the more rapid rate of evolution. From this we conclude that the observed discrepancies in specific frequency which correlate with galaxy luminosity were smaller in the past. This is reflected in the smaller exponent γ in $N_{cl} \propto L^{\gamma}$ predicted initially compared to the present-day estimate.

To conclude, we suggest that cluster evolution may account at least in part for the specific frequency problem. Because clusters evolve more rapidly in dense

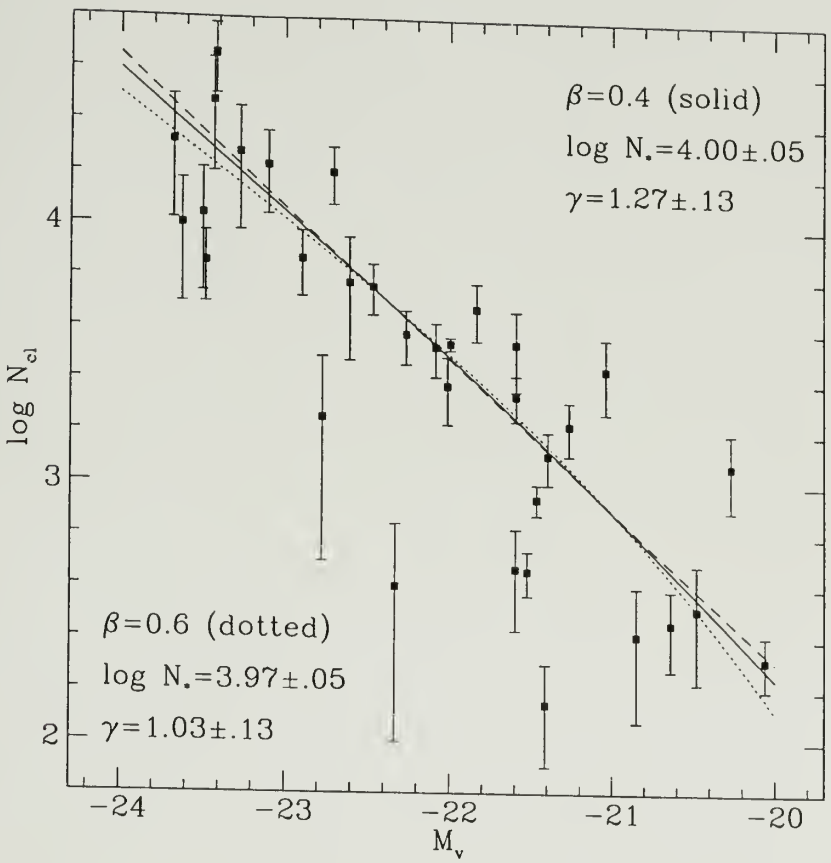

Figure 3.8. Evolved cluster population size vs. parent galaxy luminosity. Evolved population size as a function of galaxy luminosity compared to data from Harris (1996) for fundamental plane parameter $\beta = 0.4$ (solid) and $\beta = 0.65$ (dotted) . The present-day, unevolved fit (dashed) has $\log N_* = 3.89 \pm .05, \gamma = 1.46 \pm .13$. For $\beta = 0.65$, the initial value of γ is consistent with specific frequency which is independent of luminosity

environments and because ellipticals are typically denser at low luminosity that at high luminosity, cluster populations diminish more rapidly in low luminosity galaxies. Specific frequencies will therefore correlate more strongly with luminosity at later times.

3.6 Summary

We have investigated the evolution of the M87 globular cluster system. The results of this study have enabled us to examine the broader question of population evolution in fundamental plane elliptical galaxies. Our main conclusions follow:

1. The loss of globular clusters through relaxation and tidally-induced evaporation accounts for the large core and shallow profile in cluster number distribution compared to the light distribution in M87.

2. Evolution produces a radial dependence in the present-day mass spectrum of clusters such that higher mass clusters predominate in the inner regions. The models also indicate an initial radial dependence in the mass spectrum.

3. Likelihood ratio tests reject an initial power law in favor of an initial Gaussian but do not rule out the possibility of an initial core in the profile.

4. The best-fit model for M87 has an initial population of 7.25×10^3 clusters with projected radius $R < 50\,\mathrm{kpc}$, about 60% more than is currently observed. Roughly 14% of the initial population are now objects of slightly less than $10^5 M_\odot$; dynamical evolution can strongly modify the specific frequency of globular clusters.

5. Scaling the calculations to fundamental plane elliptical galaxies indicates that cluster evolution in the differing environments qualitatively accounts for the trend in observed population number versus galaxy luminosity. Smaller

galaxies tend to have high densities and thus more rapid evolutionary time scales, so their cluster populations tend to diminish more rapidly.

Some of these inferences, especially (iii), may be biased by the lack of detailed data in the inner galaxy. Point source data for $r < 1'$ will lead to stronger constraints on the size of the initial core and a deeper survey will pick up low luminosity objects and further constrain the luminosity function.

Chapter 4

Globular Cluster Evolution in the Milky Way

We estimate that a sample of 111 Milky Way globulars with velocity information descends from a progenitor population of 250 clusters. Approximately 200 of these clusters were in a spherical component and 50 in a disk component. The initial spherical population possessed a radially anisotropic orbit distribution with approximately 40% of its kinetic energy in radial motion. These inferred initial characteristics are in agreement with the spatial and kinematic distribution of halo stars derived by Sommer-Larsen & Zhen (1990). Evolution has produced a nearly isotropic distribution today. The disk component possessed a nearly isotropic initial distribution which has become more tangentially biased with time. The inferred initial characteristics do not match the kinematics of the rapidly rotating thin or thick disk stellar populations, but may correspond to a highly flattened but kinematically random halo component.

Examination of internal properties in evolving clusters shows that cluster halos are strongly modified by tidal heating and differ from equilibrium King model profiles. However, evolving line-of-sight mass spectral indices do not show marked differences as a function of orbit except due to differences in evolutionary time scales expected in tidally-limited clusters on different orbits.

4.1 Introduction

Age estimates for globular clusters indicate that they formed early in the history of the Milky Way and represent 'fossil relics' of the proto-Galaxy (e.g. Larson 1990). To reveal traces of Galactic evolutionary history, researchers have

carefully examined a range of properties of the present-day cluster system, paying particular attention to the cluster kinematic distribution (e.g. Zinn 1993), mass distribution (e.g. Harris & Pudritz 1994), metallicity distribution (e.g. Zinn 1985) and age distribution (e.g. Chaboyer, Demarque & Sarajedini 1996). These investigations have provided evidence for both accreted and native components in the cluster system (e.g. Searle & Zinn 1978) and correlations between kinematics and metallicity which may trace the collapse of the Galaxy (e.g. Zinn 1985; Armandroff 1989; Zinn 1993).

At the same time, theoretical interest in globular cluster evolution was initiated by the discovery that two-body relaxation would drive evolution on a time scale that is much less than the age of a typical cluster (e.g. Ambartsumian 1938; Spitzer 1940; Chandrasekhar 1942). Subsequent research provided an understanding of the gravothermal instability (Lynden-Bell & Wood 1968) and the phenomenon of core collapse (e.g. Cohn 1980). One of the basic conclusions of this work is that relaxation inevitably leads to cluster evaporation. Additional refinements to the picture of relaxation-driven evolution have been motivated by the need to account for a source of energy which halts core collapse (e.g. Henon 1961; Lee & Ostriker 1987) and the need to include tidal influences which arise on a cluster's orbit in a parent galaxy (e.g. Ostriker, Spitzer & Chevalier 1972; Chernoff, Kochanek & Shapiro 1986; Weinberg 1994).

Recent work on tidal influences has shown that evaporation is accelerated by the interaction of a cluster with the tidal field produced by the halo and disk of the Galaxy (e.g. Murali & Weinberg 1996, hereafter Paper I; Gnedin & Ostriker 1996). In particular, the results indicate that cluster depletion strongly depends on mass and orbit in the Galaxy and suggest that an understanding of cluster formation in the proto-Galaxy and the nature of clusters as 'fossil relics' requires a comprehensive description of cluster evolution since the time of formation. In a

related study providing further motivation, Murali & Weinberg (1996; hereafter Paper II), have demonstrated the importance of evolution in shaping the M87 globular cluster population and as a partial cause for the specific frequency conundrum in fundamental plane ellipticals.

In the present work, we investigate the degree to which evolution has shaped the Milky Way cluster population. We concentrate on inferring the size of the initial population and its initial kinematic distribution. The inferences are derived from both spherical and 2-component disk+sphere models of the cluster distribution. While several analyses have shown the cluster system to be approximately spherically distributed (e.g. Chernoff & Djorgovski 1989; Thomas 1989), other investigations show the presence of a flattened, rapidly rotating high-metallicity component with a spherically distributed low-metallicity component associated with the Galactic halo (e.g. Zinn 1985; Armandroff 1989). Further subdivisions may also exist (Zinn 1993; Zinn 1996). The choice of models reflects the gross characteristics of the cluster system and allows us to compare the candidate distributions. As the results show, neither model is completely successful in describing the cluster population because of the effects of evolution.

The study is based on the Fokker-Planck description of cluster evolution discussed in Paper I and the parametric statistical framework employed in Paper II. We first provide a detailed examination of cluster evolution in a Milky Way model which includes disk and halo. The calculations demonstrate the enhancement in the rate of evolution caused by the disk and examine evolutionary varations with orbit. Next we study the behavior of internal density profiles and mass spectra in evolving clusters. Finally, we investigate the present-day and initial characteristics of the cluster population. The analysis employs the data set compiled by Gnedin & Ostriker (1996) and a likelihood technique that also enables us to exploit the three-space velocities derived by Cudworth (1993). The results

point to differences in the initial and observed cluster populations, indicating the role of evolution in shaping the present-day cluster system.

The plan of the paper is as follows. In §4.2, we summarize the approach and scenario used throughout the investigation. §4.3 describes the physical behavior as a function of orbit, examines the internal properties of evolving clusters and concludes with an investigation of the population. Finally, §4.4 discusses the implications of the results. Appendices provide derivations of the models and a discussion of the statistical procedure.

4.2 Procedure for Investigation

4.2.1 Cluster evolution

Following formation and early stellar evolution, cluster evolution is driven by relaxation, the tidal field and binary heating of the core. As described in Papers I & II, the competition between relaxation and the tidal field of a galaxian spheroid is particularly important in determining a cluster's evolutionary time scale and survival history. The dominant effects of the spheroid on tidally-limited clusters were found to be heating on low-eccentricity orbits and tidal truncation on high-eccentricity orbits.

In the Milky Way, the disk also contributes significantly to cluster evolution. For high inclination orbits, a number of investigations have shown that the compressional shock imparted to a cluster during its passage through the disk will generally enhance the evaporation rate (e.g. Spitzer & Chevalier 1972; Chernoff, Kochanek & Shapiro 1986; Weinberg 1994; Gnedin & Ostriker 1996). For orbits confined to the disk, oscillations of the cluster about the midplane transfer energy through resonant stellar orbits. Below we further investigate the effect of the disk on cluster evolution on both low- and high-inclination orbits (§4.3.1). Appendix C.1 gives the derivation of the heating rate for disk oscillations.

4.2.2 Orbits

For eccentric, high-inclination orbits, the orbital phase of disk passage varies due to the precession of the argument of perihelion with respect to the plane of the Galaxy because orbits are not closed in the logarithmic potential. To remove dependence on unknown orbital phase, we define an effective energy input due to disk shocking to be that which occurs at the average orbital radius of the cluster which undergoes two passages per orbital period. For eccentric low-inclination orbits, we also fix the effective heating rate to be that which occurs at the average orbital radius and assume that the vertical motion is prefectly separable from the radial and tangential motion in all orbits. This allows us to define approximate three-integral distribution functions in terms of algebraic constants of the motion (c.f. §4.2.4).

Orbits in the spheroid are defined using the quantity $\kappa = J/J_{max}(E)$, which denotes the angular momentum relative to maximum for an orbit of energy E. The inclination angle is denoted i and is defined with respect to the disk, so that $i = 0^{\circ}$ defines an orbit exactly in the plane of the disk. Oscillations through the disk are noted in terms of their oscillation height in multiples of the disk scale height, z_0.

4.2.3 Model populations

Our fiducial population consists of clusters which formed in a single episode approximately 11 Gyrago. Initial clusters are assigned $W_0 = 5$ King model profiles. Investigation of concentration dependence in §4.3.1 shows that evaporation times vary little with W_0. We assume that each cluster has a Salpeter IMF ($\beta = 2.35$) with lower mass limit, $m_l = 0.1\,\mathrm{M}_{\odot}$. For this choice, stellar evolution would dominate for the first Gyr, corresponding to the main sequence lifetime of a $2\,\mathrm{M}_{\odot}$ A-star. Following the phase of strong stellar evolution, relaxation, external heating

and core collapse heating would begin to drive cluster evolution. We take this epoch to define the zero-age population considered in this paper.

Clusters on orbits highly inclined from the disk are tidally limited by the Galactic spheroid. While initial cluster densities may differ from the mean density required by perigalactic tidal limitation, subsequent evolution during the first Gyr leads rapidly to tidal truncation or disruption. Clusters on orbits confined to the disk may posess limiting radii smaller than that implied by tidal limitation in the spheroid (e.g. note the discrepancy between the observed and predicted tidal radius of M71; c.f. Drukier, Richer & Fahlman 1993). This implies that, for given concentration, their density is higher than that required for tidal limitation. However, §4.3.1 shows that evaporation times vary little with density for the low-mass clusters which dominate the population. Therefore, in studying population evolution, we assume that low-inclination clusters are also tidally limited. The limiting or *tidal* radius R_T is uniquely determined by the cluster mass and orbit (see Paper I for further details).

We employ the commonly used terminology of 'disk' and 'halo' cluster. A 'disk' cluster is most often 'metal-rich' with disk kinematics while a 'halo' cluster is most often 'metal-poor' with halo kinematics but which may have high or low orbital inclination relative to the disk. A 'classic' halo orbit, however, is one of high inclination from the disk.

4.2.4 Distribution functions

We use parametric models to define distributions of cluster orbits and masses in both disk and spheroid populations. Mass distributions, $\nu(M)$, are defined using a power-law (e.g. Harris & Pudritz 1994), a two-component power-law and a Gaussian magnitude distribution (e.g. McLaughlin, Harris & Hanes 1994). The

2-component power-law mass spectrum has continuity imposed at the mass, M_{cut}, where the spectral index changes.

Distributions of cluster orbits are defined using models which trace the adopted Galactic potential (c.f. §4.2.9). Disk component distribution functions, $f(E_d, J_z^2, E_z)$, are defined using the Mestel disk with no net rotation (e.g. Binney & Tremaine 1987) combined with an isothermal vertical distribution. This provides a family of constant anisotropy, power-law surface density profiles with index $-(\eta_d - 2q_d)$ of infinite range, where η_d defines the velocity dispersion of the distribution and q_d determines the degree of anisotropy. The range is infinite because $0 \leq \eta_d < \infty$ and $-\frac{1}{2} \leq q_d < \infty$ (see Appendix C.3 for derivation and further discussion).

Spheroidal component distribution functions, $f(E, J^2)$, are defined by adapting the Mestel DF to the spherical case, (which we refer to as the 'Mestel Sphere'; see Appendix C.4) and also using the Eddington model (e.g. Aguilar, Hut & Ostriker 1988; see Appendix C.5 for derivation and further discussion). The Mestel sphere DF gives rise to a family of constant anisotropy power-law space density profiles with index $-(\eta - 2q)$ of infinite range. The Eddington sphere DF produces a family of variable anisotropy, power-law space density profiles with cores having index $-\eta$ and core radius R_a, where R_a is the radius at which the radial anisotropy of the distribution becomes significant.

Table 4.1 gives the functional form for each model. Complete orbit and mass distributions are taken to be the joint distributions $\nu(M) \times f$, and we assume that disk and halo components can have a different mass spectra. In the 2-component model, F denotes the fraction of the population belonging to the spherical component. Because disk cluster evolution varies little with oscillation height (see §4.3.1), we determine the parameter η_z for the observed distribution and keep it fixed in the subsequent fit to determine the initial conditions in order to minimize

Table 4.1. Functional forms of models

Mass Models

Name	$\nu(M) \propto$	Parameters
power-law	$M^{-\alpha}$	α
2-component power-law	$M^{-\alpha_1}(M \leq M_{cut})$ $M^{-\alpha_2}(M > M_{cut})$	α_1, α_2, M_{cut}
gaussian mag.	$e^{-(V-V_0)^2/2\sigma_V^2} \cdot dV/dM$	V_0, σ_V

Distribution Functions

Name	$f(E, J^2, E_z) \propto$	Parameters
Mestel disk	$e^{-E_d/\sigma_d^2} J_z^{2q_d} e^{-E_z/\sigma_z^2}$	η_d, q_d, η_z
Mestel sphere	$e^{-E/\sigma^2} J^{2q}$	η, q
Eddington sphere	$e^{-E/\sigma^2} e^{-J^2/2r_a^2\sigma^2}$	η, r_a

the number of parameters since the cluster population is not large. For the disk distribution, we impose a priori cutoffs in radius at $R_d = 15\,\mathrm{kpc}$ (Wainscoat et al 1992) and height at $Z = 7.5\,\mathrm{kpc}$.

Two types of fit are used to characterize the data. Fits without the evolutionary calculations (c.f. §4.2.6) are used to derive the observed or *present-day* properties of the cluster sample. Fits including the evolutionary calculations are used to derive the most likely initial conditions which produce today's distribution. We first consider the present-day characteristics of the cluster system to serve as a guide for applying the models in the evolutionary case. The listed uncertainties are given as $1 - \sigma$ error bars under the assumption of normally distributed errors.

4.2.5 Parameterization of disk strength

In order to parameterize the strength of the spheroid relative to the cluster in Paper I, we introduced the quantity $M(x_p)$ which denotes the fraction of the cluster mass contained within the pericentric inner Lagrange point. In the following, because of the presence of the disk, it is also convenient to define the quantity $\chi = x_p/r_t$, which denotes the ratio of the pericentric inner Lagrange point to the limiting radius of the cluster (which we shall still refer to as the *tidal radius*); and the quantity $\rho_{0,d}(R)/\bar{\rho}_c$, which denotes the ratio of the disk central density at a given radius R to the cluster mean density. This latter parameter defines the amplitude of the disk relative to the cluster in the same way as $M(x_p)$ is used to define the relative amplitude of the spheroid. Using χ, we can write the ratio of the cluster mean density, $\bar{\rho}_c$, to the mean density required for tidal limitation in the spheroid, $\bar{\rho}_t$, as $\bar{\rho}_c/\bar{\rho}_t = \chi^3$.

4.2.6 Calculations

We follow the evolution of individual clusters using the one-dimensional Fokker-Planck approximation (e.g. Cohn 1979). The calculations include relaxation, external heating due to the time-varying tidal field of the disk and spheroid (as implemented in Paper I), and a phenomenological binary heating term (e.g. Lee et al. 1991).

Properties of the evolved cluster population are estimated from a grid of Fokker-Planck calculations performed over a range of cluster orbits For the disk clusters, we use a $4 \times 4 \times 5$ grid in apogalactic radius, mass and κ to sample the phase space. Apogalactica are taken in the range $2 \leq R_a \leq 8\,\mathrm{kpc}$, masses in the range $10^5\,\mathrm{M}_\odot \leq M \leq 5 \times 10^6\,\mathrm{M}_\odot$ and orbits in the range $0.3 \leq \kappa \leq 1.0$. For the halo clusters, we use a $5 \times 4 \times 5$ grid with $5 \leq R_a \leq 15\,\mathrm{kpc}$ and the same range of mass and κ. All clusters with $R_a = 0.8\,\mathrm{kpc}$ are assumed depleted and all clusters

with energies equal to a circular orbit with $R_a = 20\,\mathrm{kpc}$ are assumed to be unevolved. For $R_a = 0.8\,\mathrm{kpc}$, clusters on circular orbits either evaporate at low mass or decay into the nucleus by dynamical friction (e.g. Aguilar, Hut & Ostriker 1988) and clusters on eccentric orbits evaporate. For $R_a = 20\,\mathrm{kpc}$, the evaporation timescale on a circular orbit is 70 Gyr for $10^5\,\mathrm{M}_\odot$ and is roughly the same for other orbits of equal energy.

In §4.3.1, we find that low inclination halo clusters evolve more rapidly than high inclination clusters, although the differences are not extreme. However, in order to reduce computational expense, we neglect the phase space occupied by low-inclination orbits in the spherical component. This assumption enable us to avoid the roughly factor-of-four increase in halo phase space grid size required to sample the cylindrical geometry. As a result, the initially spherical distribution remains spherical and we underestimate the amount of evolution about the midplane of the disk, the consequences of which are discussed further below.

4.2.7 Estimation procedure

A maximum likelihood procedure is used to estimate the parameters in Table 4.1 from the observed cluster data. Generally the data for any given cluster is of varying completeness with respect to the seven components required in our models (the mass + 6 phase space components), so, to incorporate all available data, we use a likelihood technique for incomplete data sets (e.g. Little & Rubin 1987; Stuart & Ord 1991). By integrating the distribution function over all dimensions of unknown information for a particular observed cluster, we derive the marginal probability of the given observation. Typically, only the heliocentric radial velocity is known, so we integrate over the tangential velocities relative to our vantage point to derive the marginal probability of observing a cluster at a given position with a given heliocentric radial velocity. The likelihood may then be constructed

in the usual manner from the joint probabilities of the observations given the model. Appendix C.6 discusses the technique in more detail.

4.2.8 Data

We use the data compiled in Gnedin & Ostriker (1996) which consists of 119 objects. We examine the distribution of clusters within 65 kpc having masses in the range $2.0 \times 10^4\,\mathrm{M}_\odot \leq M \leq 2.75 \times 10^6\,\mathrm{M}_\odot$, using a mass-to-light ratio of 3. This removes 6 clusters from the original sample, leaving a total of 113 clusters. In most cases clusters with $M \leq 10^5\,\mathrm{M}_\odot$ initially had masses above $10^5\,\mathrm{M}_\odot$. In a few cases, extrapolation beyond the initially defined grid is required.

Using the likelihood procedure outlined above, we can also include in the data set the three-space velocities which now exist for about 20 clusters (Cudworth 1993). This is referred to as the *augmented data set.* Below we compare fits to both data sets to indicate the amount of additional information provided by the full 3-space velocities.

4.2.9 Galactic model

We represent the spherical component of the Galaxy as a singular isothermal sphere with $V_0 = 220\,\mathrm{km\,s^{-1}}$ and the disk component as an exponential disk with radial scale length $R_0 = 3.5\,\mathrm{kpc}$ normalized to the disk central density in the solar neighborhood, $\rho_0 = 0.15\,\mathrm{M}_\odot/\,\mathrm{pc}^3$ (Binney & Tremaine 1987). The vertical profile is taken to be Gaussian with a scale height of $z_0 = 320\,\mathrm{pc}$. The Gaussian was adopted instead of an exponential initially due to concern about the analyticity of the perturbation and its effect on adiabatic invariance. However, comparisons between the two profiles show no strong differences in heating rate (e.g. Weinberg 1994). The solar radius is taken to be $R_0 = 8.5\,\mathrm{kpc}$. All measured radial velocities are converted to velocities in the Galactic rest frame using an LSR velocity of

$220\,\mathrm{km\,s^{-1}}$ and a solar motion of $(\Pi, \Theta, Z) = (-9, 12, 7)\,\mathrm{km\,s^{-1}}$ (Mihalas & Binney 1981).

4.3 Results

4.3.1 Physical Behavior

4.3.1.1 The importance of disk heating

In Paper I, a calculation of fixed mass, $M(x_p)$ and κ could be scaled to an orbit of any energy due to the scale-free nature of the tidal field. This allowed us to compare the orbital dependence of cluster evolution in several ways using the same calculations (c.f. Paper I, §3.1). Here the disk destroys this scaling freedom because the quantity $\rho_{0,d}(R_d)/\bar{\rho}_c$ varies with the radius R_d of disk crossing. In order to compare cluster evolution on different orbits, in Tables 4.2 and 4.3, we show the mass remaining after 10 Gyr in tidally-limited clusters on orbits of equal apocenter over a range of mass and eccentricity both with and without the disk.

For equal apocenter and fixed mass, the densities of tidally-limited clusters increase with orbital eccentricity because the perigalactic angular frequency increases, implying a smaller tidal limit. Clusters on eccentric orbits therefore undergo the most rapid relaxation and can be expected to have high evaporation rates. However, tidal heating enhances mass loss rates on low-eccentricity orbits. As a result, for evolution in the spheroid alone, the remaining masses of $10^5\,\mathrm{M}_\odot$ clusters decrease monotonically with eccentricity because their evolution is dominated by relaxation. The remaining masses of $10^6\,\mathrm{M}_\odot$ clusters peak at intermediate eccentricity because the intrinsic relaxation rates are small enough that tidal heating noticeably increases mass loss at low eccentricity.

The large amplitude of the disk relative to the spheroid greatly enhances tidal heating on low and intermediate eccentricity orbits in the disk+sphere calculations. High-mass low-eccentricity disk clusters lose equilibrium and suffer

Table 4.2. Disk clusters: fraction of remaining mass after 10 Gyr

$10^5\,M_\odot$

$\kappa =$	1.0	0.9	0.6	0.3	
4 kpc	0.0	0.0	0.0	0.0	disk+sphere
	0.42	0.35	0.0	0.0	sphere
8 kpc	0.0	0.0	0.05	0.0	disk+sphere
	0.77	0.76	0.40	0.0	sphere

$10^6\,M_\odot$

$\kappa =$	1.0	0.9	0.6	0.3	
4 kpc	0.0	0.54	0.74	0.60	disk+sphere
	0.77	0.84	0.89	0.60	sphere
8 kpc	0.0	0.25	0.75	0.86	disk+sphere
	0.85	0.91	0.95	0.86	sphere

for $5z_0$ oscillation height and $W_0 = 5$

disruption. The low-mass counterparts do not disrupt but are rapidly driven to evaporation by strong tidal stripping. For increasing eccentricity the tidal effect diminishes due to the increasing density of cluster relative to disk at the crossing point of the orbit, and is negligible at $\kappa = 0.3$.

Since the strength of the disk relative to the spheroid varies with radius, the importance of disk heating varies as a function of the radius of disk crossing. The relative strength of disk heating is highest at about 8 kpc. As a result, the $10^6\,M_\odot, \kappa = 0.9$ disk cluster at 8 kpc loses more mass than does its counterpart at 4 kpc (c.f. Table 4.2).

Halo clusters exhibit the same overall tendencies as disk clusters, but with lower heating rates for the given inclination. Heating rates are lower because the input power is concentrated at higher frequencies than the input power from disk oscillations. For example, at 90° inclination, the $1z_0$ passage time scale is on the order of 1 Myr while the corresponding period of an oscillation with height $> 1z_0$ is

Table 4.3. Halo clusters: fraction of remaining mass after 10 Gyr

$10^5\,M_\odot$

$\kappa =$	1.0	0.9	0.6	0.3	
5 kpc	0.14	0.10	0.0	0.0	disk+sphere
	0.58	0.55	0.0	0.0	sphere
10 kpc	0.74	0.73	0.42	0.0	disk+sphere
	0.82	0.82	0.59	0.0	sphere

$10^6\,M_\odot$

$\kappa =$	1.0	0.9	0.6	0.3	
5 kpc	0.49	0.56	0.82	0.72	disk+sphere
	0.80	0.86	0.91	0.73	sphere
10 kpc	0.80	0.82	0.90	0.90	disk+sphere
	0.87	0.93	0.96	0.90	sphere

for $i = 90°$ and $W_0 = 5$

> 10 Myr for $R_d > 2$ kpc. At high frequency, the response of a stellar orbit to a perturbation of fixed amplitude decreases due to the increased binding energy.

4.3.1.2 Inclination dependence

The importance of frequency matching is also evident when comparing halo clusters on orbits of different inclination with respect to the disk. Table 4.4, which compares cluster evolution on circular orbits, shows that mass loss increases as orbits become less inclined due to the improved frequency match between perturbation and cluster. At 5 kpc, the best match occurs for $i = 30°$, while at 10 kpc, the best match occurs at $i = 15°$. Radial differences arise because the disk passage time is fixed at $t_{pass} \sim 1 z_0/v_c \sin i$, while the cluster dynamical time scale varies as $\bar{\rho}_c^{-1/2}$ which is fixed by the mean density of the spheroid through tidal limitation. The drop in cluster mean density at 10 kpc leads to more efficient heating at lower passage speed. The tendency to stronger evolution at low inclination and for clusters confined to the disk implies that an initially spherical

Table 4.4. Halo clusters: fraction of remaining mass after 10 Gyr as a function of orbital inclination

$10^5\,M_\odot$

$i =$	15	30	60	90
5 kpc	0.02	0.0	0.09	0.14
10 kpc	0.49	0.59	0.71	0.73

$10^6\,M_\odot$

$i =$	15	30	60	90
5 kpc	0.50	0.41	0.44	0.49
10 kpc	0.58	0.69	0.80	0.80

$\kappa = 1.0$ and $W_0 = 5$

halo distribution will develop a vertically-dependent density profile with minimum density about the midplane of the disk.

4.3.1.3 Density dependence

The rapid disruption of tidally-limited low-eccentricity disk clusters suggests that they have higher initial densities to survive for long periods after formation. Figure 4.1 shows survival, disruption and evaporation patterns in clusters on circular orbits with a range of initial densities, parameterized by the ratio of disk central density to cluster mean density, $\rho_{0,d}(R_d)/\bar{\rho}_c$. The heat input from the spheroid is negligible beyond 1 kpc for disk clusters and has therefore been ignored to provide scaling freedom. Surviving clusters are bounded by disruption at low density and evaporation at high density. $10^5\,M_\odot$ clusters can only survive beyond 7 kpc. For higher mass, the evaporation boundary moves to higher density because of the longer relaxation time scale. However, the disruption boundary remains fairly constant at density higher than the tidal limit.

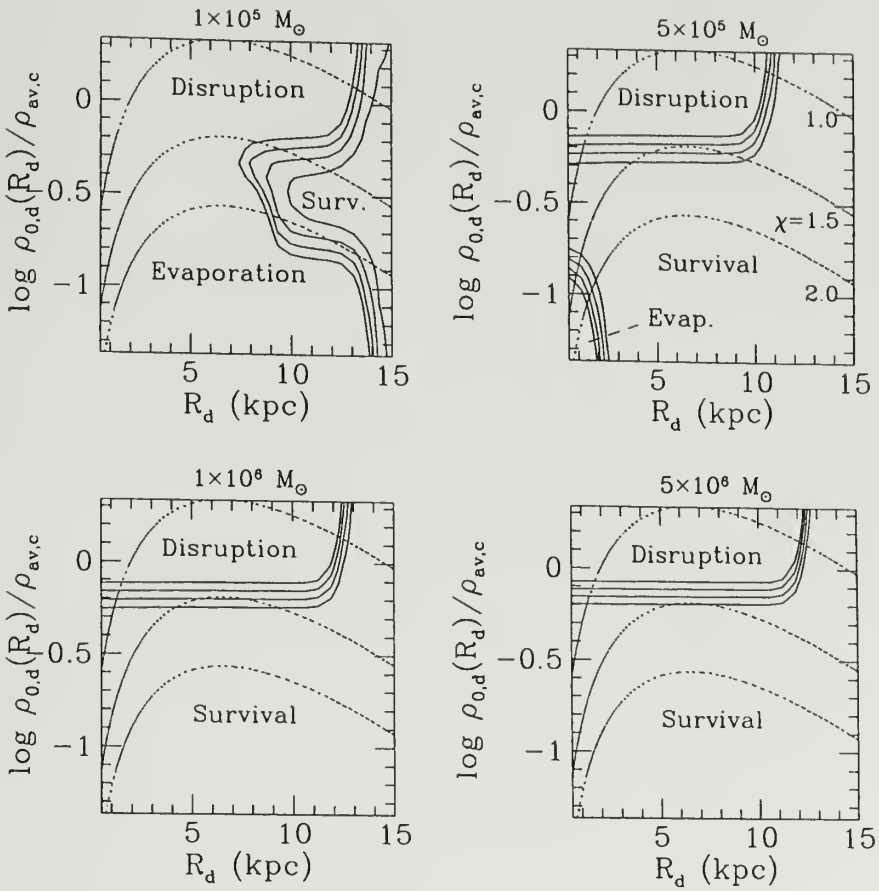

Figure 4.1. Density dependence of evaporation time. The remaining mass of disk clusters on circular orbits executing $5z_0$ oscillations as a function of the ratio of disk central density to cluster central density (for a $W_0 = 5$ profile). Solid contours show remaining masses in the range $3.5 \leq logM_c \leq 4.5$. Dotted contours show values of $\chi = x_p/r_t$ as labeled in the top right panel. Initial masses are given at the top of each panel. Lower density clusters tend to disrupt due to tidal heating while higher density clusters tend to evaporate due to rapid rates of relaxation. The density required for tidal limitation in the spheroid is too low to allow survival against disk heating.

Table 4.5. Disk clusters: fraction of remaining mass after 10 Gyr as a function of disk oscillation height

		oscillation height			
		$1z_0$	$2z_0$	$5z_0$	$10z_0$
$10^5\,M_\odot$	4 kpc	0.0	0.0	0.0	0.0
	8 kpc	0.45	0.36	0.38	0.43
$10^6\,M_\odot$	4 kpc	0.80	0.76	0.67	0.69
	8 kpc	0.82	0.81	0.77	0.78

$\kappa = 1.0$ and $W_0 = 5$

4.3.1.4 Dependence on oscillation height

Table 4.5 shows the dependence of disk cluster evolution on oscillation height for clusters on circular orbits with $\log \rho_{0,d}(R_d)/\bar{\rho}_c = -0.37$– well within the the tidal limit set by the spheroid but still strongly influenced by disk heating. Evolution is weakly dependent on the oscillation amplitude, with the maximum effect occurring between $2z_0$ and $5z_0$. We exploit this property below to remove the vertical dimension from the phase space grid required to construct the distribution of evolved disk clusters.

4.3.1.5 Concentration dependence

The preceding discussion is based on clusters of a single concentration. To examine the concentration dependence, we consider the evolution of disk clusters of varying concentration for different values of $\rho_{0,d}(R_d)/\bar{\rho}_c$ and a range of mass. Figure 4.2 indicates evaporation dominates at high concentration and high density while disruption dominates at low concentration and low density. Clusters show similar trends for increasing eccentricity, with evaporation becoming more important due to the increasing cluster densities of tidall-limited at fixed Galactocentric radius.

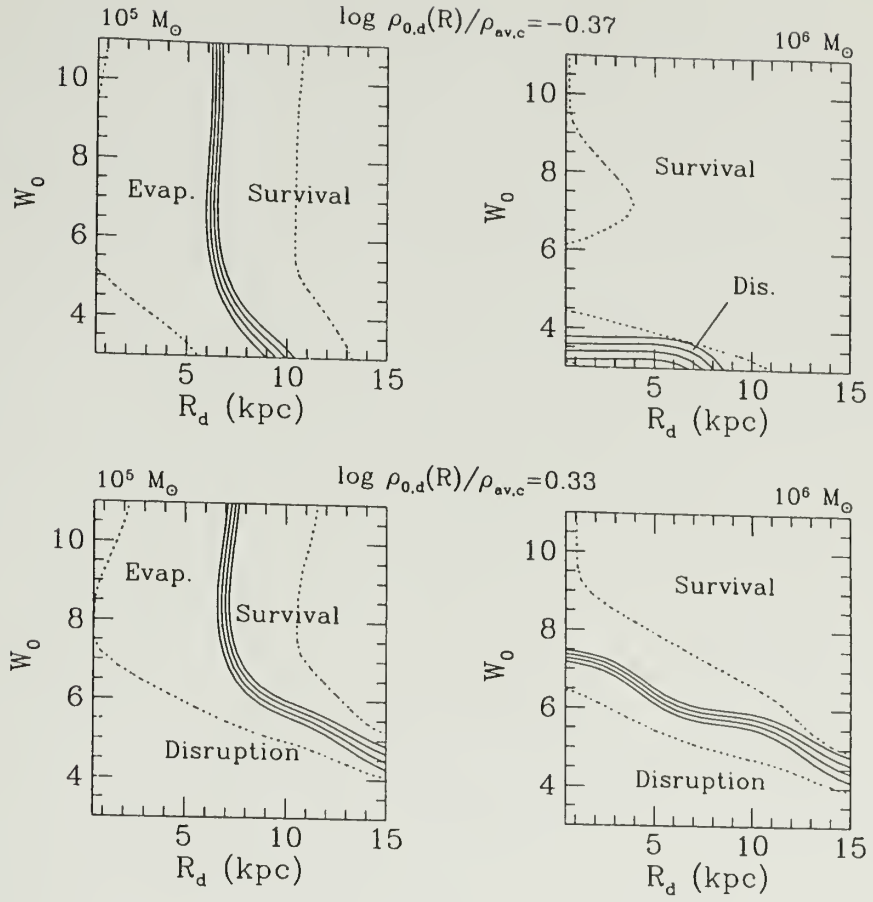

Figure 4.2. Concentration dependence of evaporation time. Remaining mass after 10 Gyr as a function of initial concentration and radius in the disk for clusters on circular orbits with indicated masses and mean densities. Solid contours show remaining masses in the range $3.5 \leq \log M_c \leq 4.5$. Dotted contours show the 5 Gyr and 15 Gyr evaporation/disruption isochrones on either side of the 10 Gyr survival boundary. $10^5\,M_\odot$ clusters evaporate for $R_d \leq 6$ kpc at high mean density (upper left) and evaporate or disrupt for $R_d \leq 7$ kpc at low mean density (lower left). $10^6\,M_\odot$ clusters disrupt for $R_d \leq 7$ kpc and very low concentration at high mean density (upper right) and disrupt for over a large range in radius and concentration for low mean density (lower right).

4.3.2 Internal properties

To illustrate some basic trends in the evolution of internal cluster properties, we examine traits of the the $10^6\,M_\odot$ disk clusters with apogalactica at 8 kpc. Figure 4.3 compares evolution in projected profiles for cases ranging from tidal disruption to relaxation-dominated core contraction. The tidally dominated $\kappa = 1.0$ and $\kappa = 0.9$ clusters shows marked departure from the initial King model profiles, developing a steeper fall-off which is roughly a power-law. The limiting radii remain near the expected tidal boundary which moves inward due to the mass loss.

The profiles also show mild concavity in the fall-off, a feature which appears similar to the observed profiles given by Grillmair et al (1995,1996), who interpreted their observations as *tidal tails*. However, the feature evident here is not an unbound tidal tail but, rather, a bound halo region which has been partially cleared through resonance. For $\kappa = 0.7$, heating is strong enough to produce deviation from the initial King profile, although the central evolution is relatively unaffected. For $\kappa = 0.5$, heating is so weak that the outer profile remains fixed while the central regions undergo gravothermal contraction.

The evolution of the line-of-sight mass spectral index is shown in Figure 4.4. Mass segregation occurs in every case, regardless of the strength of tidal heating. As the $\kappa = 1.0$ cluster disrupts, however, the low mass component completely evaporates. The other cases show flattening of the spectrum in the core and steepening in the halo with differences that increase with eccentricity. This trend results from the more rapid evolutionary time scale at high eccentricity for orbits with equal apocenter. Aside from differences in time scale, the evolution of the mass spectral index does not depend significantly on orbit. One potentially important feature is the constancy of the spectral index near the initial half-mass radius of the cluster. However, the half-mass radius is relatively constant only in

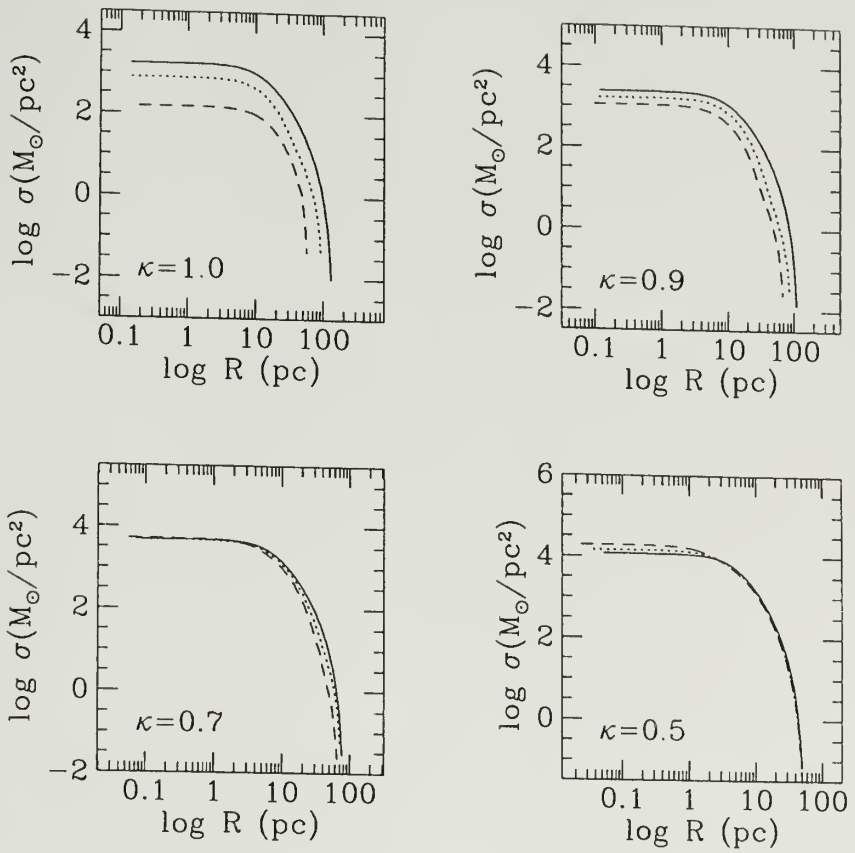

Figure 4.3. Orbital dependence of profile evolution. The evolution in projected mass profile for four 10^6 $M_\odot$ clusters on indicated orbits with apogalactica at 8 kpc. Solid lines show initial profiles; dotted lines show profiles after 5 Gyr; dashed lines show profiles after 10 Gyr except for $\kappa = 1.0$ whose profile is shown at 7.5 Gyr, just prior to disruption. In the strong tidal cases ($\kappa = 1.0, \kappa = 0.9$), halos are truncated and profiles develop a steeper fall-off than the initial profile. In the $\kappa = 0.7$ case, no expansion occurs due to greater balance between heating and relaxation, but the outer profile evolves due to tidal heating. The $\kappa = 0.5$ cluster undergoes negligible tidal heating, evidenced by the static halo profile, while relaxation leads to increasing central densities.

the most eccentric cases; it evolves considerably when tidal effects are strong. Therefore, it is observationally difficult to estimate the initial mass spectral index to better than ~ 0.5 dex.

4.3.3 The cluster population

We now investigate the properties of the cluster population as a whole. Our main goal is to establish characteristics of the initial cluster distribution. Before pursuing this topic, we examine the present-day characteristics of the cluster population to provide reference for understanding evolutionary inferences as well as to compare some of the frequently-used models for the cluster population.

4.3.3.1 Present-day characteristics

Figure 4.5 shows the inferred model parameters for the Mestel sphere both with and without the tangential velocity. The comparison shows the improved constraints that the additional information provides. In the radial velocity data set, the tangential anisotropy of the Mestel sphere fit is unconstrained; in the augmented data set, the confidence contours close within $q = 1.0$ and $\eta = 5.0$, although there are still significant uncertainties in the estimates. These results rule out distributions with very strong anisotropy. The fit is nearly centered about isotropic. We will use the augmented data set throughout the remainder of this paper.

Parameter estimates for the Eddington sphere are consistent with the previous inference that the distribution is roughly isotropic with an anisotropy radius $R_a = 20\,\mathrm{kpc}$ (Table 4.6). Comparing the models with a likelihood ratio test shows that the Mestel sphere can be rejected in favor of the Eddington sphere with only 75% confidence. The Eddington sphere fits the observed spatial distribution slightly better because it has a core.

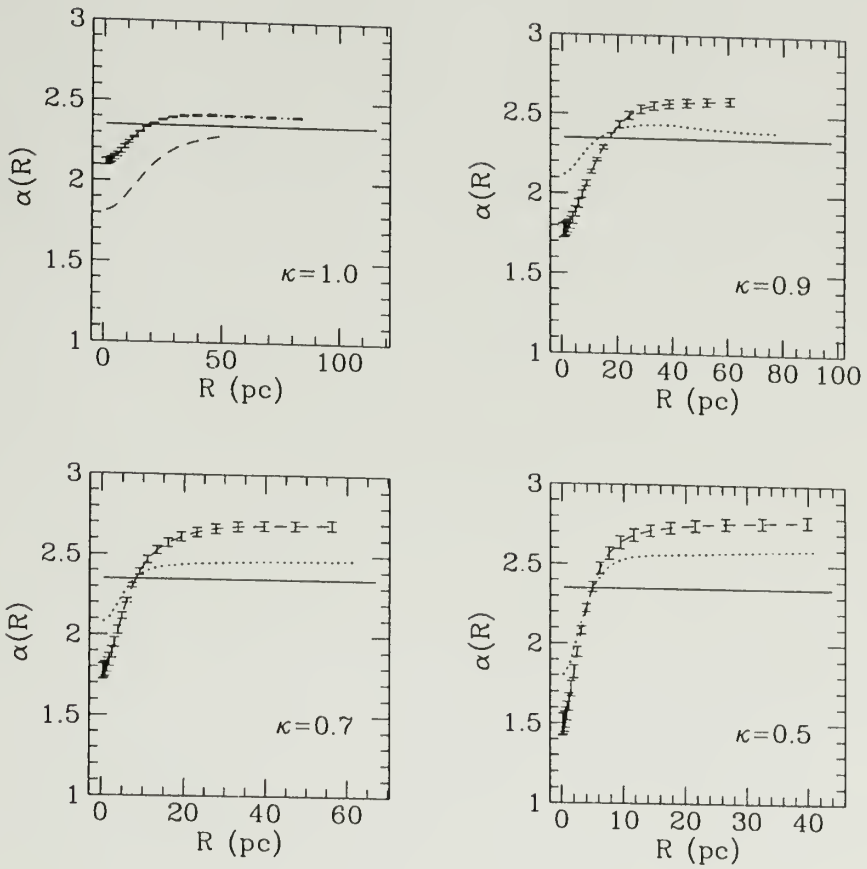

Figure 4.4. Orbital dependence of mass spectrum evolution. The line-of-sight mass spectral index as a function of projected cluster radius. Solid lines show the initial value, $\alpha = 2.35$; dotted lines show the dependence after 5 Gyr; dashed lines show the dependence after 10 Gyr, except for $\kappa = 1.0$ which shows $\alpha(R)$ after 7.5 Gyr, just prior to disruption. $1-\sigma$ error bars are plotted in only one case to show the typical size. The index $\alpha(R)$ shows the effect of mass segregation in each case, becoming flatter in the core and steeper in the halo. The increased difference between core and halo indices with eccentricity results from the more rapid evolutionary timescale at high eccentricity for orbits with equal apocenter.

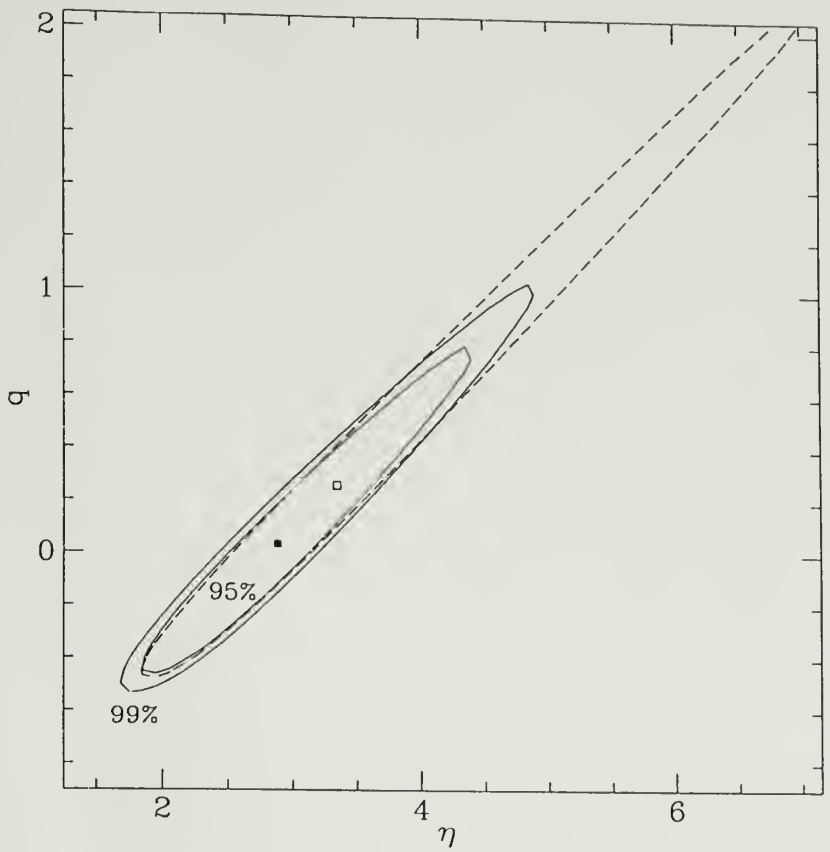

Figure 4.5. Comparison of data sets. Comparison of Mestel sphere fits to data with (solid) and without (dashed) available three-space velocities. The additional information in the augmented data set provides some constraint on the degree of tangential anisotropy compared to the pure radial velocity data. The uncertainty still dominates, but we can rule distributions which are very extremely anisotropic.

Table 4.6. Comparison of fits to Mestel and Eddington spheres.

Model	η	σ_η	q	σ_q	r_a	σ_{r_a}	log L
Mestel	2.89	0.25	0.04	0.11	-	-	-3544.4
Eddington	2.54	0.10	-	-	20.1	4.1	-3542.3

As the results of Paper II show, we expect the initial cluster distribution to follow a power-law profile and develop a core through evolution. Both models provide pure power-law space densities. However, the Mestel sphere can have arbitrary orbital anisotropy while the Eddington sphere must have purely radial orbits to produce a coreless model. Because we expect a nearly coreless initial distribution of clusters, the initial orbit distribution required by the Eddington model is kinematically unrealistic given the presence of so many moderate to high angular momentum orbits in the observed population. Therefore, in what follows below, we use only the Mestel sphere to model the spherical portion of the cluster distribution.

The mass spectrum of observed clusters is not well-described by a single power-law over the mass range considered here. Using a single power-law, Harris & Pudritz (1994) find a change in slope near 10^5 $M_\odot$. This trend is evident in Table 4.7 which compares fits to the mass spectrum using three different models: a single power-law, a two-component power-law and a Gaussian magnitude distribution. The single power-law shows a relatively flat spectrum in agreement with Harris & Pudritz (1994). The 2-component power-law shows a fairly steep dependence for $M > 2.2 \times 10^5$ $M_\odot$ and a nearly flat spectrum for masses below that. The Gaussian magnitude distribution peaks at 2.7×10^5 $M_\odot$ in agreement with the 2-component power-law.

Using a likelihood ratio test to compare the models, we find that the single power-law can be rejected in favor of both the Gaussian magnitude distribution and 2-component model at better than 99% confidence. However, the Gaussian

Table 4.7. Models of present-day mass spectrum

Model	α_1	σ_{α_1}	α_2	σ_{α_2}	$m_{cut}(M_\odot)$	$\sigma_{m_{cut}}$	log L
power-law	0.80	0.05	-	-	-	-	-260.56
2-component power-law	0.034	0.15	1.62	0.15	2.2×10^5	2.6×10^4	-248.38

Model	V_0	σ_{V_0}	σ_V	σ_{σ_V}	log L
gaussian mag.	-7.56	0.11	1.30	0.10	-251.03

can favored over the 2-component power-law with about 40% confidence. Regardless, we are faced with insufficient data to use models with many parameters, so we will use the single power-law as the simplest model which provides an acceptable description of the overall cluster mass distribution.

We characterize the dynamics of the observed cluster population using a 2-component disk-spheroid model (Table 4.8). The value of F, which gives the fraction of the cluster population in the spherical distribution, provides an estimate that 96% of the clusters in the sample are dynamically associated with the halo. This implies that only 4-5 of the sample clusters are associated with the disk, a result which contradicts our a priori knowledge that there are approximately 25 disk clusters in our sample (Armandroff 1993). Examination of the physical behavior in the previous section showed that clusters associated with the halo on low inclination orbits or which are confined to the disk will evolve more rapidly than those on high inclination orbits. We therefore expect the present-day distribution of halo clusters to be aspherical with lower density near the disk. The overestimate in the halo population size when using a spherical model is consistent with our dynamical expectation that cluster depletion is more effective for orbits confined to the disk. Nevertheless, a likelihood ratio test rejects the Mestel sphere at better than 99% confidence in favor of the 2-component fit. The improvement results from the strong tangential anisotropy which is attributed to the disk

Table 4.8. Present-day two-component model

	η	q	α	η_d	q_d	η_z	α_d	F	log L
estimate	2.75	-0.035	0.76	17.0	7.8	0.37	1.04	0.96	-3495.00
uncertainty	0.24	0.12	0.05	7.08	3.34	0.16	0.13	0.001	-

component using the two-component model, a feature which is consistent with the expectation that this component is rapidly rotating (e.g. Armandroff 1989).

4.3.3.2 Initial conditions

Evolution of the pure Mestel sphere, as expected, produces a profile which is shallower at present than in the past (Figure 4.6). The anisotropy changes little. The constraints are considerably better, however, and are consistent with an isotropic initial distribution.

Table 4.9 compares the best-fit parameters of the spherical model with the 2-component model. The spheroid in the 2-component model has a slightly shallower decline but is considerably more radially biased because the tangential velocities are mainly associated with the disk component. The uncertainties in the disk parameters are reduced because the present-day population fraction (1-F) is larger than in the present-day model. Here the population is currently expected to posess about 16 clusters, still somewhat below the expected number. Again this results from our assumption that an initially spherical model remains spherical. A likelihood ratio test rejects the purely spherical model with about 97.5% confidence.

The analysis predicts that the velocity distributions of both halo and disk components become more tangentially biased with time due to the more rapid evaporation of clusters on eccentric orbits. The initial orbit distribution of the halo component has fairly strong radial bias, with approximately 41% of its kinetic energy in radial motion, while the disk component has a nearly isotropic initial orbit distribution. In addition, the initial halo cluster density distribution has

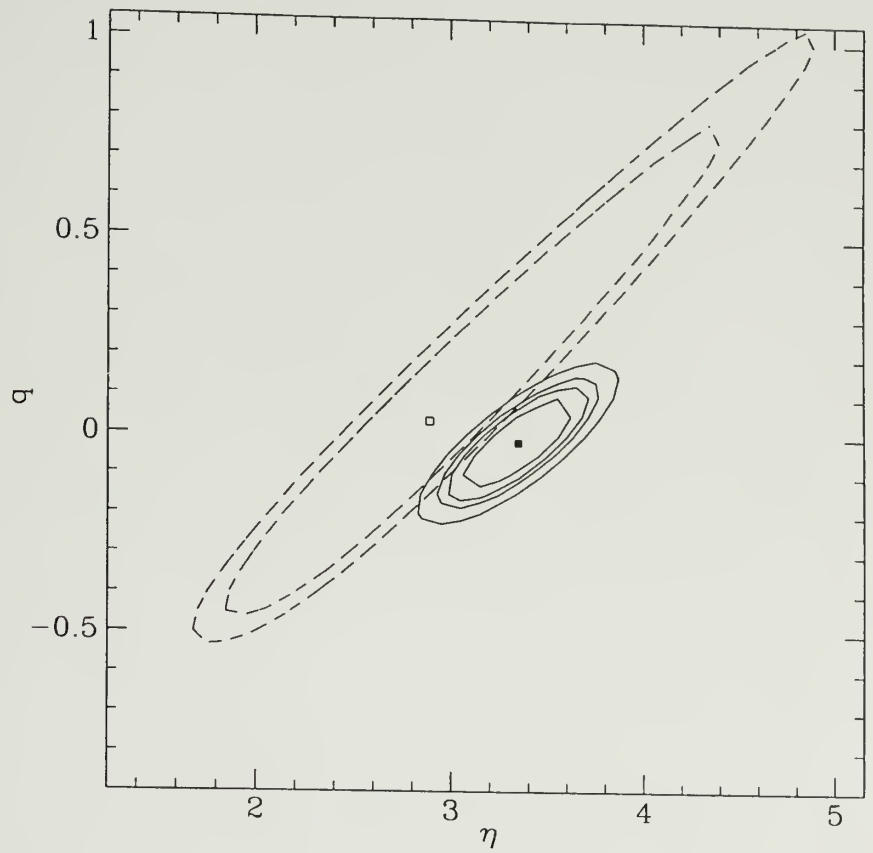

Figure 4.6. Comparison of parameter estimates in spherical models. Comparison of 50%,90%,95%,99% confidences in estimated initial parameters (solid) with confidences in estimated present-day parameters (dashed- superimposed from previous figure). Constraints are stronger on the initial distribution and indicate proximity to isotropy. The slope of the density distribution $-(\eta+2q)$ is steeper initially, going approximately as $r^{-3.35}$ while the present-day slope is best described as $r^{-2.95}$.

Table 4.9. Comparison of initial conditions in 2-component and spherical models

spherical

	η	q	α	η_d	q_d	α_d	F	log L
estimate	3.35	-0.018	0.95	-	-	-	-	-3486.94
uncertainty	0.32	0.16	0.06	-	-	-	-	-

2-component

	η	q	α	η_d	q_d	α_d	F	log L
estimate	2.82	-0.28	0.96	2.38	0.066	1.15	0.89	-3478.79
uncertainty	0.27	0.03	0.07	0.53	0.10	0.23	0.001	-

power law index of $\eta - 2q = 3.38$, while the disk cluster density distribution has power law index $\eta_d - 2q_d = 2.25$.

Figure 4.7 compares the cumulative distribution of clusters in our data sample with the evolved profile of the 2-component model along with the separate contributions of the disk and sphere. The model apparently matches the data fairly well. At small radii, our models overestimate the expected number of clusters. However, a KS test rejects the null hypothesis that the observed distribution is drawn from the model distribution at only 58% confidence. The overestimate can result from the exclusion from our data set of observed clusters at small radii which lack velocity information. Conversely, the models neglect dynamical friction, which should also be important at such small radii.

Using the initial conditions from the 2-component model, we derive the estimated initial distribution of clusters (Figure 4.8). The total initial population expected to give rise to our sample is about 250 clusters, with 200 in the spheroid and 50 in the disk. Approximately 43% of the initial population remains.

4.4 Discussion

Our estimates of the initial population size are tied to the assumption that an initially spherical distribution of clusters remains spherical. As the presentation of the physical behavior showed, we actually expect clusters confined on orbits near

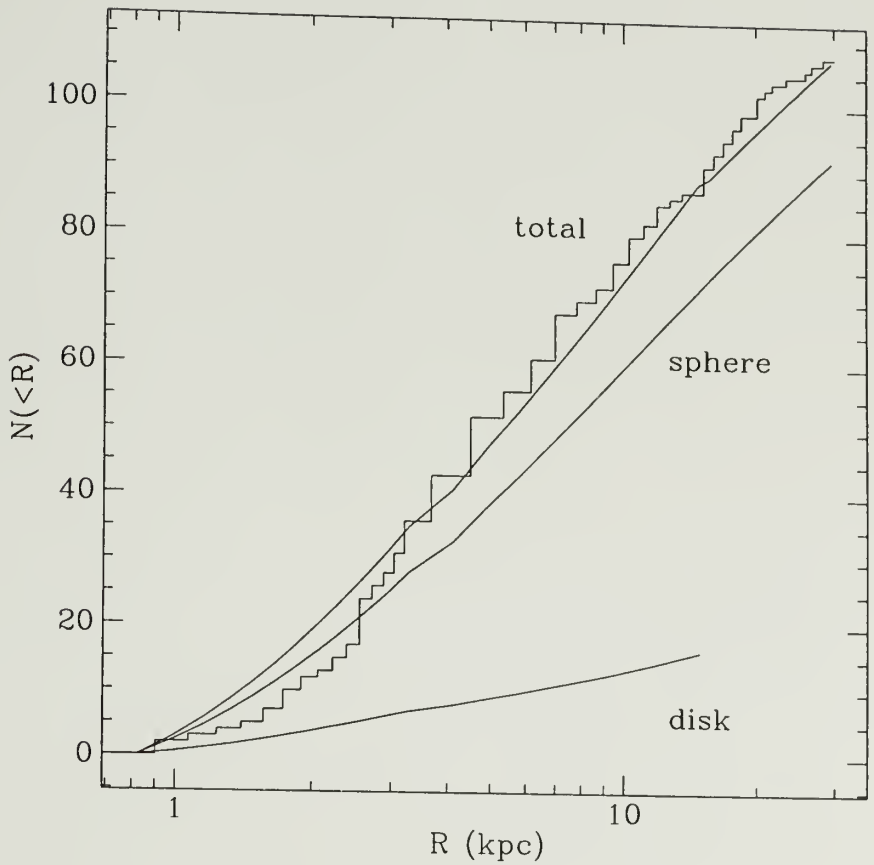

Figure 4.7. Comparison of observed and estimated evolved distributions. Comparison of the evolved 2-component model with the observed cumulative distribution of clusters with $R < 30\,\mathrm{kpc}$ in the present sample. The total number of clusters is 108. The spherical component is estimated to have 92 clusters and the disk 16.

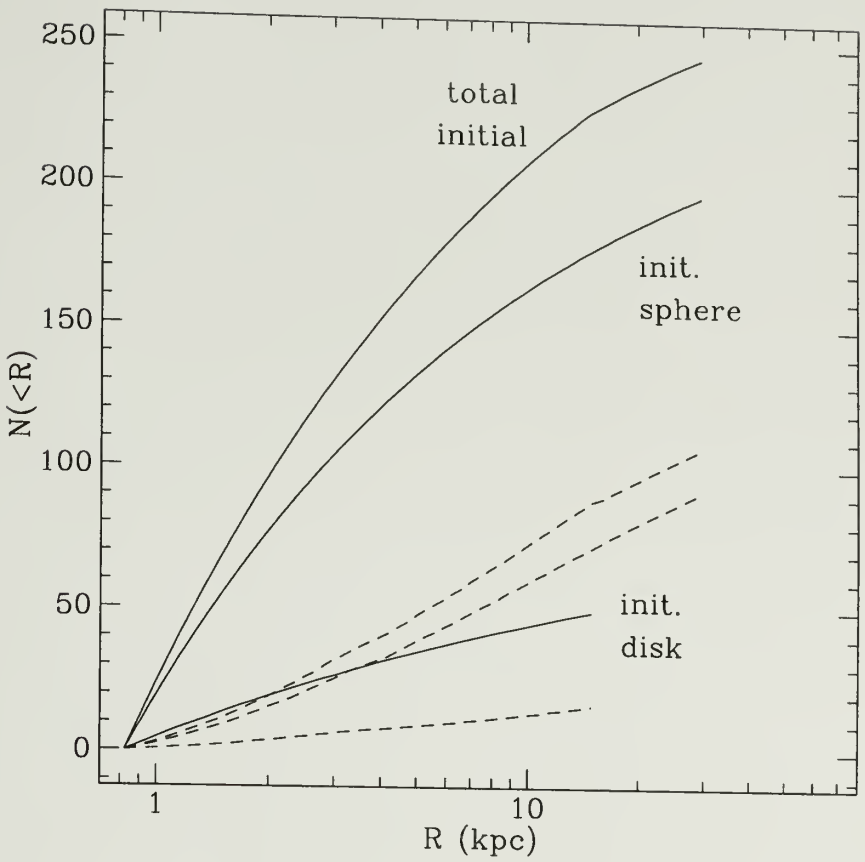

Figure 4.8. Comparison of initial (solid) and evolved (dashed- from previous figure) 2-component models. The total initial number of clusters is estimated to be about 250 with 200 in the spheroid and 50 in the disk.

the disk to decay more rapidly than clusters on high inclination orbits. This dynamical expectation was corroborated by the results of the two-component fit to the present-day population, which showed that, if we assume the halo population to be spherical, then we strongly underestimate the size of the disk cluster population.

Correctly accounting for the inclination dependence in halo cluster evolution will not significantly change the size of the inferred halo cluster population. The primary result will be to reduce the size of the present-day halo cluster population which this initial distribution produces by accounting for the loss of low inclination clusters. This will then increase our estimate of the size of the disk cluster population. The estimated number of current disk clusters in the evolutionary models is 16, which is roughly 60% below the expected number. Correcting the estimated initial population by this factor implies that there may have been upwards of 80 disk clusters initially.

The other important factor in estimating the initial population size is the choice of mass spectrum. Using a single power-law is necessitated by sample size, although we know that there is more likely a steep power-law dependence for $m \gtrsim m_{cut} \approx 2.2 \times 10^5\,\mathrm{M}_\odot$ and a shallower dependence for masses below that (m_{cut} also depends on the adopted mass-to-light ratio). From the two-component power-law mass spectrum fit and using the results of Paper II as a guide, we estimate that the spectral index may decrease by 0.2 for $m \gtrsim m_{cut}$ and by 0.3 for $m \lesssim m_{cut}$ since the higher range is very similar to that studied in Paper II while the lower mass clusters evolve more rapidly so heavier depletion occurs in this range. Therefore, the initial spectral indices may have been approximately $\alpha_1 = 0.3$ and $\alpha_2 = 1.8$. With this distribution, 49% of the clusters have $m \leq m_{cut}$. The vast majority of these clusters vanish in a Hubble time. For comparison, in the one-component power-law mass spectrum with $\alpha = 0.95$, only 47% of the

clusters have $m \leq m_{cut}$, so depletion for $m \leq m_{cut}$ should be roughly the same in the two-component power-law model. For $m \geq m_{cut}$, depletion should actually be higher in the two-component power-law model because of the greater proportion of clusters near m_{cut}, which is in the range of strong cluster evolution. We conclude, therefore, that adoption of a single power-law to describe the mean mass distribution should not strongly affect the size of the inferred initial population.

Let us now consider further implications of our results. Sommer-Larsen and Zhen (1990), investigating the spatial and kinematic distribution of halo field stars using a kinematically-unbiased, metallicity-selected sample $(-1.5 \leq [Fe/H] \leq -2.0)$, find that the density distribution behaves as $R^{-3.29\pm0.24}$ in the range $8\,\mathrm{kpc} \leq R \leq 20\,\mathrm{kpc}$ for which their sample is valid. This agrees well with the inferred initial density profile for the halo globular cluster distribution which we found to vary as $R^{-3.35\pm0.27}$. Furthermore, they find that the velocity ellipsoid is radially biased with $\sigma_R = 156 \pm 10\,\mathrm{km\,s^{-1}}$ and $\sigma_T = 156 \pm 10\,\mathrm{km\,s^{-1}}$, so that $50 \pm 6\%$ of the kinetic energy is in radial motion. This is roughly consistent with our estimate that $41 \pm 3\%$ of the kinetic energy of the initial cluster population is in radial motion. Consequently we suggest that the inferred characteristics may reflect a scenario in which halo clusters primarily formed or were accreted at early times along with a corresponding stellar component.

The disk clusters, conversely, show increased disparity with both thin and thick disk stellar populations. While the uncertainties in the estimate are significant, the initial orbit distribution appears nearly isotropic, strongly discrepant from the rapidly rotating stellar disk populations. We do, however, underestimate the size of the disk cluster population by using the spherical halo model, so some of the motion is unaccounted for. Nevertheless, given the radially biased orbit distribution determined for the halo clusters, it is not likely that a significant tangential component can be added to the disk distribution even when

using a fully consistent model of the halo cluster distribution. An isotropic initial distribution of disk clusters probably could not have formed in a very cold thin disk due to the large degree of random motion. However, these characteristics appear to correlate with the highly flattened component of the local halo observed by Sommer-Larsen & Zhen (1990). While observed disk clusters have lower metallicity than this halo component, it is conceivable that the much of the depleted, radially-biased component had lower metallicity, and therefore formed during an intermediate phase of the dissipative collapse which is thought to have given rise to the disk (e.g. Larson 1990).

4.5 Conclusions

The main conclusions of this work are as follows:

1. Disk heating through shocking on high-inclination orbits and through oscillations on low-inclination orbits strongly accelerates cluster evolution on low-eccentricity orbits compared to the spheroid alone. Disk oscillations prove more destablizing than disk shocking due to better frequency matching in typical cluster potentials.

2. Intermediate eccentricity orbits are favored for survival because evaporation dominates at high eccentricity and strong heating by the disk leads to intense tidal stripping at low eccentricity. Orbit distributions tend to become more tangentially biased because high-eccentricity evaporation dominates.

3. Evolution of disk clusters does not strongly depend on oscillation height but preferential loss of clusters on low-inclination orbits implies that the distribution of halo clusters is less dense near the disk.

4. The estimated initial distribution of halo clusters appears to match the present-day distribution of halo field stars both spatially and kinematically.

The initial distribution is radially anisotropic with approximately 40% of its energy in radial motion.

5. The estimated initial distribution of disk clusters does not appear to match the kinematic distribution of the stellar disk. However, it may correlate with the highly flattened halo component determined by Sommer-Larsen & Zhen (1990).

6. The profiles of evolving clusters deviate from King models in cases moderate to strong tidal heating. The profiles show density inflections which result from resonant clearing and which appear similar to the observed profiles of Grillmair et al (1995,1996).

7. The line-of-sight mass spectral index depends little on orbit expect for intrinsic differences in evolutionary time scales of tidally-limited clusters on different orbits.

Appendix A

Appendices for Chapter 2

A.1 Derivation of Tidal Potential

In the inertial Galactocentric frame, the coordinate components of a cluster star are

$$\vec{R} = \vec{r} + \vec{R}_{com}, \tag{A.1}$$

and its velocity components are

$$\vec{V} = \vec{v} + \vec{V}_{com}, \tag{A.2}$$

where $\vec{r}$ and $\vec{v}$ are the coordinates and velocities of the member star measured relative to the cluster center of mass and $\vec{R}_{com}$ and $\vec{V}_{com}$ are the center-of-mass position and velocity of the cluster. The Hamiltonian for an individual star in these coordinates is therefore

$$H_0' = \frac{1}{2}|\vec{V}|^2 + \Phi_c(|\vec{R} - \vec{R}_{com}|) + \Phi_R(|\vec{R}|) \tag{A.3}$$

We introduce coordinates centered on the cluster with axes fixed in space through a canonical transformation using a generating function of the second kind (Goldstein 1985). This function can be written

$$F_2(\vec{R}, \vec{v}, t) = (\vec{v} + \vec{V}_{com}) \cdot (\vec{R} - \vec{R}_{com}) + f(t) \tag{A.4}$$

where $f(t)$ is an arbitrary function of time. The transformation obeys the conditions $V_i = \partial F_2 / \partial R_i$ and $r_i = \partial F_2 / v_i$, thus satisfying Hamilton's principle.

The new Hamiltonian $H_0 = H_0' + \partial F_2/\partial t$ so that (assuming the summation convention throughout)

$$H_0 = \frac{1}{2}|\vec{v}|^2 + \Phi_c(|\vec{r}|) + \Phi_G(|\vec{r} + \vec{R}_{com}|) - \left.\frac{\partial \Phi_G}{\partial R_i}\right|_{R_{com}} r_i - \frac{1}{2}|\vec{V}_{com}|^2 + \frac{\partial f}{\partial t}. \quad \text{(A.5)}$$

Expanding the Galactic tidal potential about the center of mass, we obtain

$$H_0 = \frac{1}{2}|\vec{v}|^2 + \Phi_c(|\vec{r}|) + [\frac{1}{2}\left.\frac{\partial^2 \Phi_G}{\partial R_i R_j}\right|_{R_{com}} r_i r_j + ...] + [-\frac{1}{2}|\vec{V}_{com}|^2 + \Phi_G(|\vec{R}_{com}|)] + \frac{\partial f}{\partial t}. \quad \text{(A.6)}$$

The term in the second pair of brackets is an arbitrary function of time which arises as an ambiguity in canonical transformations (Goldstein 1985). We note that it equals $-L_{com}$, the negative Lagrangian of the center-of-mass motion and that it can be eliminated by an appropriate choice of f. In this case, setting $f = \int L dt$ (the action associated with the center-of-mass motion) gives the desired form of the Hamiltonian for a star in the cluster frame:

$$H_0 = \frac{1}{2}|\vec{v}|^2 + \Phi_c(|\vec{r}|) + [\frac{1}{2}\left.\frac{\partial^2 \Phi_G}{\partial R_i R_j}\right|_{R_{com}} r_i r_j + ...]. \quad \text{(A.7)}$$

In the expansion of the tidal potential, we can ignore all but the lowest-order term because successive terms are proportional to $(|\vec{r}|/|\vec{R}_{com}|)^{n-2}$ $(n = 3, ...)$ relative to the second order term and, therefore, fall off quickly due to the small size of a cluster compared to the size scale of the Galaxy. We are thus left with the quadratic approximation to the Galactic tidal field. The expression for the perturbing potential, equation (8), is obtained by evaluating this term of the expansion for the specific case of the logarithmic sphere.

A.2 Pericentric inner Lagrange points

To obtain an expression for the pericentric inner Lagrange point, it is convenient to first transform to rotating coordinates having one axis aligned with the galactocentric radius of the cluster on its orbit. We omit the details of the transformation here and simply give the expression for the effective potential at pericenter in the rotating frame:

$$\Phi_{eff} = \Phi_c(|\vec{r}|) + \frac{1}{2}\Omega_0^2(R_p)[|\vec{r}|^2 - 2x^2] - \frac{1}{2}|\vec{\Omega}_p \times \vec{r}|^2. \tag{A.8}$$

The first term is the cluster potential. The second term is the quadratic tidal potential for the logarithmic sphere transformed to a rotating coordinate system. The last term is the centrifugal potential arising from the angular frequency of rotation at pericenter. The quantity Ω_p is the pericentric angular frequency of the cluster orbit while $\Omega_0(R_p)$ is the angular frequency of a circular orbit at the pericentric radius which defines the tidal strain.

The pericentric inner Lagrange point x_p occurs at the instantaneous inflection point in the effective potential which lies along the galactocentric radius of the cluster. We derive an expression for x_p by considering the balance of forces which is implied by the effective potential. Taking the gradient, and considering the instantaneous point of equilibrium along the Galactocentric radius gives

$$\frac{GM(x_p)}{x_p^2} = \Omega_p^2 x_p + \Omega_0^2(R_p)x_p, \tag{A.9}$$

where the left-hand side gives the cluster force while the right-hand side gives the centrifugal force and tidal strain, respectively.

To derive an expression for the inner Lagrange point in terms of R_a/R_p, we first rewrite the angular frequencies Ω_p and $\Omega_0(R_p)$ in terms of the angular frequency of a circular orbit at apocenter $\Omega_0(R_a)$. Using conservation of angular momentum between apocenter and pericenter gives

$$\Omega_p = J/R_p^2 = \Omega_a\left(\frac{R_a}{R_p}\right)^2 = \eta\Omega_0(R_a)\left(\frac{R_a}{R_p}\right)^2, \tag{A.10}$$

where η denotes the ratio of the angular frequency of the orbit to the angular frequency of a circular orbit with the same apocenter. The flat rotation curve defines

$$\Omega_0(R_p) = \frac{V_0}{R_p} = \Omega_0(R_a)(\frac{R_a}{R_p}), \tag{A.11}$$

and substituting into equation (A.9) and solving for x_p, we obtain

$$x_p^3 = \frac{GM(x_p)}{2\Omega_0^2(R_a)}\left\{\frac{1}{2}\left(\frac{R_a}{R_p}\right)^2\left[\eta^2\left(\frac{R_a}{R_p}\right)^2 + 1\right]\right\}^{-1}. \tag{A.12}$$

Now we define the effective pericentric angular frequency

$$\Omega_p'^2 = \Omega_0^2(R_a)\left\{\frac{1}{2}\left(\frac{R_a}{R_p}\right)^2\left[\eta^2\left(\frac{R_a}{R_p}\right)^2 + 1\right]\right\} \tag{A.13}$$

where $\kappa = \eta e^{(1-\eta^2)/2}$ for the logarithmic sphere.

A.3 Derivation of flux equation

The flux equation, equation (2.9), can be derived from the $\langle f_2 \rangle$ formalism given in Weinberg (1994). The function $\langle f_2 \rangle$ defines the externally induced change in the distribution function. The general form for $\langle f_2 \rangle$ is

$$\langle f_2 \rangle = \sum_{\mathbf{l}} \mathbf{l} \cdot \frac{\partial}{\partial \mathbf{I}} \mathrm{W}_{\mathbf{l}}(\mathbf{I}), \tag{A.14}$$

where we have performed the phase-averaging to derive the perturbation as a function of the actions. The quantity $W_{\mathbf{l}}(\mathbf{I})$ is a scalar function of the actions

$$W_{\mathbf{l}}(\mathbf{I}) = \frac{1}{2}(\mathbf{l} \cdot \frac{\partial \mathrm{f}_0}{\partial \mathbf{I}})|\mathrm{U}_{\mathbf{l}}|^2|\mathrm{a}(\mathbf{l} \cdot \mathbf{\Omega})|^2, \tag{A.15}$$

where $a(\mathbf{l} \cdot \mathbf{\Omega})$ is a Fourier coefficient given by

$$a(\mathbf{l}\cdot\mathbf{\Omega}) = \int_{t_0}^{t} dt' e^{i\mathbf{l}\cdot\mathbf{\Omega}t'} g(t') \tag{A.16}$$

and other quantities are as defined in §2.2.

To derive the flux equation we note that $\langle f_2 \rangle$ can be written as a divergence:

$$\langle f_2 \rangle = \sum_{\mathbf{l}} \nabla \cdot \mathbf{W_l} \tag{A.17}$$

where $\mathbf{W_l} = W_\mathbf{l} \times \mathbf{l}$. This equation makes number conservation manifest in action space.

To implement this term in a 1-dimensional Fokker-Planck scheme, we must change variables from actions to $(E, \kappa, \cos\beta)$ and average over κ and $\cos\beta$ to obtain the one-dimensional flux in energy space. The transformation can be performed easily using the covariant form of the equation (e.g. Rosenbluth et al 1957).

The divergence written in covariant form is

$$V^{\mu}_{,\mu} = \frac{1}{\sqrt{g}} \frac{\partial}{\partial x^{\mu}} \sqrt{g} V^{\mu} \tag{A.18}$$

where V^{μ} is a contravariant vector and g is the determinant of the metric tensor, equal to the square of the Jacobian. Using this equation, we transform to the new $(E, \kappa, \cos\beta)$ coordinates, which we denote using primes. Transforming the contravariant vector $\mathbf{W_l}$ gives

$$\begin{aligned} \mathbf{W_l'} = W_\mathbf{l}(\mathbf{l}\cdot\mathbf{\Omega})\hat{\mathrm{E}} + W_\mathbf{l}\left(\frac{l_2}{J_{max}(E)} - \frac{l_1\kappa}{\Omega_1\Omega_{2max}}\right)\hat{\kappa} \\ + W_\mathbf{l}\frac{l_3}{\kappa J_{max}(E)}\widehat{\cos\beta}, \end{aligned} \tag{A.19}$$

where the quantity $W_\mathbf{l}$ is the function defined above but now written in terms of the new variables. $\mathbf{W_l'}$ is the function equivalent to $\mathbf{W_l}$ in the new coordinates.

Noting that the Jacobian is

$$\sqrt{g} = \kappa J_{max}^2(E)/\Omega_1. \tag{A.20}$$

we may write $\langle f_2 \rangle$ in the new coordinates:

$$\langle f_2 \rangle = \sum_1 \frac{\Omega_1}{\kappa J_{max}^2} \nabla \cdot' \left(\frac{\kappa J_{max}^2}{\Omega_1} \mathbf{W}_1' \right). \tag{A.21}$$

Averaging over $(\kappa, \cos\beta)$

$$\langle\langle f_2 \rangle\rangle = \frac{\int d\kappa d\cos\beta \kappa J_{max}^2/\Omega_1 \langle f_2 \rangle}{\int d\kappa d\cos\beta \kappa J_{max}^2/\Omega_1}, \tag{A.22}$$

gives the total change as a function of energy:

$$\langle\langle f_2 \rangle\rangle = \frac{\int d\kappa d\cos\beta \kappa J_{max}^2/\Omega_1 \partial(\sum W_1(\mathbf{l}\cdot\mathbf{\Omega}))/\partial \mathrm{E}}{\int \mathrm{d}\kappa \mathrm{d}\cos\beta \kappa \mathrm{J}_{\mathrm{max}}^2/\Omega_1}, \tag{A.23}$$

where the fluxes in the $\hat{\kappa}$ and $\widehat{\cos\beta}$ directions vanish due to the averaging. Fully expressed, the equation reads

$$\langle\langle f_2 \rangle\rangle = \left\{ \frac{1}{2} \sum_1 \frac{\partial}{\partial E} [\int d\kappa (\mathbf{l}\cdot \frac{\partial \mathrm{f}_0}{\partial \mathbf{I}})(\mathbf{l}\cdot\mathbf{\Omega}) |\mathrm{U}_1|^2 |\mathrm{a}(\mathbf{l}\cdot\mathbf{\Omega})|^2 \kappa \mathrm{J}_{\mathrm{max}}^2/\Omega_1] \right\} \times \left\{ \int d\kappa \kappa J_{max}^2/\Omega_1 \right\}^{-1}. \tag{A.24}$$

The phase space volume

$$16\pi^2 P(E) = (2\pi)^3 \int \frac{\kappa J_{max}^2}{\Omega_1} d\kappa, \tag{A.25}$$

which we substitute to find the total phase space flux

$$\langle\langle f_2 \rangle\rangle = (16\pi^2 P(E))^{-1} \frac{\partial}{\partial E} \{\langle\langle E \rangle\rangle\}. \tag{A.26}$$

In the asymptotic limit, this becomes the rate of change of the phase space density, equation (2.9).

A.4 Implementation

The rate of change in the distribution function due to external heating is given by equation (2.9). We write this in finite difference form for consistency with the Fokker-Planck scheme and solve after each diffusion step. The numerical implementation uses a flux-conserving finite-difference scheme with explicit time advance:

$$\frac{f_j^{n+1} - f_j^n}{\Delta t} = -\frac{1}{P_j}\left\{\frac{\mathcal{F}_{j+1/2} - \mathcal{F}_{j-1/2}}{\Delta E}\right\}, \tag{A.27}$$

where the flux $\mathcal{F}$ is denoted

$$\mathcal{F}_{j+1/2} = R_{j+1/2}\frac{df}{dE}, \tag{A.28}$$

and we have rewritten the previously defined heating rate as

$$\langle\langle \dot{E} \rangle\rangle = R(E)\frac{df}{dE}. \tag{A.29}$$

The function $R(E)$ represents the sum over all resonances which couple to orbits of energy E.

In equation (2.8), δ-functions denote resonant coupling of internal and external orbital frequencies. However, the resonant interaction has finite duration due to non-linear saturation or detuning which corresponds to a width in frequency space. For weak perturbations, narrow resonances develop since orbital frequencies evolve slowly. For strong perturbations large widths occur because frequencies evolve rapidly.

The grid spacing employed in the difference scheme defines the frequency widths. Wider spacing implies broader resonances. Broader resonances reduce the heating rate by smearing the input power over a wide region in phase space as shown in Figure A.1. To estimate the proper grid spacing, we use the bandwidth

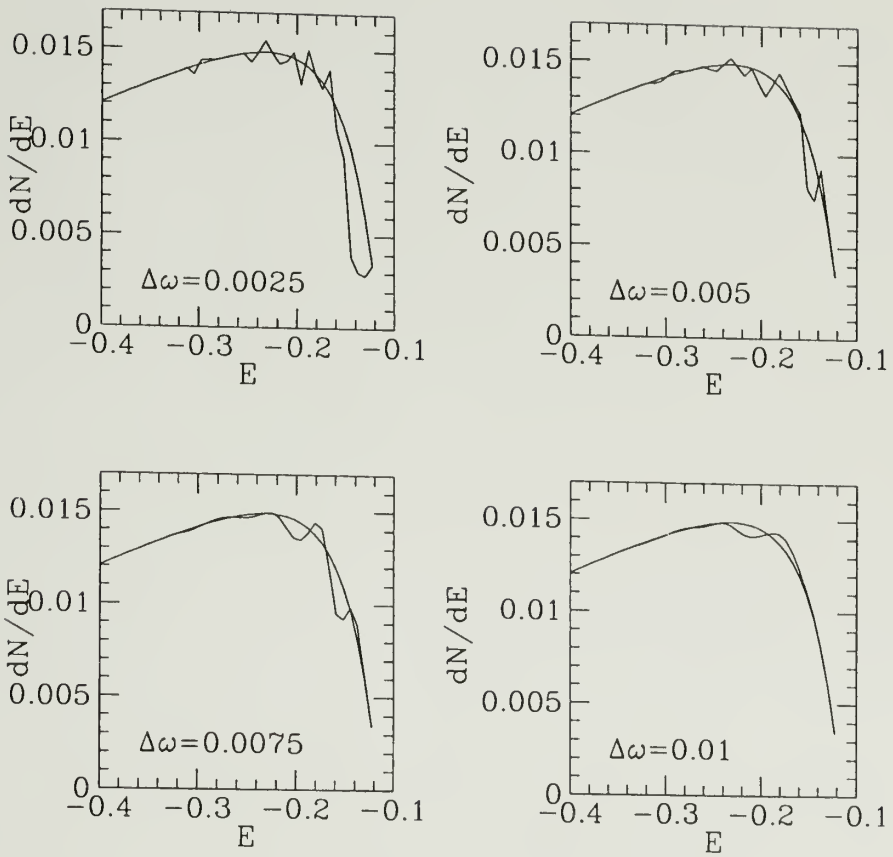

Figure A.1. Dependence of finite-difference method on grid spacing. Increasing grid spacing corresponds to broadening resonances for the resonant heating calculation. Broader resonances spread the input power over a range of energies. As a result, the DF evolves more slowly and does not develop strong resonant peaks and troughs. Here we evolve the DF in a fixed potential

theorem or uncertainty relation (e.g Bracewell 1986). The bandwidth theorem identifies the reciprocal relationship between the frequency width and sampling time of an oscillator:

$$\Delta\omega = \frac{2\pi}{\Delta t}. \tag{A.30}$$

Here the sampling time is the duration of resonance. Since non-linearity develops with some typical change in energy δE, we use the rate of energy input to estimate the duration of resonance:

$$\Delta t = \frac{\delta E}{\dot{E}}. \tag{A.31}$$

Comparisons with simulation indicate that 10% change in energy typically leads to frequency evolution. We calibrate the appropriate frequency widths using fully self-consistent N-body calculations described in Appendix A.5. For typical heating rates in tidally limited clusters, an initial spacing of $\Delta\omega = \Delta\mathbf{I} \cdot \mathbf{\Omega} \sim 0.005$ is appropriate. We use this value for all tidally-limited calculations. Larger tidal truncations require an increased width.

Two final implementation issues are the boundary conditions on the external heating equation and the Fokker-Planck equation. For the boundary conditions on equation (A.27), we set the flux to zero at the center and the gradient of the flux to zero at the edge. The latter condition represents evaporation. The last grid point of the DF therefore stays fixed between each diffusion step. We tested the choice in outer boundary condition using a zero flux condition and found solutions which differed by a few percent at most.

We use the standard tidal boundary condition in the Fokker-Planck equation. This calls for truncating the distribution function at the maximum energy allowed by the tidal limit. Because strict application of the boundary condition calls for truncating the cluster at x_p, we would throw out a potentially large fraction of the

initial cluster distribution in cases where $M(x_p) < 1$. As a less extreme alternative, we place the zero-DF boundary at the initial limiting energy of the cluster and set the heating rate according to our choice of x_p. Then we allow the boundary to evolve according to the mass loss. Tests with N-body calculations shown in Appendix A.5 indicate that the prescription works correctly.

A.5 Comparison with simulation

Comparisons of the external heating theory with N-body simulations are used to test linearity, the assumption of isotropy over long times, the importance of non-spherical moments in the potential, and the boundary condition on the heating equation (equation A.27) and to calibrate frequency widths of heating rates. We use a self-consistent field expansion code (e.g. Hernquist & Ostriker 1992) with 1.5×10^4 particles, radial expansion order $n = 10$ and angular order $l = 4$. Figures A.2 and A.3 show comparisons for $\kappa = 1.0$ and $\kappa = 0.3$ orbits. The two methods agree fairly well, especially at early times, before non-linearity and relaxation produce differences at later times.

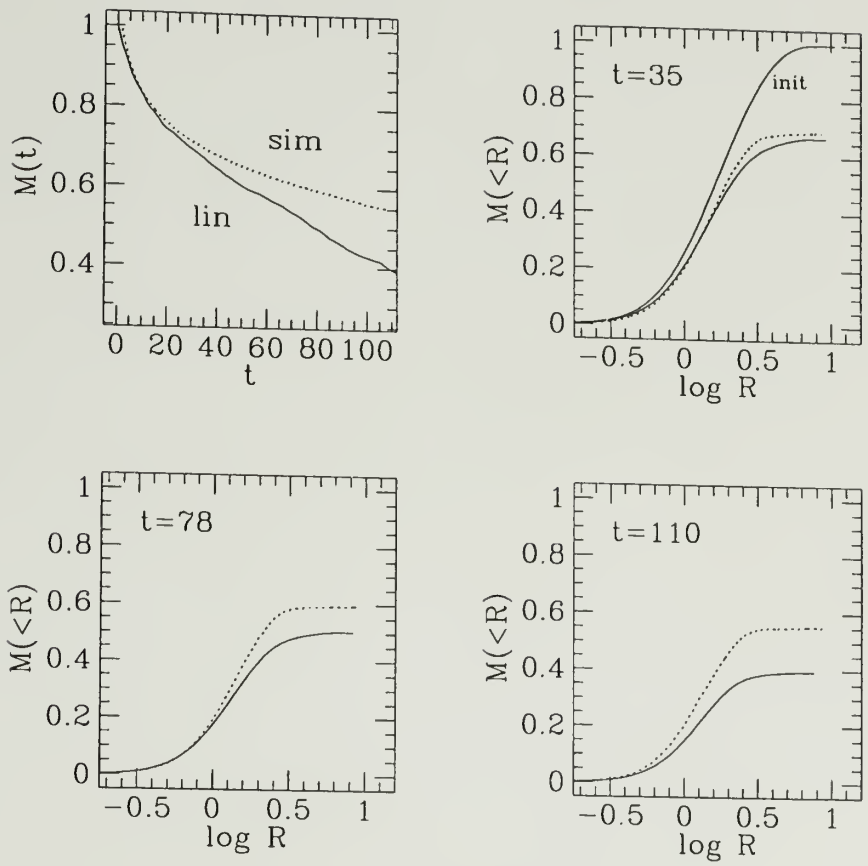

Figure A.2. Perturbation theory vs. N-body simulation for circular orbit. A $W_0 = 5$ cluster on a circular orbit with $M(x_p) = 0.95$. The half-mass dynamical time $t_{dyn} = 0.3$ and the orbital period is 2π. The top left panel shows the total mass as a function of time while the remaining panels show the mass profile at the indicated times. Agreement is good for $100t_{dyn}$. Deviation at later times results from inherent non-linearity and relaxation.

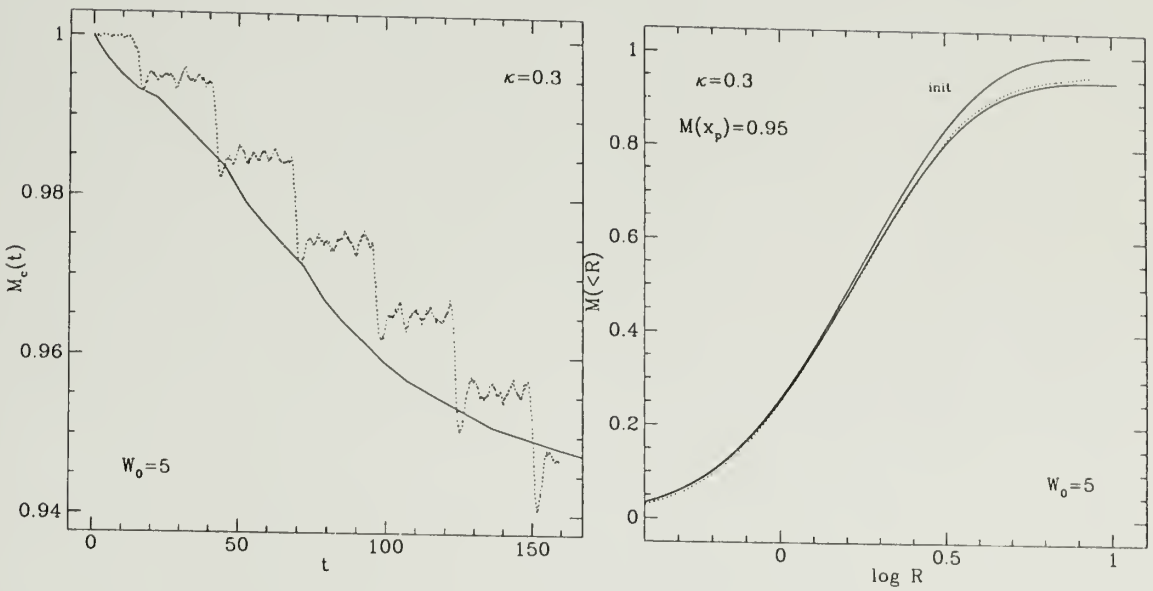

Figure A.3. Perturbation theory vs. N-body simulation for eccentric orbit. The same cluster as above on a $\kappa = 0.3$ orbit with $M(x_p) = 0.95$. The orbital period is $t = 30$. The left panel shows the evolution in total mass while the right panel compares the mass profiles at $t = 145$ or $483 t_{dyn}$. Agreement is good over this duration.

Appendix B

Appendices for Chapter 3

B.1 Cluster distribution functions

The initial cluster population is represented by joint distributions of the phase space density, $f(E)$ and the mass spectrum $\nu(M,r)$:

$$\psi(M,r,E,J) = \frac{\partial N}{\partial M \partial E \partial J} \propto f(E,r)\nu(M,r), \tag{B.1}$$

where $\psi(M,r,E,J)$ is the number of stars per unit mass per unit energy per unit angular momentum at a fixed point in space.

For the initial orbit distribution in coreless models, we generalize the isothermal distribution employed by OBS

$$f(E) = \frac{\rho_0}{(2\pi\sigma_0^2)^{3/2}} e^{-E/\sigma_0^2}, \tag{B.2}$$

with $\sigma_0^2 = \eta^{-1} v_0^2$. Note that $\eta^{-1} = \frac{1}{2}$ for the isothermal sphere and $\eta^{-1} = \frac{1}{3}$ for the fiducial model employed by OBS. The background gravitational potential of M87 is taken to be a singular isothermal sphere, $\Phi(r) = v_0^2 \ln r$, independent of the cluster distribution. The space number density of clusters for equation (B.2) is then

$$n(r) = \rho_0 r^{-\eta}. \tag{B.3}$$

We generalize this profile to include a core:

$$n(r) = \rho_0 (r_c^2 + r^2)^{-\eta/2} \tag{B.4}$$

where r_c is the core radius of the system. The isotropic cluster distribution function follows from integral inversion (e.g. Binney & Tremaine 1987).

We consider three initial distributions of cluster masses: 1) a Gaussian distribution of initial magnitudes, V, which is everywhere constant in space (e.g MHH); 2) a power law distribution of mass, M, which is everywhere constant in space (e.g. Harris & Pudritz 1994); and 3) a power law distribution of mass with a radially-dependent spectral index.

The Gaussian distribution of initial magnitudes V defines the mass spectrum

$$\nu(M) \propto e^{-\frac{1}{2}(\frac{V-V_0}{\sigma_V})^2} \frac{dV}{dM}, \tag{B.5}$$

where the transformation to mass is effected by the Jacobian, dV/dM. This distribution is characterized by two parameters: V_0 and σ_V, the mean and dispersion of magnitudes.

The simple power law mass distribution

$$\nu(M) \propto M^{-\alpha}, \tag{B.6}$$

depends only on the mass spectral index, α. We define the following radially dependent distribution

$$\nu(M, r) \propto M^{-(\alpha + Kr)} \tag{B.7}$$

whose spectral index has the central value α and varies linearly with radius.

B.2 Generalized isothermal sphere

We adopt a distance of 16 Mpc to M87 which corresponds to $H_0 = 81.5\,\mathrm{km\,s^{-1}\,Mpc^{-1}}$ (van der Marel 1994). This defines a length scale of 77.6 pc per second of arc. Lauer & Kormendy (1986) adopted $H_0 = 75\,\mathrm{km\,s^{-1}\,Mpc^{-1}}$, giving a distance of 17.4 Mpc and defining a length scale of 84.1 pc per second of arc. The more recent estimate by Elson & Santiago (1996) based on the Cepheid calibration of Freedman et al. (1994) gives a length scale of 87 pc per second of arc which is closer to the latter estimate but not strongly discrepant from the first.

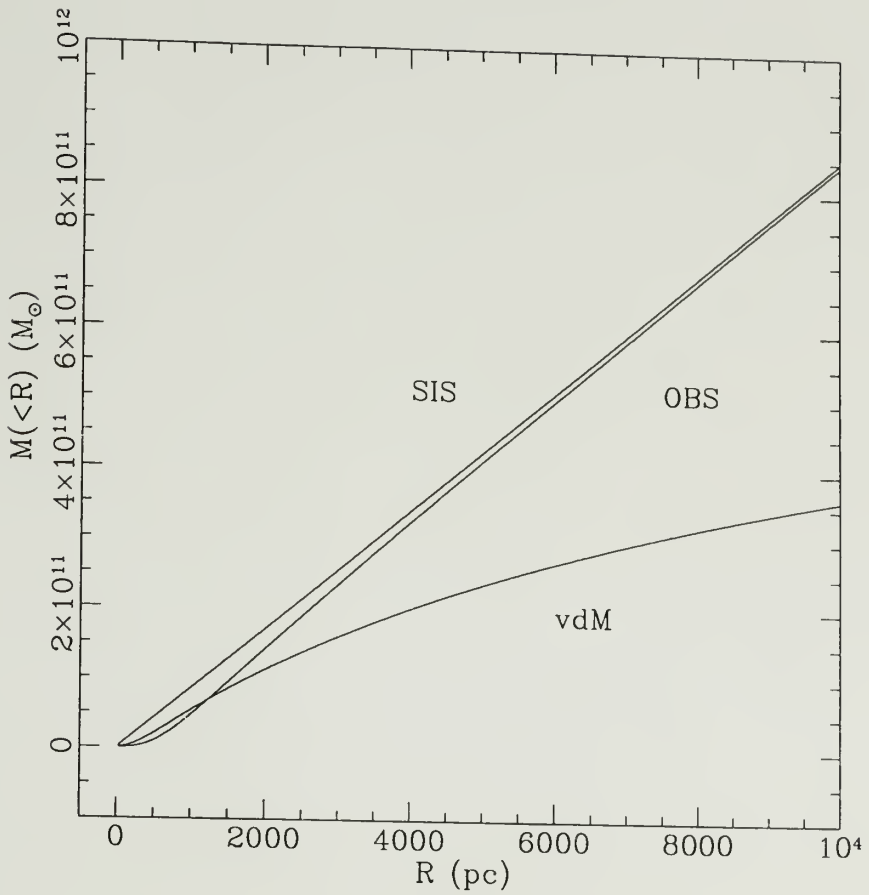

Figure B.1. Adopted mass distribution for M87. Comparison of singular isothermal sphere (SIS), softened isothermal sphere used by OBS, and the luminosity profile determined by van der Marel (1994). The isothermal models agree with the observed profile at small radii and continue to rise linearly with the dark matter halo.

OBS apparently adopted the length scale of 132 pc per second of arc, corresponding to $H_0 = 50\,\mathrm{km\,s^{-1}\,Mpc^{-1}}$.

For the singular isothermal sphere (SIS), $\Phi(r) = v_0^2 \ln r$, we adopt $v_0 = 606\,\mathrm{km\,s^{-1}}$ (OBS). This defines a velocity dispersion of $\sigma = 350\,\mathrm{km\,s^{-1}}$ for an initial distribution of luminous matter with $\eta^{-1} = \frac{1}{3}$. Figure B.1 compares the mass of the SIS with the softened isothermal sphere used by OBS, and van der Marel's (1994) estimate derived using the luminosity profile and dynamical modeling.

The results presented here do not significantly depend on choice of singular or softened potential. The 10% mass difference at 3 kpc leads to 5% faster evolution in the SIS since the dynamical time scale goes as $\rho^{-1/2}$ in tidally-limited clusters. This is well within the 4.7 kpc core radius of the cluster system determined by McLaughlin (1995). Conversely, the tidal field in the the slowly rising core region of the softened model is closer to that in a Keplerian potential which is stronger and so balances the larger mass of the SIS.

B.3 Maximum likelihood estimation of model parameters

A joint χ^2-maximum likelihood estimator is used in §3.4 to fit the dynamical models to V-band photometric data and binned surface density data of the M87 cluster system (MHH). THe expected surface density profiles are the sum of the dynamically evolved model surface density, $S(r, v; \theta)$, derived from distributions in §3.3, and background surface density, $\sigma_0(V)$, multiplied by the incompleteness factor, $f(x, y, V)$ which represents the probability of detecting a cluster of given magnitude at a particular location in the field. The likelihood statistic

$$L = \prod_j f(x_j, y_j, V_j)[S(r_j, V_j; \theta) + \sigma_0(V_j)], \tag{B.8}$$

defines the posterior probability of the data given the model. The χ^2 statistic

$$P_{\chi^2} = \prod_i \frac{1}{\sqrt{2\pi}\sigma_i} e^{-\frac{1}{2}\left(\frac{S_i - S(r,\theta)}{\sigma_i}\right)^2}. \tag{B.9}$$

defines the posterior probability of the binned data given the model. The total posterior probability is then

$$P = P_{\chi^2} \times L \tag{B.10}$$

and the parameters which maximize the posterior probability of the data are the best estimates.

Appendix C

Appendices for Chapter 4

C.1 Heating rate for disk oscillations

Clusters confined to the disk oscillate about the midplane thereby undergoing resonant tidal heating through the periodic tidal compression in the direction perpendicular to the disk plane. As discussed in Weinberg (1994), the tidal potential is given to good approximation by the leading (quadratic) term of an expansion of the disk potential about the center of mass of the cluster:

$$H_1 = 2\pi G\rho(Z(t))z^2, \tag{C.1}$$

where we have substituted the density for the second derivative of the disk potential using Poisson's equation. Z(t) denotes the cluster position as a function of time, while z refers to the position of a star relative to the center of the cluster.

Expanding the z^2 factor in the action-angle Fourier series as defined in Tremaine & Weinberg (1994), we obtain

$$z^2 = \sum_{\mathbf{l}=-\infty}^{\infty} [\frac{2}{3}\sqrt{\frac{4\pi}{5}}V_{2l_20}(\beta) + \frac{1}{3}\sqrt{4\pi}V_{0l_20}(\beta)]X_{l_2}^{l_1}e^{i\mathbf{l}\cdot\mathbf{w}}. \tag{C.2}$$

Substituting the resulting expression for H_1 into equation (8) of Paper I gives the heating rate

$$\langle\langle \dot{E}\rangle\rangle = -8\pi^4 P\frac{df}{dE}\sum_{\mathbf{l}=-\infty}^{\infty}\delta_{l_30}(\frac{1}{15}+\frac{1}{5}\delta l_20)(\mathbf{l}\cdot\mathbf{\Omega})^2|\mathrm{X}_{\mathrm{l}_2}^{\mathrm{l}_1}|^2$$
$$\sum_{n=-\infty}^{\infty}|a_n|^2\delta(\mathbf{l}\cdot\mathbf{\Omega}-\mathrm{n}\omega). \tag{C.3}$$

Choosing the vertical profile of the disk and the amplitude of vertical oscillations completely specifies the rate of energy input. In the present work, we adopt a

Gaussian vertical profile for the disk. Comparison with an exponential vertical profile reveals little difference in overall heating rate at any oscillation amplitude.

C.2 Coordinate systems

Our analysis uses three coordinate systems: heliocentric spherical coordinates, Galactocentric spherical coordinates and Galactocentric cylindrical coordinates. The first system is the natural observational reference frame while the second and third are the natural reference frames for the sphere and disk models, respectively. Primarily for reference in the following appendices, we define the symbols used to label various coordinates which are used.

In the heliocentric frame, we use (r, l, b) or distance, Galactic longitude and Galactic latitude. In the Galactocentric spherical frame, we use the (R, Φ, Θ) to denote Galactocentric distance, colatitude and azimuth respectively. In the Galactocentric cylindrical frame, we use the (R_d, Φ, Z) to denote Galactocentric radius in the disk, azimuth and height above the plane, respectively.

Velocity components in a particular direction are denoted with the corresponding subscript. In the heliocentric frame, (v_r, v_l, v_b) are the radial, azimuthal and latitudinal components, respectively. In the Galactocentric spherical frame, (v_R, v_Φ, v_Θ) are the radial, azimuthal and latitudinal components, respectively. In the Galactocentric cylindrical frame, (v_{R_d}, v_Φ, v_Z) are the polar radial, azimuthal and vertical velocities, respectively. We also write the components in the equivalent inner product form so that, for example, the Heliocentric velocity components are $(\vec{v} \cdot \hat{r}, \vec{v} \cdot \hat{l}, \vec{v} \cdot \hat{b})$.

C.3 Mestel Disk

The phase space distribution function for disk clusters in the thin disk approximation has the form

$$\frac{\partial N}{\partial E_d \partial J_z^2 \partial E_z} = f_d(E_d, J_z^2) g(E_z) \tag{C.4}$$

where $f_d(E_d, J_z^2)$ governs the distribution in the plane of the disk and $g(E_z)$ governs the distribution perpendicular to the disk. E_d denotes orbital energy in the disk; J_z refers to the angular momentum about the axis of the disk; and E_z denotes the energy of vertical osillations.

The Mestel disk distribution is defined as

$$f_d(E_d, J_z^2) = A e^{-E_d/\sigma_d^2} J_z^{2q_d}, \tag{C.5}$$

where σ_d^2 signifies the isothermal velocity dispersion in the disk. The radial and azimuthal velocity disperions are $\sigma_{R_d}^2 = \sigma_d^2$ and $\sigma_\Phi^2 = (2q_d + 1)\sigma_d^2$ which implies $q_d = \sigma_\Phi^2 / 2\sigma_{R_d}^2 - \frac{1}{2}$, so that $-\frac{1}{2} \leq q_D \leq \infty$.

The isothermal vertical distribution is defined as

$$g(E_z) = B e^{-E_z/\sigma_z^2} \tag{C.6}$$

where σ_z^2 signifies the isothermal vertical velocity dispersion. In reality, σ_z^2 varies as a function of radius in the disk because the scale height is constant while the central density varies. Assuming it to be fixed introduces some bias into the expected vertical velocities at a given radius but has no effect on cluster evolution because our calculations show that heating by disk oscillations is nearly independent of oscillation amplitude (or, equivalently, velocity at the midplane; c.f. §4.3.1).

Integrating over v_{R_d}, v_Φ, v_Z and Z yields the surface density in the logarithmic potential

$$\frac{dN}{d^2\vec{x}} = C\sqrt{\pi}(2\sigma_d)^{q+1}\Gamma(q + \frac{1}{2}) R_d^{-(\eta_d - 2q_d)} \tag{C.7}$$

where we absorb all vertical integration constants into the factor C and define the parameter $\eta_d = v_c^2/\sigma_d^2$. For $\eta_d - 2q_d = 2$, the density goes as $\ln R_d$.

C.4 Mestel Sphere

The phase space distribution function for halo clusters has the form

$$\frac{\partial N}{\partial E \partial J^2} = f(E, J^2). \tag{C.8}$$

where E is the total energy and J is the total angular momentum of a cluster.

The Mestel sphere has the same form as the Mestel disk,

$$f(E, J^2) = Ae^{-E/\sigma^2} J^{2q}, \tag{C.9}$$

but has a larger phase space volume so that $\sigma_R^2 = \sigma^2$ and $\sigma_T^2 = 2(q+1)\sigma^2$, where σ_T is the total transverse velocity dispersion. Consequently, $q = \sigma_T^2/2\sigma_R^2 - 1$ and $-1 \leq q \leq \infty$. Integrating over v_R, v_Φ and v_Θ gives the volume density in the logarithmic potential

$$\frac{dN}{d^3\vec{x}} = A\pi^{3/2}(2\sigma^2)^{q+3/2}\Gamma(q+1)R^{-(\eta-2q)} \tag{C.10}$$

where we define $\eta = v_c^2/\sigma^2$. For $\eta - 2q = 3$, the density goes as $\ln R$.

C.5 Eddington sphere

The Eddington model has the distribution function

$$f(E, J^2) = Ae^{-E/\sigma^2} e^{-J^2/2R_a^2\sigma^2}, \tag{C.11}$$

which implies that $\sigma_R^2 = \sigma^2$ and $\sigma_T^2 = 2\sigma^2/(1 + R^2/R_a^2)$. Integrating over velocities gives the volume density in the logarithmic potential

$$\frac{dN}{d^3\vec{x}} = A2\pi(2\pi\sigma^2)^{3/2}\frac{R^{-\eta}}{1 + R^2/R_a^2} \tag{C.12}$$

where we define $\eta = v_c^2/\sigma^2$.

C.6 Likelihood with incomplete data sets

An incomplete data set is defined as one in which some observations are missing. For the globular cluster system, some clusters might only have magnitudes and two-dimensional positions; others might have magnitudes and three-dimensional positions; still others might have velocity information, and so on. For each cluster, the observations have varying completeness with respect to the full set of observations required in a given model. There are several approaches to deriving parameter estimates in this situation. In the present work, we adopt a likelihood-based estimation scheme[1]

If we denote the full phase space vector for our models $(\vec{r}, \vec{v}, m)$ as Y and write $Y = (Y_{obs}, Y_{mis})$, where Y_{obs} signifies the observed data and Y_{mis} signifies the missing data, then $f(Y|\theta) = f(Y_{obs}, Y_{mis}|\theta)$ denotes the probability of the joint distribution of Y_{obs} and Y_{mis}, where $f(\cdot|\theta)$ is the underlying distribution governed by the parameters θ. Marginalizing the distribution over the missing data gives the marginal density of Y_{obs}:

$$f(Y_{obs}|\theta) = \int f(y_{obs}, Y_{mis}|\theta) dY_{mis}. \tag{C.13}$$

For independent observations, we denote the marginal probability for the i^{th} cluster as $f_i = f(Y_{i,obs}|\theta)$ and write the likelihood function in the usual way as the joint probability of the observations given the model:

$$L(\theta) = \prod_i f_i. \tag{C.14}$$

Using $L(\theta)$ to derive inferences concerning θ requires that there are no selection effects leading to the systematic absence of data for a particular class of observations. In practice, of course, we know that this is not the case for

[1]The following discussion is based on the presentation of Little & Rubin (1987), chapter 5.

observations of globular clusters, where, for example, latitude-dependent extinction results in the absence of radial velocities. However, in the present analysis we make no attempt to derive any type of selection function. One approach which does not ignore selection effects is the *Expectation-Maximization* algorithm, an iterative procedure which provides estimates for the model parameters as well as the missing data (Little & Rubin 1987, ch. 7).

The standard data set used in analyses of the spatial distribution and kinematics of the cluster system consists of cluster positions, masses and heliocentric radial velocities (e.g. Aguilar, Hut & Ostriker 1988; Thomas 1989). Therefore, as an example, if we take a spherical model for the cluster distribution function $f(E, J^2)$, the marginal probability of any given observation is

$$\bar{f}(v_r, R) = \int dv_l dv_b f(\frac{1}{2}(v_r^2 + v_l^2 + v_b^2) + \Psi(R), \\ R^2((\vec{v} \cdot \hat{\Phi})^2 + (\vec{v} \cdot \hat{\Theta})^2)), \tag{C.15}$$

where $\Psi(R)$ is the potential, and the tangential velocity components are written in inner product notation.

References

Aguilar, L., Hut, P. & Ostriker, J. P. 1988, ApJ, 335, 720

Ambartsumian, V. A. 1938, Ann Leningrad State U., no 22 [translated in Goodman & Hut 1985]

Armandroff, T., 1989, AJ, 97, 375

Armandroff, T., 1993, in The Globular-Cluster Galaxy Connection, eds. Smith, G. H. & Brodie, J. P., (Astr. Soc. Pacific: San Francisco)

Binney, J. J. & Tremaine, S. D. 1987, Galactic Dynamics, (Princeton: Princeton U. Press)

Blakeslee, J. P. & Tonry, J. L. 1995, ApJ, 442, 579

Bracewell, R. N. 1986, The Fourier Transform and its Applications, (New York: McGraw Hill)

Brodie, J. 1993, in The Globular Cluster-Galaxy Connection, ASP Conference Series, v. 48, ed G. Smith & J. Brodie, p. 483

Chaboyer, B., Demarque, P. & Sarajedini, A., 1996, ApJ, 459, 558

Chandrasekhar, S. 1942, Principles of Stellar Dynamics, (Chicago: Univ. Chicago Press)

Chernoff, D. F. & Djorgovski, S. G. 1989, ApJ, 339, 904

Chernoff, D. F., Kochanek, C. S. & Shapiro, S. L. 1986, ApJ, 309, 183

Chernoff, D. F. & Shapiro, S. L. 1987, ApJ, 322, 113

Chernoff, D. F. & Weinberg, M. D. 1990, ApJ, 351, 121

Cohn, H. N. 1979, ApJ, 234, 1036

Cohn, H. N. 1980, ApJ, 242, 765

Cohn, H. N. 1985, in Dynamics of Star Clusters, eds. Goodman, J., and Hut, P., (Boston: D. Reidel Publishing)

Cudworth, K. M., 1993, in Galaxy Evolution: The Milky Way Perspective, ed. Majewski, S. R., (Astr. Soc. Pacific: San Francisco)

Djorgovski, S. D. & Davis, M. 1987, ApJ, 313, 59

Djorgovski, S., Piotto, G. & Capaciolli, M. 1993, AJ, 105, 2148

Djorgovski, S., & Meylan, G. 1994, AJ, 108, 1292

Drukier, G. A., Fahlman, G.G. & Richer, H. B. 1992, ApJ, 386, 106

Eggen, O. J., Lynden-Bell, D. & Sandage, A. R. 1962, ApJ, 136, 748

Elson, R. A. W., Fall, S. M. & Freeman, K. C. 1987, ApJ, 323, 54

Elson, R., Hut, P. & Inagaki, S. 1987, ARAA, 125, 565

Elson, R. & Santiago, B. 1996, MNRAS, 278, 617

Faber, S. M. 1995, private communication

Faber, S. M. & Jackson, R. E. 1976, ApJ, 204, 668

Faber, S. M., Dressler, A., Davies, R. L., Burstein, D., Lynden-Bell, D., Terlevich, R., Wegner, G. 1987, in Nearly Normal Galaxies: From the Planck Time to the Present, ed. S. M. Faber, (New York: Springer-Verlag), p. 175

Fall, S. & Rees, M. 1985, ApJ, 298, 18

Freedman, W. L., Madore, B. F., Mould, J. R., Hill, R., Ferrarese, L., Kenicutt, R. C., Saha, A., Stetson, P. B., Graham, J. A., Ford, H., Hoessel, J. G., Huchra, J., Hughes, S. M., Illingworth, G. D. 1994, Nature, 371, 757

Gnedin, O. & Ostriker, J. P., 1996, ApJ, submitted

Goldstein, H. 1980, Classical Mechanics, (Reading, Mass: Addison-Wesley), p.383

Goodman, J. & Hut, P. ed. 1985, Dynamics of Star Clusters, IAU Symposium 113, (Dordrecht: Reidel)

Grillmair, C. J., Ajhar, E. A., Faber, S. M., Baum, W. A., Holtzman, J. A., Lauer, T. R., Lynds, C. R. & O'Neil, Jr., E. J., 1996, AJ, 111, 2293

Grillmair, C. J., Freeman, K. C., Irwin, M. & Quinn, P. J., 1995, AJ, 109, 2553

Harris, W. E. 1991, ARAA, 29, 543

Harris, W. E. 1996, private communication

Harris, W. E. & Pudritz, R. E. 1994, ApJ, 429, 177

Heggie, D. C., & Ramamani, N., 1995, MNRAS, 272, 317

Henon, M., 1961, Ann. d'Astrophys., 24, 369

Hernquist, L. & Ostriker, J. P. 1992, ApJ, 386, 375

Hesser, J. E., 1993, in The Globular-Cluster Galaxy Connection, eds. Smith, G. H. & Brodie, J. P., (Astr. Soc. Pacific: San Francisco)

Huchra, J. 1988, in The Harlow-Shapley Symposium on Globular Clusters in Galaxies, ed. J. Grindlay & A. Philip, (Boston: Kluwer), p. 255

Inagaki, S., in Dynamics of Star Clusters, eds. Goodman, J., and Hut, P., (Boston: D. Reidel Publishing)

Inagaki, S & Saslaw, W. 1985, ApJ, 292, 339

King, I. R., 1962, AJ, 67, 471

Kissler, M., Richtler, T., Held, E. V., Grebel, E. K., Wagner, S. J., Capaccioli, M. 1994, A&A, 287, 463

Kochaanek, C. S. 1996, ApJ, 457, 228

Krall, N. A., & Trivelpiece, A. W. 1973, Principles of Plasma Physics, (New York: McGraw-Hill)

Landau, L. D., & Lifschitz, E. M. 1965, Quantum mechanics, non-relativistic theory, (London: Pergamon Press)

Larson, R. B. 1990, PASP, 102, 709

Larson, R. B. 1996, preprint

Lauer, T. R. 1988, ApJ, 325, 49

Lauer, T. R. & Kormendy, J. 1986, ApJ, 303, L1

Lee, H. M. & Goodman, J. 1995, ApJ, 443, 109

Lee, H. M. & Ostriker, J. P. 1987, ApJ, 322, 123

Lee, H. M., Fahlman, G. G., & Richer, H. B. 1991, ApJ, 366, 455

Lee, M. & Geisler, D. 1993, in The Globular Cluster-Galaxy Connection, ASP Conference Series, v. 48, ed G. Smith & J. Brodie, p. 576

Lichtenberg, A., & Lieberman, M. 1983, Regular and Stochastic Motion, (New York: Springer-Verlag)

Lightman, A. & Shapiro, S. 1978, Revs. Mod. Phys., 50, 437

Little, R. J. A. & Rubin, D. R., 1987, Statistical Analysis with Missing Data, (New York: John Wiley & Sons, Inc.)

Lynden-Bell, D. & Kalnajs, A. 1972, MNRAS, 157, 1

Lynden-Bell, D. & Wood, R. 1968, MNRAS, 138, 495

Majewski, S. R., 1993, ARAA, 31, 575

Martin, B. 1971, Statistics for Physicists, (New York: Academic Press)

McLaughlin, D. E. 1995, AJ, 109, 2034

McLaughlin, D. E. & Harris, W. E. 1995, private communication

McLaughlin, D. E., Harris, W. E., & Hanes, D. A. 1994, ApJ, 422, 486 (MHH)

McLaughlin, D. E. & Pudritz, R. E. 1996, ApJ, 457, 578

Mihalas, D. & Binney, J., 1981, Galactic Astronomy: Structure and Kinematics, (Sanf Francisco: W. H. Freeman and Co.)

Mihos, J. C. & Hernquist, L. 1994, ApJ, 437, L47

Morrison, H. & Sarajedini, A. eds., 1996, Formation of Galactic Halo.... Inside and Out,(Astr. Soc. Pacific: San Francisco)

Murali, C. & Weinberg, M. D. 1996, MNRAS, submitted (Paper I; MW; Chapter 2)

Murali, C. & Weinberg, M. D. 1996, MNRAS, submitted (Paper II; Chapter 3)

Murali, C. & weinberg, M. D. 1996, MNRAS, in preparation (Chapter 4)

Murray, S. D. & Lin, D. N. C. 1992, ApJ, 400, 265

Oh, K. S. & Lin, D. N. C. 1992, ApJ, 386, 519

Okazaki, T. & Tosa, M. 1995, MNRAS, 274, 48

Ostriker, J. P.1985, in Dynamics of Star Clusters, eds. Goodman, J., and Hut, P., (Boston: D. Reidel Publishing)

Ostriker, J., Binney, J. & Saha, P. 1989, MNRAS, 241, 849 (OBS)

Ostriker, J. P., Spitzer, L., Jr. & Chevalier, R. 1972, ApJL, 176, L51

Ostriker, J. & Tremaine, S. 1975, ApJ, 202, L113

Pahre, M. A., Djorgovski, S. G. and de Carvalho, R. R. 1995, ApJ, 453, L17

Richer, H. B., & Fahlman, G. G. 1989, ApJ, 339, 178

Rosenbluth, M. N., MacDonald, W. M. & Judd, D. L. 1957, PhysRev, 107, 1

Sandage, A. R. 1953, AJ, 58, 61

Santiago, B. X & Djorgovski, S. G. 1993, MNRAS, 261, 753

Searle, L. & Zinn, R. 1978, ApJ, 225, 357

Sommer-Larsen, J. & Zhen, C., 1990, MNRAS, 242, 10

Spitzer, L. Jr. 1940, MNRAS, 100, 396

Spitzer, L., Jr. 1987, Dynamical Evolution of Globular Clusters, (Princeton: Princeton Univ. Press)

Spitzer, L., Jr. & Hart, M. 1971, ApJ, 164, 399

Spitzer, L., Jr. & Chevalier, R. A. 1973, ApJ, 183, 565

Stix, T. H. 1992, Waves in Plasmas, (New York: AIP Press)

Strom, S., Strom, K., Wells, D., Forte, J., Smith., M. & Harris, W. 1981, ApJ, 245

Stuart, A. & Ord, J. K., 1991, Kendall's Advanced Theory of Statistics, V.2, (London: Edward Arnold)

Szebehely, V. 1967, Theory of Orbits, (New York: Academic Press)

Thomas, P. 1989, MNRAS, 238, 1319

Titchmarsh, E. C. 1986, Introduction to the Theory of Fourier Integrals, (New York: Chelsea Publishing Company)

Tremaine, S. D. & Weinberg, M. W. 1984, MNRAS, 209, 729

van den Bergh, S. 1995, preprint

van der Marel, R., 1994 MNRAS, 270, 271

Wainscoat, R. J., Cohen, M., Volk, K., Walker, H. J. & Schwartsz, D. E., 1992, ApJS, 83, 111

Weinberg, M. D. 1994, AJ, 108, 1414

Zepf, S. E., & Ashman, K. M. 1993, MNRAS, 264, 611

Zepf, S. E., Geisler, D. & Ashman, K. M. 1994, ApJ, 435, L117

Zinn, R., 1985, ApJ, 293, 424

Zinn, R., 1993, in The Globular-Cluster Galaxy Connection, eds. Smith, G. H. & Brodie, J. P., (Astr. Soc. Pacific: San Francisco)

Zinn, R., 1996, in the Formation of Galactic Halo....Inside and Out, eds. Morrison, H. & Sarajedini, A.,(Astr. Soc. Pacific: San Francisco)